Light Fragment Formation in 11.5 GeV/c per Nucleon $Au + Au$ Collisions

A Dissertation Presented

by

Stephen Craig Johnson

to

The Graduate School

in Partial Fulfillment of the Requirements

for the Degree of

Doctor of Philosophy

in

Physics

State University of New York
at
Stony Brook

December 1997

State University of New York
at Stony Brook

The Graduate School

Stephen Craig Johnson

We, the dissertation committee for the above candidate for the Doctor of Philosophy degree, hereby recommend acceptance of the dissertation.

Dr. Thomas Hemmick
Advisor
Professor of Physics

Dr. Harold Metcalf
Professor of Physics

Dr. Barbara Jacak
Professor of Physics

Dr. Edward O'Brien
Physicist, Brookhaven National Laboratory

Dr. Heinz Sorge
Physicist, The University at Stony Brook

This dissertation is accepted by the Graduate School.

Graduate School

Abstract of the Dissertation

Light Fragment Formation in 11.5 GeV/c per Nucleon $Au + Au$ Collisions

by

Stephen Craig Johnson

Doctor of Philosophy

in

Physics

State University of New York at Stony Brook

1997

Inclusive double differential multiplicities of ^{2}H, ^{3}H, and ^{3}He at mid-rapidity and ^{2}H and ^{4}He at beam rapidity are presented for central Au + Au 11.4 GeV·A collisions at the AGS. Deuteron formation is studied for this system by both comparing these results with those at other bombarding energies and by utilizing simple models and the cascade code RQMD with a coalescence afterburner to describe deuteron yields. The strong dependence of the deuteron yield on the collective motion in the system is studied in light of a flowing thermal model and a novel technique is described and demonstrated for extracting heavy-ion source parameters from deuteron multiplicity distributions. Such a parameterization results in a deduced transverse radius and temperature of $R = 6.5^{+1.7}_{-.4}$fm and $T = 137^{+38}_{-12}$MeV.

Dedicated to the blessed Guardian whose model of

justice,

devotion,

wisdom,

and scholarship

shall be a standard for future generations.

It has for me.

Contents

List of Figures

List of Tables

Acknowledgements

> *Look, would it save you a lot of time if I just gave up and went mad now?* [Hitch Hiker's Guide to the Galaxy]

Unjust as it may be, one of the startling realizations at the culmination of pursuing a doctorate is the recognition of the multitude of supporting individuals who deserve this degree at least as much as you, friends, family and mentors who have paved the way for such a venture and, to my knowledge, have extracted no benefit.

For this reason, humanity has invented "The Acknowledgments" in a vain attempt to return to them the loving support they have so selflessly given. As I have found no method of dividing the benefits of this degree with them, [1] I too will revert to these brief pages as a public confession of their aid while awaiting the moment when I can return the favors.

I'm afraid this is going to be long...

---

[1] Will someone let me know what these benefits are so I may begin collecting them?

> *I just want to thank everyone who made this day necessary.* [Yogi Beara]

To proceed chronologically: The first thank-you's must be declared to my family. My father and mother, Mark and Sue, have been continual sources of support and to them I owe a great deal beyond my mere existence. Mark has been a standard of love and devotion to family, a man unafraid of deep personal changes and less afraid of what other people will think of them. I look to him as my source of integrity and devotion and, though I'm not the judge, fully deserves the title of 'Reverend'. My mother exudes a sense of calm and warmth meritorious even among mothers and, though she is probably unaware that this talent resides within her, has always been the one to whom I've turned in times of inner conflict because she has a sense of the right words to say to replace my turmoil with a sense of serenity.

In my life I've been blessed with other parents who have increasingly showered love and attention on me: to Don, my source of living-patience; to Craig, the touchstone of unconditional love; and to Sandy, the bubbly and vibrant mother of my siblings, care-taker of my father, and focal point of all of our loving insanity. To each of you I owe a sincere debt of gratitude for bolstering my beliefs and encouraging my learning. Thank-you.

I sincerely pity those poor people in the world who have only one (or five!) siblings; mine have upheld me through the years of my life thus far though they must often do so over great physical distances. To Mikaela, Monique, Sunny, Beth, Jesse, Amanda, Richard, and Tracy I owe a great debt of gratitude and probably more than a few hairs which were (inadvertently, of course) removed from their heads in our early years together. I continue to look forward to our co-development as we learn of all the points where we can rely on, support, and love one another.

To the Baha'is of Brookhaven: My fountain of faith and prayer. I would entrust my soul with each one of you and could not have sanely progressed without your presence. While to recount each one of the individual Bahá'ís would be the length of a thesis in and of itself [2], I would like to especially thank Joan and Gary Dunn, Sylvia Strong and Mina Khorshidi, who have served as worthy, working models of a sincerely Bahá'í life. Beyond them I appreciate the loving friend I have in (Auntie) Zoha who has fortified me on numerous occasions and John and Marie, who continue to astound my imagination due to their steadfastness, patience in trials and true love of scholarship, family and friends through it all. Their children, Rebecca and Jennifer stand as geniuses in my estimation, each in their distinct categories, as well as being extraordinary Skip-Bo players (of course I let them win!). Finally, to Tara, my very first true friend when I arrived from Colorado to Long Island, who continues to be a refreshing source of good company and loving companionship – God bless you all.

Concurrent with my physics experiences, in the past couple years I have had the bounty and privilege of joining the family of Bob and Marge Scheidet through my marriage to their blessed daughter Betsy. While they may often flatter me with their praise and encouragement, they should always be aware

---

[2] Hey, there's an idea!

that it is I that owe them the greatest debt, not only because of Betsy, but also because they have been true, loving parents to me and have captured my heart as only my family can. Their youngest daughter, Heidi, displays a maturity and strength far beyond her years and I am honored to embrace her as a true sister; our relationship, I pray, will continue to grow with the years.

In the development of a career, there are bound to be those individuals who have influenced life decisions, most often in positions of educational authority. I have had the bounty of three such individuals and, to them I owe my love of and future in science, a debt I feel can only be repaid by proving through my actions that I was worthy of their trust.

My first true interaction with physics occured in high school in the physics course taught by Mr. Guy Kirouac, the young, dynamic teacher who convinced me that not only was physics not distant from our reality, but was intimately related to so much that I found interesting. In his course I first began, under his encouraging comments, to think for myself and question naive and face-value arguments. I realize that those in his profession are not often appreciated for the profound affect they have on young students lives; he has certainly driven a large portion of my life and for that I am truly thankful.

This innate love of science was further encouraged under the guiding hand of Professor David Cook at Lawrence University who taught a large portion of all of the physics courses I took as an undergraduate. His discussions were always stimulating and his love of the subject was extremely contagious. He has encouraged the talents of a large number of young physicists and fed their personally unknown thirst for knowledge; his clarity of thought and development of a cogent argument shall be an example for me in the many years to come.

The third scientist and teacher, who has had the most profound impact on my scientific development is Professor Tom Hemmick; you can call him Tom. I was a teaching assistant working in Tom's class my first year at Stony Brook and was immediately impressed with not only his knowledge of physics but his obvious urge to convey this knowledge in the simplest, yet most profound, way. By my second year I had joined his research group and began to experience first-hand his sincerity, wit and scientific power and, as my love of this science began to grow, so did my attachment to this extraordinary man. He has been an insightful tutor, an encouraging mentor and, as the years have passed, is developing into a genuine colleague. I look forward to the years we will have together in this community and the further insights he will shower upon me and hope that I will, in some way, be able to return with as much sincerity all that he has given to me. He is truly my "ambassador of coin". Thank you Tom, for all that I have found impossible to write in an acknowledgments.

To those postdocs and my fellow students: Dariusz Miskowiecz, Marzia Rosati, Martin Trzaska, Johannes Wessels, Nu Xu, Thongbay Vongpaseuth, Mark Pollack, Wen-Chen Chang, Sergei Panitkin, Tim Piazza, Youngil Kwon, Mikhail Kopytine, Wade Smith, and Corrie Vaa – I owe them my sanity during these past four years of study and research. They have been selfless in sacrificing their time and effort so that I could begin my career in physics. They were always patient with my ignorance and encouraged my individual ideas. Thank you for being a shelter of my developing scientific career.

Special thanks to Socoro Delquaglio and Rich Hutter who have been instrumental in assuring that my physics studies have been kindly interrupted by friendship. Socoro's ability to make my life significantly smoother and Rich's engineering skills and heckling have added an extra dimension to my time at Stony Brook. I appreciate the companionship of them both.

Of course, one of the greatest debts of gratitude I owe is to my lovely wife, Betsy, who has not only supported me in my studies but is actively involved in developing my character. She has been and will continue to be my eye-of-the-storm, that point of calm in the middle of the chaos of my life. Day-by-day my attachment to her expands and my love for her increases. I am truly honored to be married to such a woman.

Chapter 1

An Introduction

> *[Science] will free man from his remaining chains, the chains of gravity which still tie him to this planet. It will open to him the gates of heaven.* [Wernher Von Braun]

1.1 The Fundamental Forces of Nature

Modern theoretical physics has developed the standard model, a description of nature which accounts for the fundamental forces of nature by proposing local gauge invariance ($U(1) \times SU_2(2) \times SU(3)$). The beauty of such a theory is that three of the four forces of nature can be described in a uniform manner, the only excluded force being gravity, and that this invariance necessarily implies massless mediators of the fields, called gauge bosons, which have been experimentally detected.

For example, Quantum Electro-Dynamics (QED), a description of the electro-magnetic force, may be formulated through a $U(1)$ local gauge symmetry with the photon as a gauge boson; the weak force may be described by a $SU_2(2)$ symmetry. Recently, QED and the weak force have been theoretically combined into the electro-weak force which has $U(1) \times SU_2(2)$ gauge invariance. To its credit QED is the most accurate theory ever formulated by science, predicting the magnetic moment of the electron correctly to 13 decimal places [1]. Ironically, Quantum Chromo-Dynamics (QCD) which describes the interaction of the strong force between quarks and gluons with an $SU(3)$ gauge invariance, is virtually incalculable except under the most extreme and least common circumstances: interactions at high momentum transfer (q^2) and low coupling constant (α_s). It is this region that most high energy experiments investigate today. In order to probe the physics of QCD at low q^2 scientists have had to utilize the mechanism of a phase transition, which needs a large collection of quarks and gluons as a medium. This has led physicists to propose heavy ion collisions as a probe for such physics processes.

1.2 QCD Phase Transitions

> *[I]gnorance more frequently begets confidence than does knowledge: it is those who know little, and not those who know much, who so positively assert that this or that problem will never be solved by science.* [Charles Darwin, *The Descent of Man* (1871).]

The primary goal of the physics of relativistic heavy ion collisions is the study of nuclear matter under extreme conditions of temperature and baryon density in order to probe QCD at low q^2. Probes of this region of physics will shed light on the process of the big bang and possible conditions inside of neutron stars. More specifically, this field of physics yearns to detect two predicted phases of nuclear matter: the restoration of chiral symmetry and the deconfinement of quarks or the quark-gluon plasma (QGP).

1.2.1 The Quark Gluon Plasma

The deconfinement phase transition or Quark Gluon Plasma (QGP) is a fundamental prediction of QCD as calculated on the lattice [2] and predicted from simple arguments about the standard model [3]. While the order of the QGP transition for non-zero baryon density is still debated, though expected to be second order, the theoretical prediction for its critical temperature has settled near $T_{QGP} = 150 MeV$ [2] for zero baryon density. This transition should also be attainable through large baryon densities, on the order of 5-10 times normal nuclear matter density.

Phenomenologically, the phase transition may be described as follows. The strong force, the interaction occuring between quarks via massless gluons, has a running coupling constant such that the effective force between two quarks is large at distances beyond a Fermi and relatively small below this value. Because of this, a free quark will never be seen isolated from its color-neutral bag since the energy one must put into a system in order to separate two quarks is sufficient to create a new $q\bar{q}$ pair which bind to the separated quarks and create two color neutral mesons. The creative solution to viewing a free quark is to instead drive a large number of quarks together where the coupling constant is very small; this configuration is shown qualitatively in Fig. 1.1. As we push hadrons close enough together such that their effective radii overlap, the quarks will no longer feel confined since those quarks at

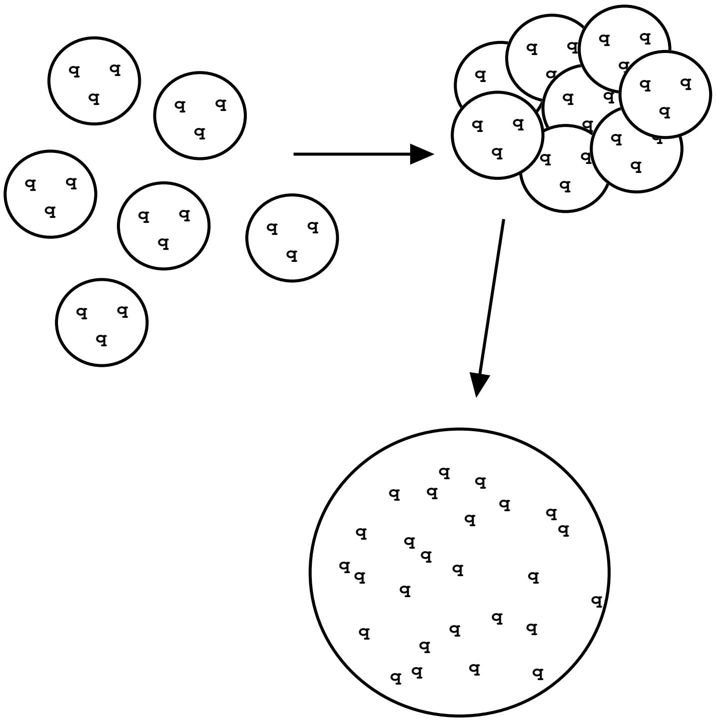

Figure 1.1: A qualitative picture of a transition from normal nuclear matter compressed to overlap the hadronic bags and finally to create a quark gluon plasma. The gluons are not shown in this figure.

large distances will be Debye screened by those nearby. Therefore, color deconfinement can be considered the approximate QCD analog of the insulator - conductor transition in QED. When these quarks are screened, they will feel free to roam about the entire deconfined region which could be 10-100 times larger than an individual hadron.

Shown in Fig. 1.2 is a standard theoretical phase diagram of nuclear matter showing phase transitions to a hadronic gas and a QGP including qualitative paths for the early universe, a neutron star, and a heavy ion collision. It

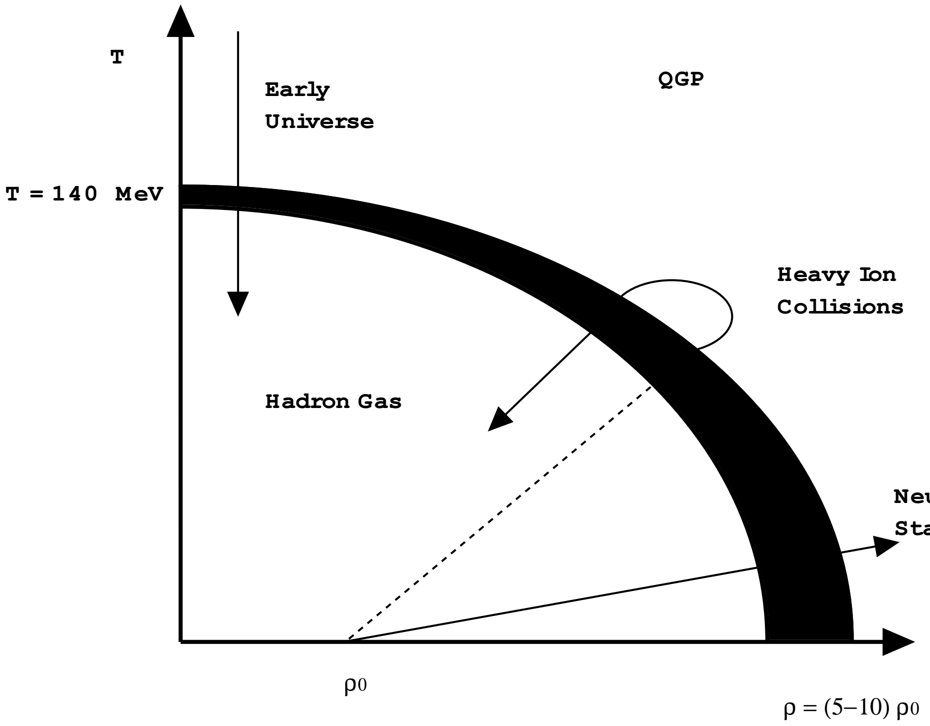

Figure 1.2: A phase diagram of nuclear matter showing qualitative paths for the early universe, a neutron star and a heavy ion collision. ρ_0 is the density of normal nuclear matter.

is the ultimate purpose of relativistic heavy ion collisions to create this QGP and, more importantly, to study its properties.

In this asymptotic region, the nature of hadronic matter is expected to change dramatically; the tricky part for experimentalists is that the QGP must hadronize again. That is, the quarks must form into hadrons again far before they can reach the experimental detectors and so some of the signals of this phase transition may be lost in the hadronization process. For this reason, it is expected that measuring simply hadronic signals is not sufficient for studying the QGP as they include an integrated history of the heavy-ion collision, from the initial ions traveling towards one another to the final strong interaction. The other option is to study leptons from the collision zone which do not interact strongly with the nuclear matter but are instead created throughout the entire collision and travel directly to the detector without further interactions; one draw back to this signal is that it is relatively weak and often dominated by hadronic processes which also create leptons. This situation results in the fact that there are few unambiguous signals for measuring the QGP; a thorough study of many signals is currently the best bet for studying the possibility of this phase transition.

1.2.2 The Chiral Phase Transition

> *Whether man is disposed to yield to nature or to oppose her, he cannot do so without a correct understanding of her language.* [Jean Rostand]

The second, though less publicized, transition is that of chiral symmetry restoration. Chiral symmetry is a perfect symmetry in the limit of massless quarks. Since the up and down quarks are nearly massless compared with hadronic scales, QCD has a nearly exact $SU(2) \times SU(2)$ symmetry such that the pions act as a Goldstone boson, or a collective mode, in the vacuum condensate. This approximation allows the calculation of low-energy theorems and sum rules for QCD [5] which approximately hold.

The vacuum condensate associated with the $SU(2) \times SU(2) = O(4)$ chiral symmetry is a four-vector $(\sigma, \vec{\pi})$. In a chirally symmetric universe, this vector would have no preferred direction. However, in our universe, this four-vector points in the sigma direction. At high energy densities in hadronic collisions theorists suspect that a region of matter may be created that is oriented differently than "normal" nuclear matter. If this should occur, in order for this chirally disoriented region to freeze out, it must decay to the true vacuum orientation by emitting a disproportionate number of pions of one particular specie (e.g. π^0). This signal of a phase transition from the *disoriented chiral condensate* (DCC), which by current models is suspected to occur at $T_c \approx 260 MeV$ [4], should be discernible by studying the event-by-event fraction of produced pions.

J. D. Bjorken, one of the primary proponents of a study of the DCC, notes that "...while everyone (theorists) talks about the QCD vacuum, hardly anyone (experimentalists) tries to do something about it" [6]. While some experiments have chosen to study this phase of matter, most notably the theoretician-driven Tevatron experiment T864 (MiniMax) [7] and the CERN experiment WA98 [8], this topic remains mostly of theoretical interest as the majority of experimentalists focus their studies on the quark-gluon plasma. However, it should be noted that the study of light pseudoscalar mesons and their masses in dense nuclear matter, which has had a surge of recent interest [11, 14], is also linked to the Goldstone boson nature of QCD and therefore indicates a potential signal for chiral restoration.

1.3 The Theory of Heavy Ion Collisions

> *The truth is a young maiden as modest as she is beautiful, and therefore she is always seen cloaked. [The Island of the Day Before by Umberto Eco]*

Collisions of heavy nuclei at relativistic energies are expected to probe the history of the universe by reproducing it on a much smaller scale and in reverse. The universe is hypothesized to have started as a point distribution in the big bang model which, subsequently, passed through a number of phases. In particular, this theory must include a time when the universe passed through a deconfined stage. Resulting from the consequent cooling and expansion of this system, the universe then passed through a hadronization phase when the quarks combined into hadrons, first a hot gas with numerous pions and resonances and then into a cool hadron gas. Finally the region of combination of protons and pions into light nuclei, or coalescence, will have occurred, resulting in nuclei up to and including lithium. Through the gradual evolution of this system, and gravitational influence, the universe soon produces stars which act as factories for heavier nuclei.

Some studies have attempted to learn about the history of the universe and the deconfined state by studying current day abundances of light nuclei coupled with a hypothesis of nucleosynthesis [9]. To date no "smoking gun" for a hot big bang has been deduced from isotopical considerations due to the uncertainties both in the theoretical calculations and the experimental measurements of isotope abundances. The deconfined stage seems to be sufficiently cloaked by the period of hadronization that such a determination is difficult, if not impossible. However, these measurements may still quantify the cooling stage of the universe, determining temperatures and appropriate time parameters.

In order to reproduce the conditions present immediately following the big bang, heavy ion collisions first reproduce the process in reverse, where heavy nuclei are collided together to create a hot, dense region where particles are produced and the resulting energy-density leads to a dissolution into a QGP. However, similar to the universe, our "little bang" must expand and cool to eventually reach a hadron gas which results in numerous emitted hadrons, predominantly pions, kaons, nucleons and, through coalescence, light nuclei.

To achieve the experimental conditions needed to create the QGP or restore chiral symmetry, nuclear collisions are conducted at beam energies above 1 GeV·A utilizing heavy nuclei. The purpose for such beams and targets is that heavy ion collisions have a large energy and particle deposition in a small region of space and, from simple cascade models, include enough reinteractions between constituents, typically between 10 and 20, that the system can properly thermalize.

While the recipe for creating a deconfined state may be relatively easy with current day beam technology, simply push enough hadrons together into a small volume with a large energy density, the detection and subsequent study of such a phase has to date eluded experimental signals. The difficulty is the same as that discovered by those studying the big-bang isotopic contributions: the deconfined stage is hidden from absolute detection by hadronization.

1.3.1 Probes and Measures of Heavy Ion Collisions

Emitted from a heavy ion collisions are a large variety of particles, including pions and nucleons in abundance as well as kaons and light nuclei less predominantly. Furthermore, leptons are also produced in heavy ion collisions such as electrons and muons and, though less widely created, are the primary focus of some experimental groups. In the following I will give a brief introduction to the methods utilized for collecting and interpreting the emission function from a heavy-ion collision. However, light nuclei production, the focus of this thesis, will be covered separately in Section 1.4. For a review of each of these methods, the reader is referred to [11].

Hadronic Observables

Hadronic particles, predominantly p, π and K, are traditionally interpreted according to their event averaged transverse and longitidunal distributions. This technique has been used because (1) there are statistically not enough hadronic particles of one particular specie exiting the collisions such that it can be described via an event-by-event model [1] and (2) hadronic observables from the collisions are thought to have suffered enough collisions for them to be interpreted thermally.

---

[1] With the advent of collisions at RHIC with $\sqrt{s} = 200 GeV \cdot A$ the number of pions will be sufficient to produce an event-by-event analysis of particle spectra, predominantly with the STAR experiment. For a review of the experiments at RHIC see [10].

If hadronic observables are truly thermal, one would expect that the transverse distributions would be describable by a temperature. For a Boltzmann assumption, the transverse spectra should be described by

$$\frac{d^2N}{dp_t dy}|_{mid-y} \propto \exp(-E/T) = \exp(-m_t \cosh(y)/T) \tag{1.1}$$

where m is the mass of the particle, $m_t = \sqrt{m^2 + p_t^2}$, p_t is the transverse momentum, y is the rapidity and T is the temperature of the system.

An intruiging dependence of the Boltzmann temperature as a function of particle mass has been noted. For a completely thermalized system, one would expect that T_B would be constant for all particle species. However, it has been experimentally determined that T_B scales with the mass of the particle. Shown in Fig. 1.3 is the slope parameter measured by NA44 for A+A [60] and p+p [61] collisions. This dependence of the temperature parameter on the mass of the specie can be attributed to an underlying collective velocity experienced by all hadrons leaving the collision. This collective velocity has been dubbed the "radial flow" or "radial expansion" of the system and has a simple physical basis. As the hadronic system expands and cools, particles will tend to be moving in the same direction as their position vector. For example, particles on the left-hand-side of the source will most likely have a momentum directed to the left-hand-side. This effect will lead to heavier particles having a larger perceived temperature than lighter particles which implies that pions, the lightest specie, are much more likely to reflect the "true" temperature of the system at freeze-out.

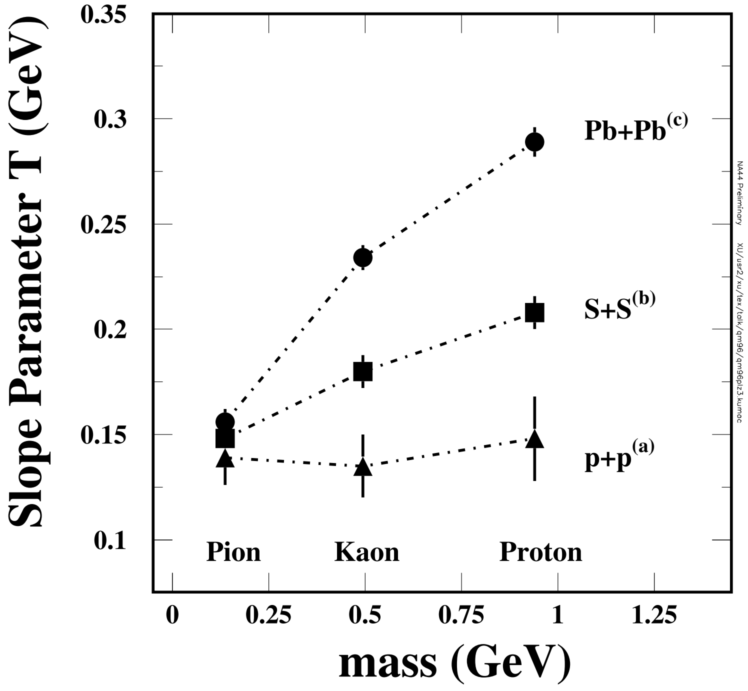

(a) Alper, et al, Nucl. Phys. B100, 237(75),
Guettler, et al, Nucl. Phys. B116, 77(76),
Shuryak and Zhirov, Phys. Lett. B89, 253(80).

(b)/(c) NA44 Preliminary data.

(d) Csorgo and Lorstad, sub. Phys. Rev. C, 95.

$$T = T_{fo} + m\langle\beta_t\rangle^2$$

Figure 1.3: Slope parameter T as a function of particle mass for p+p ($\sqrt{s} = 23$ GeV), S+S ($\sqrt{s} = 19.4A\cdot$ GeV) and Pb + Pb ($\sqrt{s} = 17.3A\cdot$) GeV collisions. Figure taken from [60].

Particle Correlations

While hadronic observables primarily provide insight into the thermal properties of the system at freeze-out, correlations of identical and non-identical particles are studied to gain information of the volume of the system at freeze-out.

The technique of particle correlations was pioneered by the two scientists R. Hanbury-Brown and R. Q. Twiss [12] who used it to determine the size of distant stars by exploiting the quantum characteristics of bosons (in that case photons) which are emitted from the source. In an isotropic source with emitted particles which do not interact with each other, the correlation function reflects the Fourier transform of the particle emission distribution [13]. Therefore, in an ideal case, the correlation of pions from heavy-ion collisions could be used to directly measure the size of the source. Unfortunately, such a signal is disrupted by resonance decays and coulomb effects as well as finite time extents and collective phenomena in the source. As such, though particle correlations have been a significant focus of study in heavy-ion collisions, until recently the physics phenomena which interrupt a simple description have not been well understood. For a review of such studies, the reader is directed to [11, 13].

1.3.2 Leptonic Probes

Leptonic signals have, to date, produced the most promising signals of the QGP [11]. The primary reason for such results is the fact that, while leptons can be produced during all phases of the collisions, from the QGP through the dilute hadron gas, since leptons do not interact via the strong force they can deliver a signal directly from the QGP to the detector that measures them. This direct measure, coupled with theoretical predictions of the properties of lepton sources, make this field of heavy-ion collisions one of the more encouraging future paths of this field of physics [14, 11].

1.4 The Theory of Light Fragment Formation

> *It is a capital mistake to theorize before one has data. Insensibly one begins to twist facts to suit theories, instead of theories to suit facts.* [Sherlock Holmes, in Arthur Conan Doyle's *A Scandal in Bohemia* (1891).]

The purpose of this thesis is to study the properties of heavy-ion collisions utilizing theories of nucleosynthesis (or coalescence) coupled with light fragment data in order to deduce the size and temperature of the system at freeze-out. The effect of a plasma is expected to be hidden in such a study as it was in the studies of isotopic ratios from the big bang [9] described above. However, light fragments (^2H, ^3H, ^3He, ^4He) should be very dependent on the properties of the dilute and thermalized hadron gas at breakup.

In this thesis we will consider in more detail than has been previously the *dual nature* of light nuclei spectra. As was mentioned in Section 1.3.1, since light nuclei are an extreme of the mass scale of ejectiles they are likely to give more detailed information of the radial flow of the system at freeze-out. Specifically, one would expect that the light fragment transverse spectra would reflect a temperature that is much higher than that of protons and pions and therefore, be a finer handle for constraining model predictions of the collective velocity of emitted particles. Furthermore, the production of light nuclei is highly dependent on final state interactions and distances at freeze-out and may be treated similar to a correlation function. In fact, deuteron formation may be directly related to a proton-neutron correlation [33] which probes the volume and collective effects of the system at freeze-out.

Light nuclei have been inherently difficult to interpret due to hadronization and the fact that they are essentially a second order effect, being dependent on the phase space distribution of nucleons at freeze-out. However, this fact ends up being highly useful, because, while a number of models can correctly describe simple hadronic observables such as pions and protons, due to the high sensitivity of fragments to the phase space configuration, a number of them can be discarded because they would fail to reproduce light fragments.

By way of introduction, the following sections will give a brief glimpse of the historical ideas regarding light nuclei production in heavy-ion collisions. In Chapter 5 these models as well as current descriptions will be considered in more detail and quantitative comparisons will be made.

1.4.1 Simple Coalescence Model

Light fragments from heavy-ion collisions have historically been studied via a coalescence model [15, 16] that assumes deuteron formation takes place at freeze-out, that is when all strong interactions have ceased. Since the binding energy of the deuteron is $2.24 MeV$, it is easily broken apart in the "fireball" region where current models show the temperature to be $\approx 150 MeV$ [18, 19]. Therefore, the historical argument for describing deuteron production is to assume that they are formed from the proton and neutron distributions at freeze out. In the original coalescence formulation [15] the probability of forming a deuteron is the greatest when a proton and neutron have a small relative momentum such that we would expect [20]

$$P_d(\vec{v} = \vec{v_d}) \propto P_p(\vec{v_p} = \vec{v_d}) \cdot P_n(\vec{v_n} = \vec{v_d}) \tag{1.2}$$

where $P(\vec{v})$ is the probability of a particle having a velocity $\vec{v}$. The deuteron momentum distribution is then given by

$$E_d \frac{d^3 N_d}{dp^3}(P_d) = B_d \left(E_p \frac{d^3 N_p}{dp^3}(P_p) \right)^2 \tag{1.3}$$

where $P_d = 2P_p$ which can be easily generalized to lighter fragments as

$$E_A \frac{d^3 N_A}{dp^3}(P_A) = B_A \left(E_p \frac{d^3 N_p}{dp^3}(P_p) \right)^A \tag{1.4}$$

where $P_A = AP_p$. B_A is a phenomenlogical parameter known as the coalescence constant and was traditionally in proton-nucleus collisions related to an interplay between the binding energy of the deuteron and the optical potential of the target nucleus [15]. For nucleus-nucleus collisions it was recognized that the idea of a nuclear optical potential was no longer meaningful and Schwarzschild and Zupančič [16] expressed the coalescence parameter as a momentum radius p_0 within which a proton and nucleon pair would coalesce into a deuteron. In this case

$$B_A = \left(\frac{2s_A+1}{2^A}\right)\frac{{R_{np}}^N}{N!Z!}\left(\frac{4\pi}{3}{p_0}^3\right)^{A-1}. \tag{1.5}$$

Therefore, the coalescence parameter in these models is simply related to the momentum difference between corresponding protons and neutrons and is described by a simple step function in the coalescence probability at p_0. Note that no dependence on the colliding system exists in this model which described deuteron and $^3H/^3He$ production very well in nucleus-nucleus reactions at Bevalac [20, 21] energies ($\sim .1 - 1$GeV·A) and in p-nucleus, and p-p collisions at CERN [28] and FNAL [29] energies. For all of these energies, only a single factor was needed to describe the light fragment distributions given the proton spectra. Shown in Fig. 1.4 is a collection of data from these energies as well as AGS measurements in Si + Al and Si + Pb collisions [22]. The B_d parameter is surprisingly constant for a large variety of colliding systems and energies; however, for nucleus-nucleus collisions at AGS energies and above there is a dramatic drop in the coalescence parameter and a strong dependence on the centrality of the collision.

The independence on source size discovered at Bevalac energies can be understood [30] by noting that p-p, p-A and A-A collisions at low energies decouple at a size that is comparable or smaller than the size of a deuteron, $R_{rms} = 2.1 fm$. In this case, only the relative momenta of the particles determines the probability of forming a deuteron, whereas if the source itself

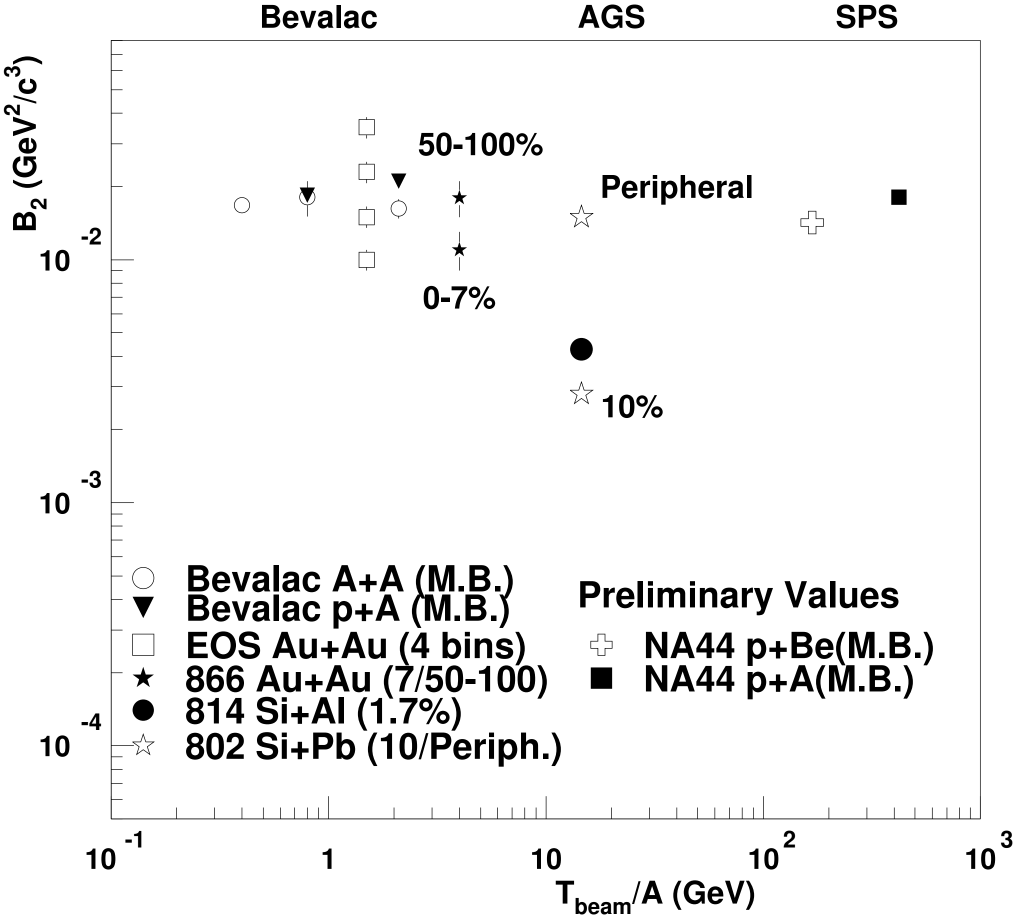

Figure 1.4: B_2 for a variety of systems and energies. The values in parenthesis are the centrality cuts, where 'M.B.' corresponds to minimum bias events. The data are taken from [20, 21, 22, 27, 28, 29]

is much larger than the deuteron radius than the relative distance between the proton and neutron must also be taken into account. Therefore, even though at Bevalac energies they collided heavy nuclei as well, the fact that few secondary particles are produced means that the collision volume does not increase significantly until it freezes out; similarly at higher energy p-p and p-A collisions, though secondary particles are produced, the size of the system is still comparable to the deuteron rms radius. However, at AGS energies and above, a large number of secondary particles are produced (the pion yield is equivalent to that of the nucleon) which will tend to drive the system to larger freeze-out volumes before it decouples. This will cause protons and neutrons to freeze-out at distances beyond the mean radius of the deuteron such that volume effects need to be added to a conceptual description of deuteron formation.

1.4.2 Matrix Models

In order to account for the increase in source size beyond that of the deuteron rms radius in relativistic heavy-ion collisions, several models have been developed. One non-relativistic model [36] utilizes a density matrix formalism to relate the coalescence volume to the internal wave function of the composite particle and the spatial distribution of nucleons. This model assumes that the momenta and positions of the nucleons are uncorrelated at freeze-out and deduces that

$$B_d = \frac{3}{4}\frac{(8\pi)^{3/2}}{Z!N!}\left[\frac{\nu_d\nu}{(\nu_d+\nu)}\right]^{3/2} \tag{1.6}$$

where $\nu_d = .20 fm^{-2}$ is the Gaussian wave function parameter and ν is directly related to the nucleon freeze-out radius by

$$R_{rms} = (3/2\nu)^{1/2}. \tag{1.7}$$

Other models [32] also utilize a wave-function description and a density matrix formalism to describe deuteron formation. Many of the models are similar though, with the exception of large cascade codes [30, 37], none of them account for collective expansion. Further, though there have been some attempts at a fully relativistic treatment [38], the generalization to relativity is non-trivial because of difficulties in the proper relativistic treatment of bound states [32].

1.4.3 The Three Body Problem

People don't go there anymore. It's too crowded. [Yogi Berra]

From simple energy-momentum conservation considerations, it is impossible for two objects to coalesce into a bound state of smaller mass without a third body. Therefore, a consistent theory of deuteron production should ideally account for 3-body interactions. Butler and Pearson [15] in their early studies of deuteron formation, considered p-A collisions as a neutron pick-up reaction that included an interaction between the optical potentials of the proton and the target nucleus. They argued, that explicit mention of a third body was unneccesary since it was implicitly a part of their calculations. As we have noted above, in A-A collisions the optical potential view is invalid; theorists have therefore attempted to bypass full 3-body calculations by considering deuteron production to occur via the coalescence of a proton and a neutron interacting with the rest of the fireball. One exception to this rule occurs in a set of calculations by Beyer and Röpke [31] where they provide a full 3 body formalism in dense nuclear matter. Their calculations are for energies on the order of $100 MeV$, not applicable to our collisions, but they find that the effect of the medium becomes smaller at higher scattering energies, translating to a negligible effect at AGS energies.

Mrówczyński [32] argues that, since the collision passes through a fireball stage, the uncertainty in the momenta of all the particles is enough to account for the excess energy in deuteron formation, thus dispensing of the need for a third body. However, Leupold and Heinz [35] note that this view is incorrect since the p-n wave function overlap with the deuteron bound state is identically zero even when the coalescing proton and neutron are required to live inside of a fireball with finite extension R. Instead, they [35] attempt to describe deuteron production by employing an effective nucleon mass in the nuclear medium. This methods appears to be more correct in the initial assumptions, yet under-predicts the coalescence parameter compared to other models by 3-4 orders of magnitude.

Generally, theories of light fragment formation have remained an intuiging sideshow since the first collisions of heavy ions. However, a complete model which can correctly account for a relativistic, 3-body interaction in a nuclear medium interactions is still forthcoming.

1.4.4 Thermal Models

Finally, it should be noted that descriptions of deuteron yields via thermal models have also had some success at AGS and SPS energies [18, 40]. The applicability of such a model to describe deuterons seems questionable since it fails to account for changes in deuteron formation due to collective motion, possibly a significant component to the overall yield [30]. However, the fact that it describes the yields of all measured hadrons from heavy ion collisions to within a factor of two makes its results intruiging. Perhaps the good fortune of thermal models in predicting deuteron production, however, are due to an underlying physical process of hydrodynamics and thermodynamics which result in the two models being identical. We will study this and other questions further in Chapter 4.

1.5 Innovation

In this thesis light fragment spectra from Au + Au collisions at AGS energies of 11.5 GeV/nucleon are presented. Specifically, ^{2}H, ^{3}H and ^{3}He at mid-rapidity and ^{2}H and ^{4}He at beam rapidity are measured and described in the context of a thermal model.

Despite the numerous theories regarding deuteron formation and the promise of the light fragment yield being sensitive to the volume at freeze-out, at AGS energies, it will be proven in the following that the models outlined above result in unrealistic conclusions, overpredicting the volume of the system by at least a factor of 3.

However, measurements of thermal parameters describing the source will be extended, quantified and made more precise as regards their relation to light fragment production. Simple and complex models with light fragment formation as an afterburner are studied and the strong dependence of deuteron formation on source parameters is taken advantage of for the first time. Using this simple model with coalescence assumptions, the volume of the system at freeze-out is directly measured using the deuteron yields.

Chapter 2

Experimental Apparatus

E877 was a fixed target experiment at the Brookhaven National Lab (BNL) Alternating Gradient Synchrotron (AGS). Its progenitor, E814, was initially proposed in 1985 with the expressed purpose of exploring the characteristics of central heavy-ion collisions and the phenomena of coulomb dissociation in peripheral collisions. The upgrade in 1993 to the E877 apparatus has since focused its attention on the measurement of transverse energy E_T and the physics of collective flow in conjunction with the identification of single particle spectra and identical particle correlations in heavy ion collisions at $\approx 10 GeV$.

In order to make these measurements of hadrons, the experiment primarily consists of three components: (1) a set of scintillators and silicon detectors for beam definition; (2) a near 4π calorimetry coverage, providing global event properties; and (3) a forward spectrometer, allowing for measurements of particles at low transverse momentum, p_T. Figure 2.1 provides a schematic diagram of the E877 experimental setup for the 1994 run.

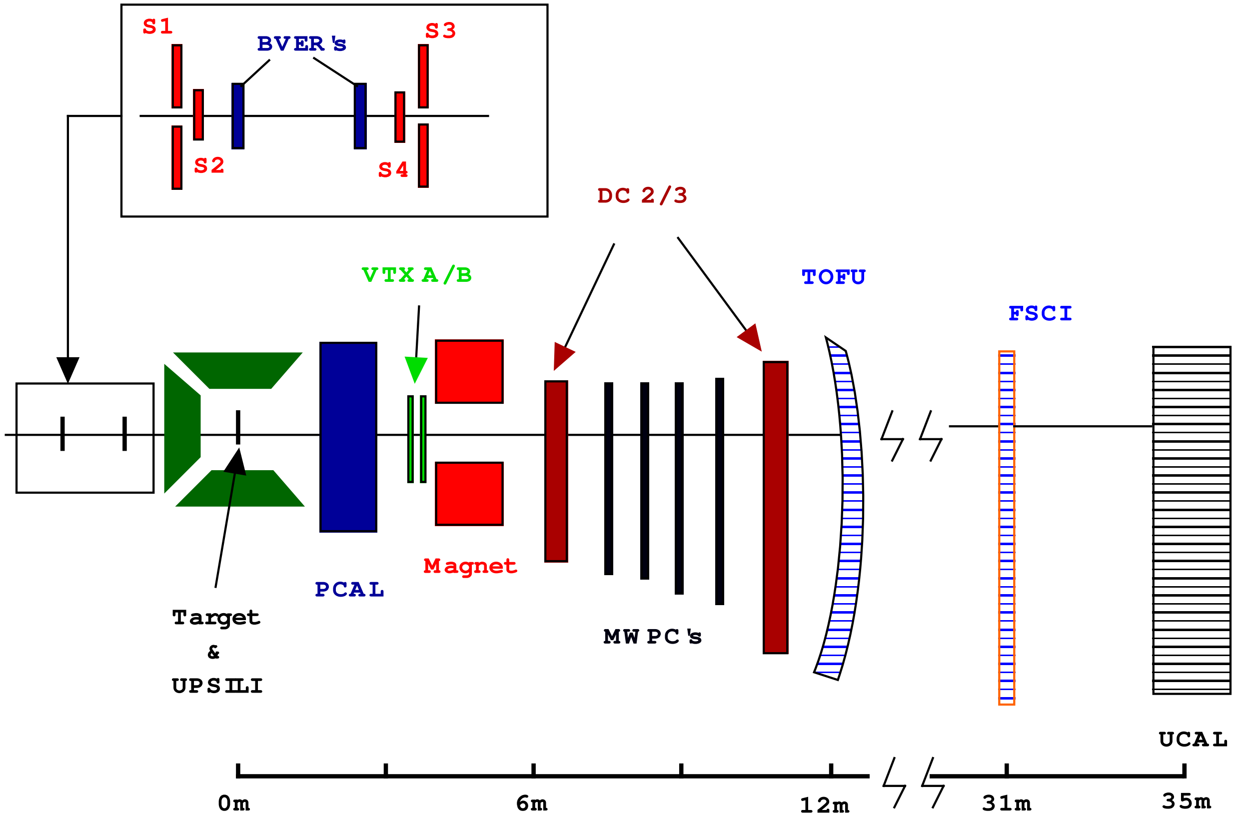

Figure 2.1: E877 setup for the 1994 run

In this chapter we will discuss the different parts of the experimental apparatus and justify their use. Section 2.1 provides a brief description of the AGS facility; Sections 2.2-2.4 describe each of the three aforementioned components of the experimental apparatus as it was in 1994, the year in which the data in this thesis was collected.

2.1 The Alternating Gradient Synchrotron

The process of producing relativistic heavy-ions is multi-step and includes stripping the atom of its electrons and accelerating it. The AGS facility fiscal year '94 operation configuration at BNL is shown in Fig. 2.2. Ions of ^{197}Au are accelerated in the Brookhaven tandem Van de Graff to an energy of $\sim 1A \cdot MeV$. The Au ions exit the tandem and are passed through a thin carbon foil which strips off valence electrons. The ions are subsequently led through the heavy-ion transfer line to the AGS Booster. The Booster accelerates the ions to an energy of $\sim 200A \cdot MeV$, through further foils to completely strip the Au ions and injects them into the AGS where they are accelerated to a final momentum of $\sim 11.5A \cdot GeV/c$. Finally, the beam is extracted to our experimental area via the C5 beam line. The beam intensity was about 10^5 particles per spill, or bunch of Au ions, with a repetition rate of 3.6 *sec* and a duration of 1 *sec*.

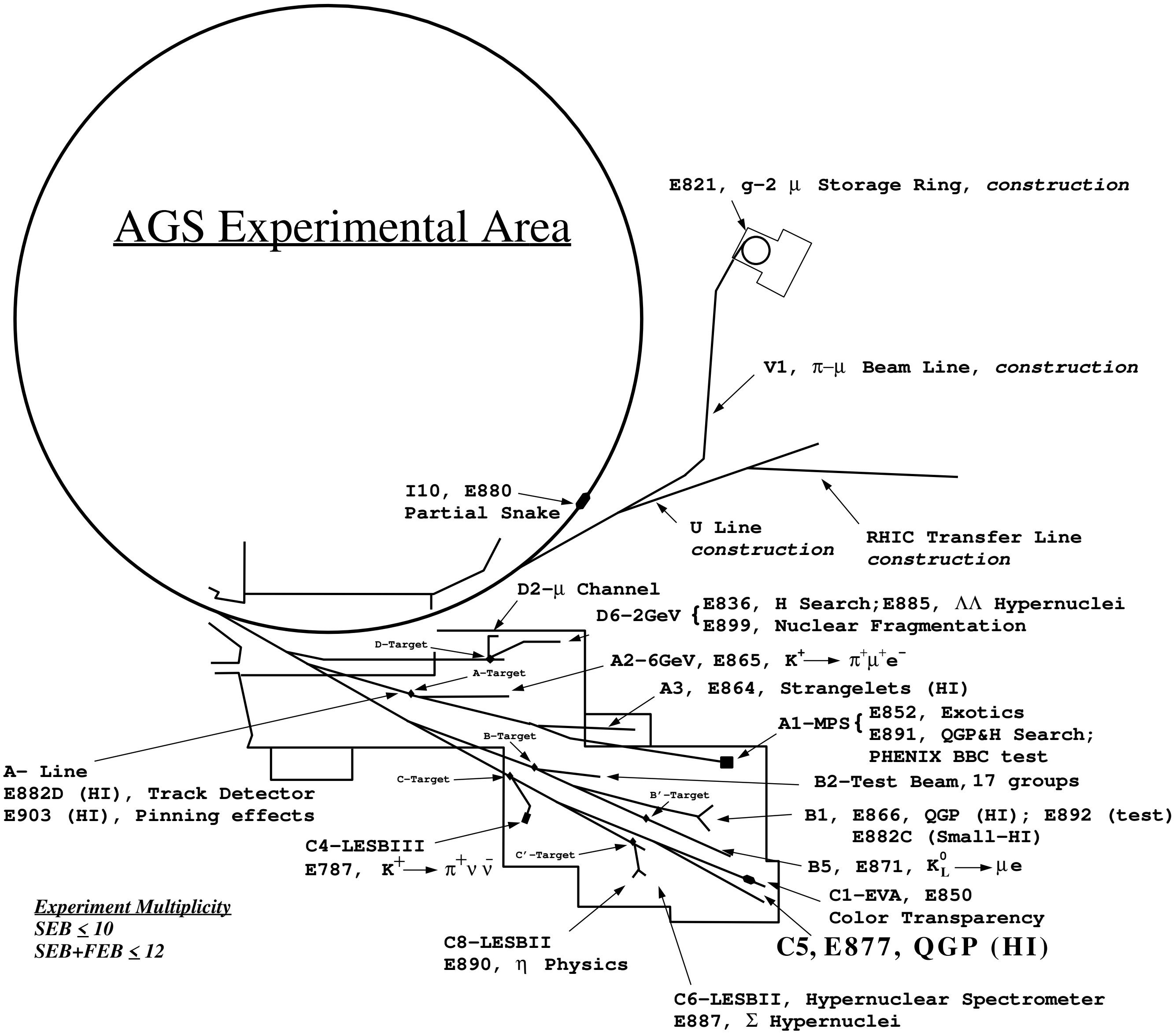

Figure 2.2: Layout of the Alternating Gradient Synchrotron experimental area for the fall 1994 heavy ion run.

2.2 Beam Definition

In order to confirm the beam composition and determine its momentum and angle at the target, a number of detectors are placed upstream of the target. The utility of these detectors arises from several considerations. First, though the momentum of the beam is fairly well known [56], since the momentum of all tracks in a collision should be measured with respect to the beam angle, this variable should be well defined prior to the interaction region. Also, though the beam extracted from the AGS is very pure since improper charge or mass states will not collect into a stable orbit, the extraction process and the transit of the beam through the C5 line to the experimental area may introduce impurities into the beam. Therefore, also needed is a measure of the beam isotopic contributions so that incorrect charge and mass states can be excluded from the data set. Finally, since some detectors require knowledge of the time of the collision for particle velocity measures, the time of the interaction should also be defined

The following sections will deal with these dilemmas. To reject double-beam events, measure the incoming beam angle, and define the time reference for the experiment, there are several detectors prior to the nuclei interaction region: four plastic beam scintillators, two silicon microstrip detectors, and a silicon semiconductor detector.

Beam Scintillators (BSCI): Those beam particles that do not have similar trajectories as the majority of the ^{197}Au projectiles may have resulted from upstream interactions or may simply be a Au nucleus beyond the bounds the collimated beam. As such online cuts on these variables were made to remove unwanted beam particles from the data set.

In order to do this, E877 has placed upstream of the target a series of four plastic scintillators (S1, S2, S3, S4) for good-beam definition, *i.e.* directed towards the target. Furthermore, these detectors are used for a time reference definition which sends a "start" signal to the other detectors in the experiment. These scintillators are described in detail elsewhere [42, 43]. Scintillators S1 and S3 are donut-shaped veto detectors with photomultiplier read outs while scintillators S2 and S4 are ellipsoidal detectors placed at 45^o; they are at 45^o in order to allow the scintillated light to reach the photomultiplier tubes with minimal reflections and ellipsoidal to fill the circular hole in S1 and S3. The beam logic, then requires coincidence of $\bar{S}1 \cdot S2 \cdot \bar{S}3 \cdot S4$. Fast rise time phototubes are utilized on S4 such that it may also be used as a high precision measurement of the interaction time [42] with a typical Gaussian sigma of $\sigma = 35 - 40 psec$

Beam Vertex Detectors (BVER): For determining the momenta of all particles downstream with respect to the beam, two silicon microstrip detectors measuring the beam angle in the xz-plane at the target are located between S2 and S4. The detectors are each composed of 320, $300\mu m$ thick strips with a $50\mu m$ pitch and a multiple-scattering dominated resolution of $\sim 40\mu rad$ of the incident beam angle and $\sim 300\mu m$ in the x coordinate of the beam at the target [45]. The BVER's do not need to provide a y-position at the target for two separate reasons. The first is that the AGS provides the beam to us strictly horizontal with major deviations occuring in the x-z plane from the construction of the beam line. The second is that the y-resolution of our detectors downstream (the DC's and TOFU) is large enough that any reasonable variation in the beam y would result in no measurable difference down stream. The BVER's are also used to tag those events in which two or more particles struck the target within the same 1 μs bin, beyond the response time of our detector.

Upstream Silicon Detector (SILI): In order to eliminate beam particles with incorrect charge number, perhaps due to Coulomb excitation or upstream interactions, a silicon semiconductor is located 2.5 cm before the target with a much better pulse height resolution than the scintillators. Cuts on the deposited energy in this detector effectively eliminates these unwanted interactions from our data set.

2.3 Calorimetry: Global Event Characterization

From one Au + Au central event, the number of pions and nucleons of each isospin is approximately 150. In order to quantify the attributes of these collisions with such a large number of particles streaming from the collision zone we have implemented two large calorimeters which are highly segmented. Together these detectors cover most of 4π in the center-of-mass frame and can identify the reaction plane, or direction of the impact parameter vector[1], as well as quantify a number of global variables. The exact use of the calorimetry will be discussed in Chapter 3 but their physical attributes are discussed below.

Target Calorimeter (TCAL): A diagram of the TCAL is shown in Fig. 2.3. It consists of 832 NaI(Tl) crystals which surround the target with a polar coverage of $48^o < \theta < 135^o$ ($-0.5 < \eta < 0.8$ [2]). Each crystal has a depth of 13.8cm, or about 5.4 radiation lengths (.34 hadronic interaction lengths), and thus contains a fraction of the total transverse energy directed into it. The TCAL is discussed in detail elsewhere [50].

Participant Calorimeter (PCAL): The PCAL is a finely segmented lead/iron/scintillator consisting of 16 azimuthal sections, 8 radial towers, and 4 depth sections,schematically shown in Fig. 2.4. It covers a polar angle of $1^o < \theta < 47^o$ ($0.83 < \eta < 4.7$). There is a small opening in the PCAL ($-136 < \theta_x < 16mrad$; $-11 < \theta_y < 11mrad$) with iron wedges along the inside which define the opening of the forward spectrometer, see Sec. 2.4. The PCAL is described in detail elsewhere [49].

---

[1] The impact parameter vector b is defined as that vector between the axes of the two colliding nuclei. An impact parameter of zero corresponds to an absolute overlap between the two nuclei and an impact parameter greater than 2R, with R the radius of the nuclei, corresponds to a miss

[2] The pseudo-rapidity variable, $\eta \equiv \tanh^{-1}(\cos\theta)$, is an approximation of rapidity, y in the limit of $v \rightarrow c$.

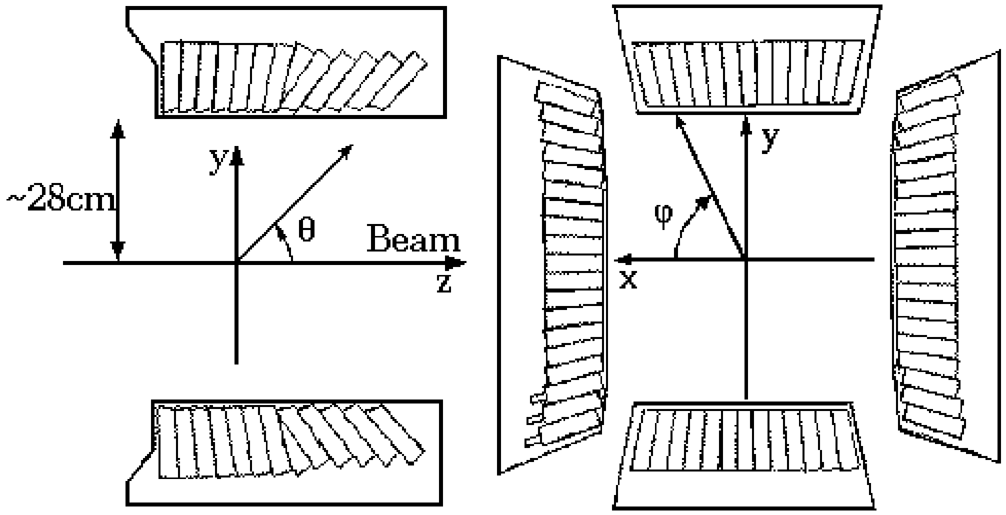

Figure 2.3: Side (left) and end (right) views of the TCAL.

2.4 Forward Spectrometer

Finally, after the beam has been defined and the global properties of the collisions have been set, one would like to reconstruct the momenta and time-of-flight of the particles which pass through the collimator and enter the forward spectrometer, which measures the characteristics of individual tracks. In order to do this, several detectors downstream are used.

To measure the momentum of the tracks, the collimator leads to a magnet with a number of detectors beyond it. Since the center-of-mass of our system is at a rapidity of 1.6 (which corresponds to 5.7 GeV per nucleon) we do not need to worry about excessive multiple scattering from the detector gases in the particle's trajectory. The intervening volume between the calorimeter and the downstream detectors is filled with helium bags, though passage through air would not degrade our measurements significantly. By measuring the point and

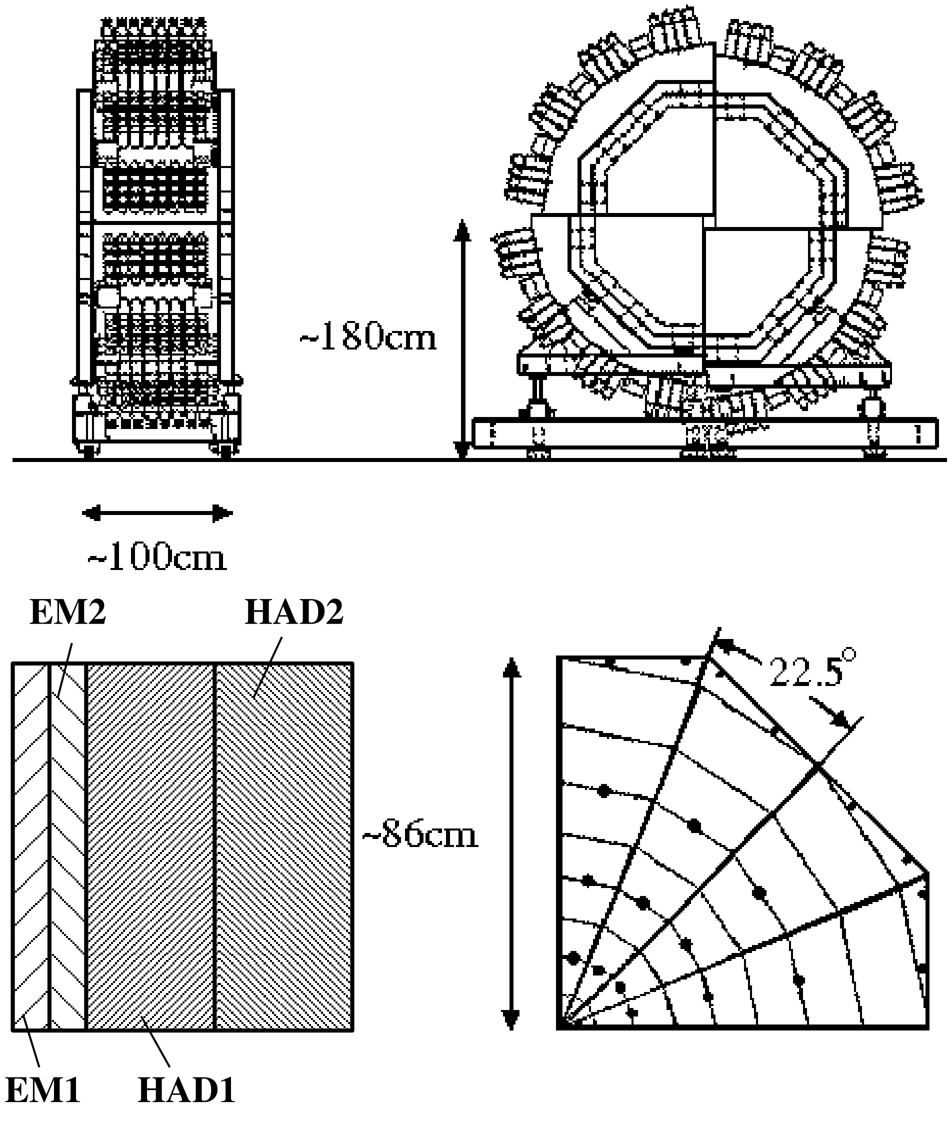

Figure 2.4: Side (upper-left) and end (upper-right) views of the PCAL along with schematic representations of the segmentation directly beneath.

angle of intersection in two of the downstream detectors (the Drift Chambers) and assuming that they originated from the target, the momentum of each track can be reconstructed.

To measure the time of flight a simple hodoscope wall was instrumented approximately 12 meters from the target. The velocity of the ejectiles from the collision are traveling at a low enough velocity that the time-of-flight, and hence β can be determined rather accurately. This method, coupled with the hodoscope wall determination of the charge, each track can be preliminarily identified according to specie(see Section 3.8).

In this section the downstream detectors will be outlined; a discussion of their calibration and use will wait until Chapter 3.

Vertex Chambers (VTXA and VTXB): A set of wire chambers with a highly segmented cathode pad readout are placed 2 m from the interaction region separated from each other by 25cm. These chambers were implemented for the 1994 $Au+Au$ run in order to aid in reconstructing tracks in this high multiplicity reaction and to resolve those tracks which did not pass through the origin of the collision due to either downstream interactions or the decay of hyperons. Each pad plane is instrumented with 508 channels which provide a position resolution of $100\mu m$ horizontally and $1.44mm$ vertically, resulting in a resolution of secondary vertices track-able to within $\frac{1.71}{tan\theta}mm$ of the target. Detailed information can be found in [52]. These detectors were not used in the analysis for this thesis.

Magnet: The next object in the forward spectrometer is an analyzing magnet which can be run in two polarities in order to study the systematics of the forward spectrometer and acquire sufficient statistics of positive and negative particles. The collimator is placed before the magnet, with a smaller opening than the magnet aperture ($-134 < \theta_x < 16 mrad$, $-11 < \theta_y < 1 mrad$), thus causing all secondaries to be produced prior to the field. This configuration results in a small background in the spectrometer since the produced secondaries have a lower energy than the primary particles and, hence, they tend to be either caught in the magnetic field or swept by the magnet out of the spectrometer. Additional offline cuts on tracks that passed near the magnet edge reduce this background further. (See Chapter 3.)

Drift Chambers (DC2/DC3): Two drift chambers provide x and y information of the tracks and hence determine the rigidity of each track; each drift chamber is composed of six planes of wires which measure the position in the bending plane of the magnet, *i.e.* the xz-plane, with a resolution of $250\mu m$ ($300\mu m$) for DC2 (DC3). Furthermore, DC2 and DC3 contain a cathode pad plane segmented into a series of chevron-shaped pads running along the anode wires which provide y measurements of charged particles with a resolution of typically a few percent of the pad size; this results in y-resolutions of 2.3-15 mm in DC2 and 4.3-36 mm in DC3 depending on the pad size. For more detailed information regarding the drift chamber see [53].

Multiwire Proportional Counters (MWPC1,2,3,4): The MWPCs are a series of wire chambers with vertical anode wires spaced 5.08 mm apart. They are not used for determination of particle rigidity but instead are used for track confirmation in the high multiplicity environment of $Au + Au$ collisions. Each wire is instrumented with only a discriminator and, therefore, this detector has a resolution equal to the wire spacing.

Time of Flight Upstream Wall (TOFU): The TOFU is an array of 160 plastic scintillators aligned vertically and placed behind DC3; it provides a resolution of $85ps$ in time of flight measurements and a $1cm$ vertical position resolution. For more information, see [54].

Forward Scintillator (FSCI): The FSCI is another hodoscope wall which also measures the time of flight but with a resolution of $350ps$. This lower resolution, coupled with the fact that it covers less phase-space meant that it was only utilized in this analysis in a study of TOFU systematics (see Chapter 3).

CsI/UCAL: A CsI photon detector, located $35m$ from the target at an angle of 4.8^o for measurement of photons from the collision, and a uranium calorimeter (UCAL) behind it, which provides neutron rejection in those photon measurements [51], were not utilized in this analysis.

Chapter 3

Data Reduction

> *There is a theory which states that if ever anyone discovers exactly what the universe is for and why it is here, it will instantly disappear and be replaced be something even more bizzare and inexplicable. There is another theory which states that this has already happened.* [The Restaurant at the End of the Universe]

Data reduction is aptly described as the process of reducing a raw collected event, which includes signals from individual detectors, to a set of necessary and sufficient variables which can describe the collision. In our case such a set includes (1) a track list of particle specie, momenta, and time of flight and (2) global characteristics of the event including the centrality, reaction plane vector, and beam definitions.

This process of accumulating information from detector channels and translating it to a characterization of each event will be discussed in this chapter. Section 3.1 outlines the reduction of this collected data size to a manageable set and Sections 3.2 and 3.3 describe the event characterization cuts. Section 3.4 defines the calorimetric variables used in this thesis. Sections 3.5-3.7 describe the process of reconstructing momenta and velocities of particles given their passage through the downstream detectors and Section 3.8 specifies the procedure for identifying the specie of each track given these measurements. Finally, Sections 3.9 and 3.10 will cover how the identification of specie in the entire data set leads to a production of the invariant cross-section of this specie as a function of p_t and y.

3.1 Raw Data Tapes

The 1994 data set is approximately 10 million central events. For each event the pulse height and/or time of each detector channel was recorded, regardless of whether or not it was hit. Since most channels are not hit, the corresponding space on 8mm magnetic tapes of the entire 1994 run is 540 Giga-bytes, far too large to economically save in one central place and rescan according to the needs of individual analyses. Therefore, the first step in translating the raw data tapes into characterizations of heavy-ion collisions consists of passing through the list of channels and removing those that are devoid of information. Simultaneous with this process, the collection of channel hits is translated into a list of tracks with corresponding positions and momenta, as will be described in later sections. After this reduction and simplification pass the data size was reduced to 15 GB, a fraction of the raw collected space, but sufficient information for all physics analyses.

The final data is written in a CERN library defined format, termed an n-tuple, which is simply a transparent way of listing arrays of variables. This format is widely recognized by the high-energy physics community as an effective way to save large amounts of data for further and multiple analyses. An added benefit of such a format is that it is trivial via standard tools such as PAW, to quickly plot two or three variables versus one another under various conditions. However, in the final analyses, a Fortran code named STEP2 reads the n-tuples and performs all necessary calculations without the overhead that would be required in PAW for such detailed and multiple calculations.

3.2 Online Event Characterization Cuts

To create a clean sample of events, various cuts are performed on global variables. As was described in Chapter 2, during data collection the beam trigger logic of $\bar{S}1 \cdot S2 \cdot \bar{S}3 \cdot S4$ cuts on upstream interactions and incorrect rigidity beam particles. A minimum deposition of energy in the PCAL, corresponding to $\sim$ 1 GeV, ensures an interaction of the Au beam particle in the 2% interaction length Au target. Furthermore, to further reject double-beam interactions, a first level trigger discards those events where another beam particle entered the spectrometer within $1\mu s$ prior to or following the projectile of interest.

A second-level trigger analyzes each event that has passed the good beam particle definitions described above. This trigger must decide if the event is interesting enough to write to tape or should be quickly discarded in order to save time for the more interesting events. The trigger system does this by analyzing the signals from a few detectors which will be most representative of the user's definition of a "good" event. Since any events which may correspond to a deconfinement stage or may reflect the most thermalized distribution are those that are the most violent (the largest centrality), the E877 trigger was set to accepts those events which have the largest transverse energy as measured in the calorimeters. As high centrality events are more rare, the online second-level trigger performs a fast digital sum of the calorimeter measurements with FERA ADC's which is compared to three preset thresholds. Events from the highest threshold are all saved to tape, as are down-scaled factors of other calorimeter energy regions. The trigger was set with the goal of saving equal statistics of all centralities to tape instead of allowing a disproportionate number of low centrality events. Figure 3.1 shows the down-scaled E_T distributions for Au on Au events in both the PCAL and the TCAL for the 1994 analysis. The points of down-scaling are clearly noticeable in the PCAL distribution. Note, however, that the TCAL E_T distribution has smoother edges since it is not the trigger source and instead relies on the PCAL for its good-event definition.

3.3 Offline Event Characterization Cuts

After the events have been saved to tape and in the process of extracting the physics from the data, a second pass is made over event characterization variables and more stringent cuts are made in order to remove unwanted events.

The raw values of event characterization variables and the imposed offline cuts are shown in Figs. 3.2 and 3.3. In Fig. 3.2, the BSCI and BVER distributions are shown. These two cuts help to ensure that only one beam particle

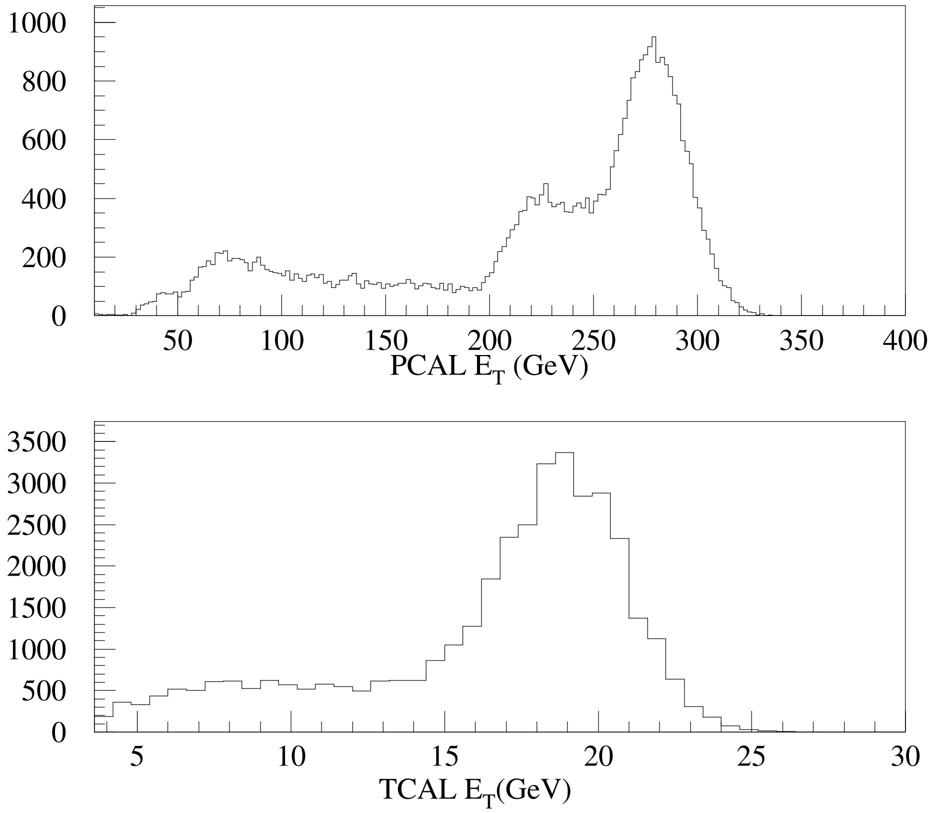

Figure 3.1: E_T distribution in the PCAL (top) and the TCAL (bottom) for $Au + Au$ events.

Cut Variable	% of Accepted Events
BSCI1	95.5%
BSCI2	95.4%
BVER1	95.4%
BVER2	85.9%
SILI	92.7%
X-TARGET	99.8%

Table 3.1: Event characterization efficiencies. The percentage of accepted events for each event cut.

entered the apparatus during the analysis of a collision. The BSCI distributions show a clear two humps, the upper one corresponding to the energy of two beam particles. The number of BVER clusters is also clearly peaked at 1, though 0, 2, and 3 clusters are also seen. Therefore, cuts on the first bump in the BSCI's and on 1 cluster in the BVER ensures that only 1 beam particle entered the apparatus. In Fig. 3.3 the SILI distribution and the projected position and angle of the beam at the target are shown. Cuts on these variables ensure that the beam particle struck the target at an appropriate angle. The PCAL vs TCAL E_T distribution, also shown in Fig. 3.3, can be used as a final cut for a good event by eliminating those events that have an unreasonable zero energy deposition or a spike. Cuts on the correlations between the two measures of transverse energy also can cut on double beam events.

Table 3.1 shows the percentage of accepted events for these various cuts. Notice that most of these cuts are above 90% efficient and are highly correlated such that the percentage of accepted events after all of these cuts is close to 80%.

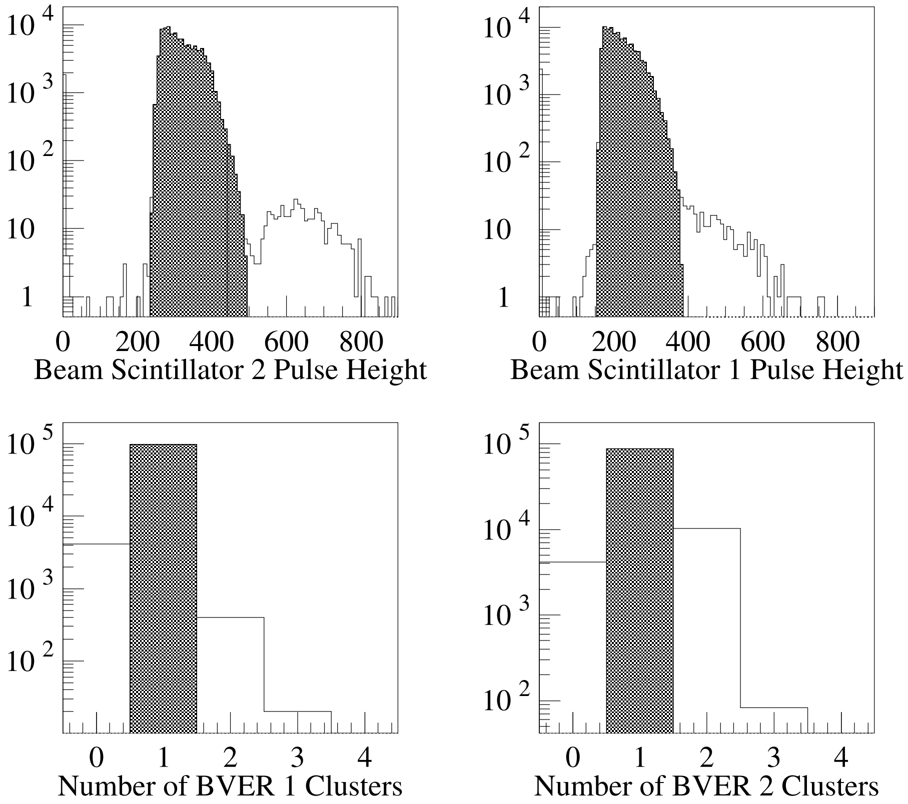

Figure 3.2: Offline cuts of BSCI pulse height (in channels), and number of clusters in each BVER. The shaded region outlines those events which pass the offline cuts.

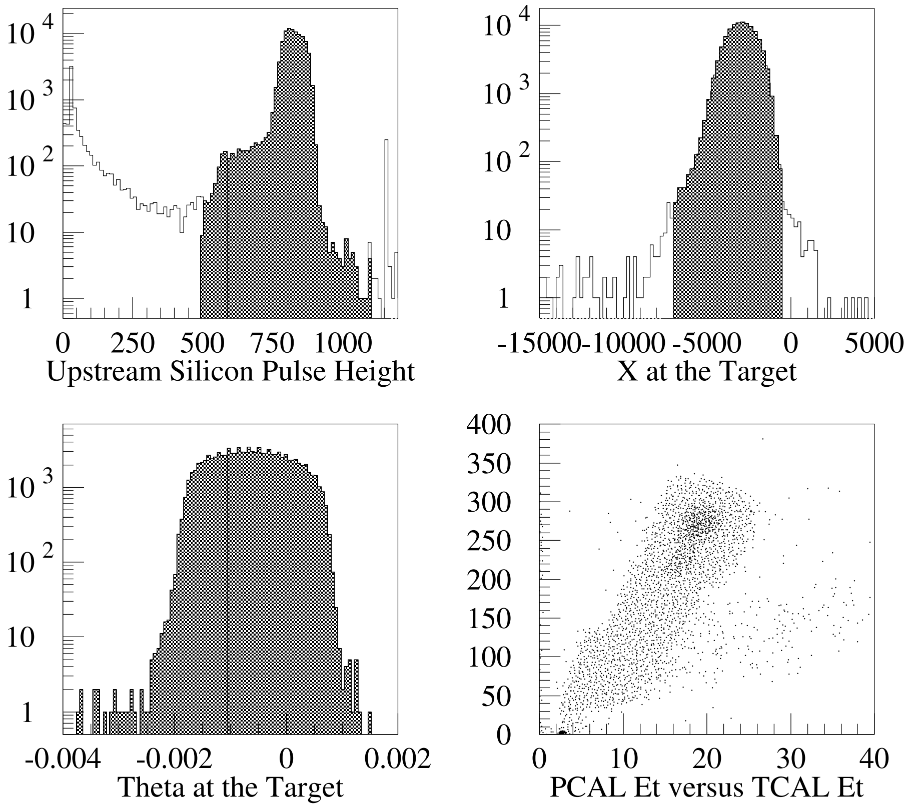

Figure 3.3: Offline cuts on the upstream silicon detector pulse height (in channels), the projected position (in microns) and angle of the beam (in degrees) at the target and the correlation between PCAL and TCAL E_T. The shaded region outlines those events which pass the offline cuts.

3.4 Calorimetric Measures

The calorimeters which cover most of 4π describe the global properties of a heavy-ion collision. In order to quantify the attributes of an interaction for future comparison, two variables are defined for this analysis which adequately describe the global collision dynamics. The total transverse energy is defined as

$$E_T = \sum_i e_i sin\theta_i \tag{3.1}$$

where e_i is the energy deposited in one cell of the calorimeter and θ_i is the polar angle of the cell with respect to the beam axis; the sum is performed over all cells. The transverse energy provides a handle on the relative violence of the collision by providing a measure of the transfer of longitudinal momentum (the initial configuration) to transverse momentum. Those collisions with a large transverse energy are believed to have the largest number of participating nucleons, or highest centrality, and thus are more likely to have the highest energy densities. To embolden us in our simple belief that transverse energy relates to the centrality of the collision, results from the cascade code RQMD relating E_T to the impact parameter, taken from [47], are shown in Fig. 3.4. Notice that the transverse energy and impact parameter are highly correlated, reassuring us that a cut on large transverse energy is similar to a cut on small impact parameter.

We then use the transverse energy as a measure of the centrality of the collision by noting that

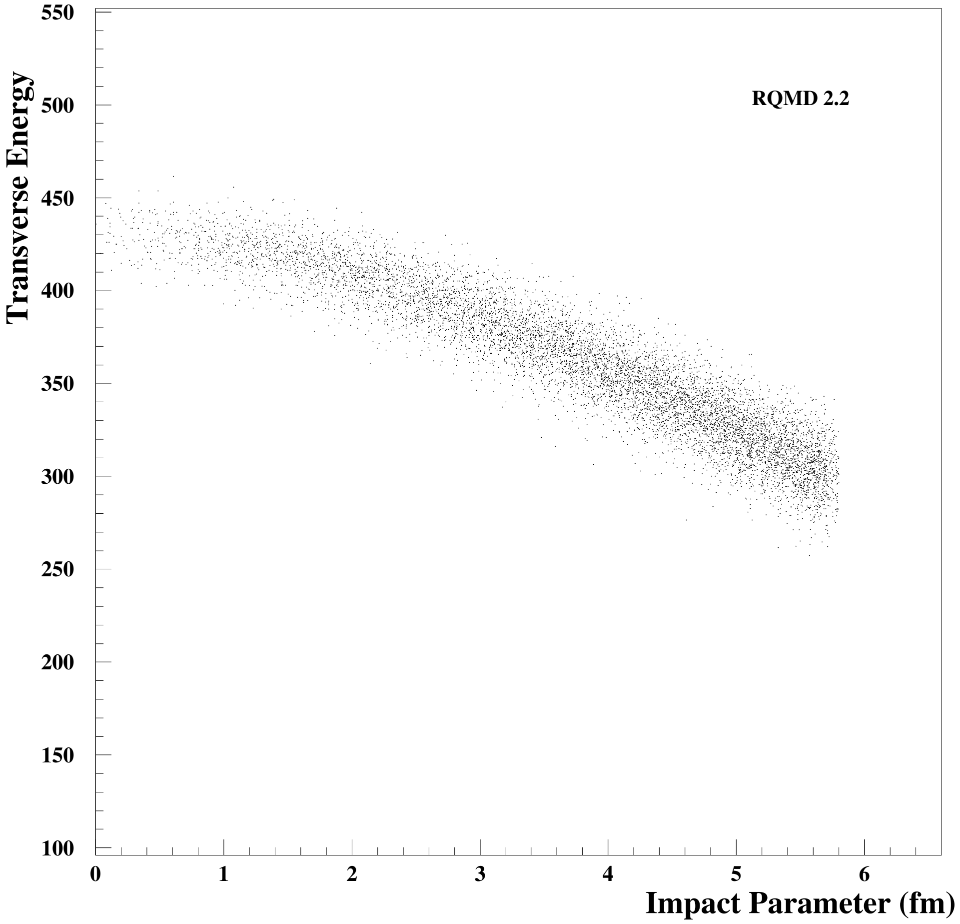

Figure 3.4: The dependence of produced transverse energy on impact parameter in RQMD version 2.2. Taken from [47].

$$\frac{d\sigma}{dE_t} = \frac{s}{n_t B}\frac{dN}{dE_t} \tag{3.2}$$

where σ is the cross-section, B is the incident number of beam particles, s is the trigger down-scale factor ($s \leq 1$), and n_t is the number of target atoms per unit cross-sectional area. In order to provide a trans-experiment quantity, we define the geometric cross-section as the fraction of Eq. 3.2 integrated, and not the impact parameter (b) as we have no direct measure of it.

$$\sigma_{top} = \int_{E_t}^{\infty} \frac{d\sigma}{dE_t} dE_t \tag{3.3}$$

However, assuming the relation between b and E_T is strict, the correlation between E_T and the number of interacting nucleons can be calculated. This calculation is shown in Appendix E.

Therefore, the ratio of σ_{top} to the total cross section integrated over all transverse energies, σ_0, provides our characterization of the centrality of the collisions; this quantity is independent of the absolute value of σ_0.

Beyond characterizing the centrality of the collision, calorimetric measures can also define the reaction plane, the azimuthal angle into which the nuclear reaction deposited the majority of its energy in the forward direction. This asymmetry results from the collision dynamics in that the two colliding nuclei are most often offset from one another and do not collide head on; they have some non-zero impact parameter. This initial asymmetry in the collision is translated through the collision in such a way that more energy will be deposited at an angle in the same plane as the impact parameter vector and the beam axis. The reaction plane is extracted with the calorimeters by performing a Fourier analysis on the transverse energies measured by the cells [44, 48]. The Fourier coefficients are defined by

$$A_n = \frac{\sum_i {e_T}^i cos(n{\phi_i}')}{\sum_i {e_T}^i} \qquad (3.4)$$

$$B_n = \frac{\sum_i {e_T}^i sin(n{\phi_i}')}{\sum_i {e_T}^i} \qquad (3.5)$$

where ${\phi_i}'$ is the azimuthal angle of the cell. In the analyses of the reaction plane and studies of flow [48, 77, 78], the full Fourier coefficients are studied and multipolarities are analyzed. However, for this thesis, the first Fourier coefficient holds the information concerning the azimuthal orientation of the collision via

$$\psi_r = tan^{-1}(\frac{B_1}{A_1}) \qquad (3.6)$$

and is the only part of the azimuthal distribution that we will use.

3.5 Drift Chamber Calibration

Now that the global characteristics of the collision have been determined, the downstream detectors are used to reconstruct the momentum and time-of-flight of each trajectory. The drift chambers will reconstruct the former.

As described in Chapter 2, the drift chambers (DC2/3) measure the position of a charged particle along its trajectory. This feat is performed via two separate methods. First, the x-position is measured by determining the time at which an avalanche is induced on the wire in the six planes of each drift chamber; this time is translated to a distance, via a drift velocity. Secondly, the pad section of each drift chamber determines the y-position by measuring the induced charge on the chevron pads.

For both of these reconstructions of position, the raw data is itself used to calibrate the detector, rather than relying on a simulation. The method of calibrating these detectors for the '93 and '94 runs is described in detail elsewhere [47, 56]; a condensed overview of the method is provided here.

For the drift chamber, each channel has an overall time offset which arises due to varying discriminator thresholds, cable delays and other effects. Therefore, mean measured times of all drift chamber channels are aligned to cancel such effects. The position of the signal from the wire is corrected directly from the data. In an ideal case, when the drift velocity would be constant as a function of distance, the distance from the wire can be easily determined via a linear extrapolation to the maximum time and the drift cell size. However, the drift chamber time spectrum is non-linear due to the fact that the electric field present in it is not constant. In this case a map from the measured time into distance from the time spectrum can be determined by:

$$d = D\frac{\int_0^{t_{meas}} \frac{dN}{dt'} dt'}{\int_0^{t_{max}} \frac{dN}{dt'} dt'} \tag{3.7}$$

where t_{meas} is the measured time, d is the distance, D is the drift cell size, and t_{max} is the largest measured time. Utilizing this method, rather than a simple constant drift velocity approximation results in a 30% improvement in position resolution in the middle of the cell and eliminates any artificial wire-structure (or "scalloping") from the reconstructed position spectrum [47].

The seventh plane of each drift chamber, the pad plane, is calibrated via a similar method. First, since the signals are amplified prior to digitization, a test pulser was used to calibrate the gain of each channel prior to each physics run. Then, ideally, the position of each track could be calculated from

$$y = \frac{\Sigma_{pads} Q_i y_i}{\Sigma_{pads} Q_i} \tag{3.8}$$

where Q_i is the charge deposited on each pad and y_i is the pad location. Similar to the wire calibration, the y-position can be more precisely measured by using a linearizing technique.

3.6 Step1 and Track Reconstruction

> *Weinberg's first Law: If builders built buildings the way programmers wrote programs, then the first woodpecker that came along would destroy civilization.*

The raw data, saved to tape during the data collection run, is subsequently analyzed and interpreted by STEP1, a program with its major element, QUANAH, being a tree climbing algorithm. In STEP1, the data saved on tape is converted into useful quantities like momenta, positions and times. To complete this, all detectors are calibrated, their pedestals are subtracted and dead or hot channels are corrected for or removed.

The method of track reconstruction and selection is described in more detail elsewhere [45, 56]. First, QUANAH begins by looking for hits in the drift chambers and collecting groups of hits on the 6 planes to create elements.[1] These elements are coupled to clusters on the pads, which provide y position information, and are grouped together as mates. Due to the high multiplicity environment in Au + Au collisions, the four MWPCs were added to the experimental apparatus and act as confirmation detectors between mates of DC2 and DC3. The requirement that at least 3 MWPC wires confirm drift chamber mates 99% efficiently connects correct mates from the two drift chambers [47].

The confirmed hits, are assumed to have come from the target by passing through the magnet. This assumption, along with the determination of the magnetic field, fixes the momentum of each track. However, the assumption that all tracks came from the target is not always defendable as we expect that a fair number of protons and pions result from decays of long-lived hyperons, predominantly Λ's. See Appendix A for more details.

Preliminary tracks are compared to the spatial extent of the collimator and software fiducial cuts are made within the walls of the collimator in order to dispense of spurious tracks. After passing these cuts, they are grouped as track candidates and are filtered such that a maximum number of tracks are selected from an ordered list of track candidates. These tracks are then projected to the TOFU for an associated time-of-flight.

Shown in Figure 3.5 is a typical event measured in the E877 forward spectrometer. The figure displays the DC's, MWPC's, and TOFU hits and

---

[1] Since no two elements can have a single wire hit in common, two-track resolution inefficiencies result, see Section 3.10.

their associated reconstructed tracks. The display reflects a typical number of tracks that pass through the spectrometer, between 5 and 8 on average.

3.7 Time of Flight Calibration

The TOFU and FSCI detectors are described in Chapter 2. They consist of thin horizontal scintillator slats with a photo-multiplier tube on both the top and bottom. Scintillation light reaches each of the phototubes and the time, with respect to BSCI4, and pulse height are registered. If an energy Q is deposited in a scintillator slat of length l at a vertical position y with respect to the vertical center of the slat, the times and pulse heights measured in each tube are given by

$$\begin{aligned} t_{top} &= tof + \frac{l/2 - y}{v_s} \\ t_{bot} &= tof + \frac{l/2 + y}{v_s} \end{aligned}$$

$$\begin{aligned} PH_{top} &\propto Qe^{-\lambda(l/2-y)} \\ PH_{bot} &\propto Qe^{-\lambda(l/2+y)} \end{aligned}$$

where tof is the time-of-flight of the particle to the scintillator, v is the velocity of the signal along the scintillator and λ is its attenuation constant. These position dependencies can be removed by defining the following variables:

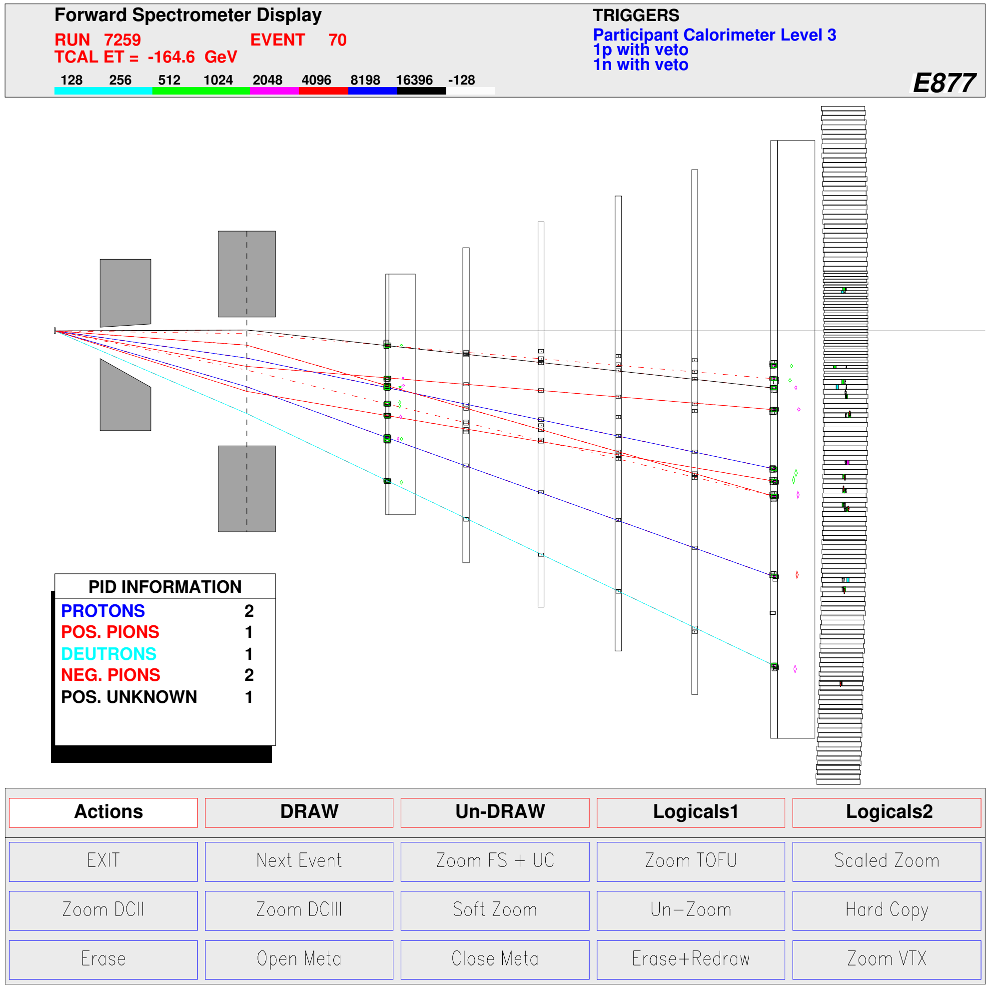

Forward Spectrometer Display

RUN 7259 EVENT 70

TCAL ET = -164.6 GeV

TRIGGERS

Participant Calorimeter Level 3

1p with veto

1n with veto

PID INFORMATION	
PROTONS	2
POS. PIONS	1
DEUTRONS	1
NEG. PIONS	2
POS. UNKNOWN	1

Figure 3.5: Event display for a typical Au+Au collision in the E877 forward spectrometer.

$$\begin{aligned} t_{mean} &= \frac{t_{top} + t_{bot}}{2} = tof + C \\ PH_{mean} &= \sqrt{PH_{top} PH_{bot}} \propto Q \end{aligned}$$

where $C = l/2v$ is a constant.

At the STEP1 level, the variable time offsets measured by TOFU, due to varying cable lengths and run dependent changes in discriminators, are measured and each TOFU slat is calibrated. Therefore, the constant C in the determined t_{mean} is simply absorbed into the overall constant, dubbed t_0. This constant is determined by examining negative tracks in the forward spectrometer which are predominantly pions traveling at near the speed of light. Therefore, the time registered that of the pion is well determined and t_0 is easily measured on a slat-by-slat basis. Since t_0 varies measurably over the course of several days, it is determined for each slat and each run, which corresponds to every few hours, for the entire data set.

The pulse-height spectrum can also be normalized slat-by-slat by requiring that the peak of the pulse-height spectrum for each slat is located at 1.0. This proportionality constant does not change over the course of the data collection set and, therefore, needs to be determined only once.

Finally, the slewing parameters of each TOFU slat are measured. Slewing is a well-known correlation between the pulse height into the discriminator and the measured time. It arises because the time of a pulse is determined by the point at which it passes a fixed threshold. In this case, large signals will pass this threshold sooner than will lower energy signals. To a good approximation, the error in timing resulting from slewing effects is inversely proportional to the pulse height such that

$$\delta t_{slew} = \frac{\alpha}{PH_{top}} + \frac{\beta}{PH_{bot}}. \tag{3.9}$$

α and β are determined for each slat by determining the set that minimizes the width of the TOFU spectrum. Such a determination need only be completed once for the entire data set as the slewing properties do not change significantly over time.

For this analysis, an in depth study of the resulting distribution was performed in order to account for second order effects related to particles of high mass or charge > 1. To this end, a study of the Bethe-Bloch effect and Landau distribution of the TOFU pulse height was completed. A discussion of this method follows.

3.7.1 Bethe-Bloch Formulation

According to the Bethe-Bloch formula, in the framework of a quantum theory, the energy loss in a collision between a traversing particle and a group of atoms depends only upon the velocity and charge of the traversing particle. In E877, this phenomena manifests in the measured pulse heights of the two scintillator detectors (TOFU and FSCI). These dependencies are shown in the left two plots of Fig. 3.6.

Note that the majority of all particles in Fig. 3.6 are charge $= 1$ and $\beta \sim 1$. Two clear tails exist: one from particles which deposit more energy in

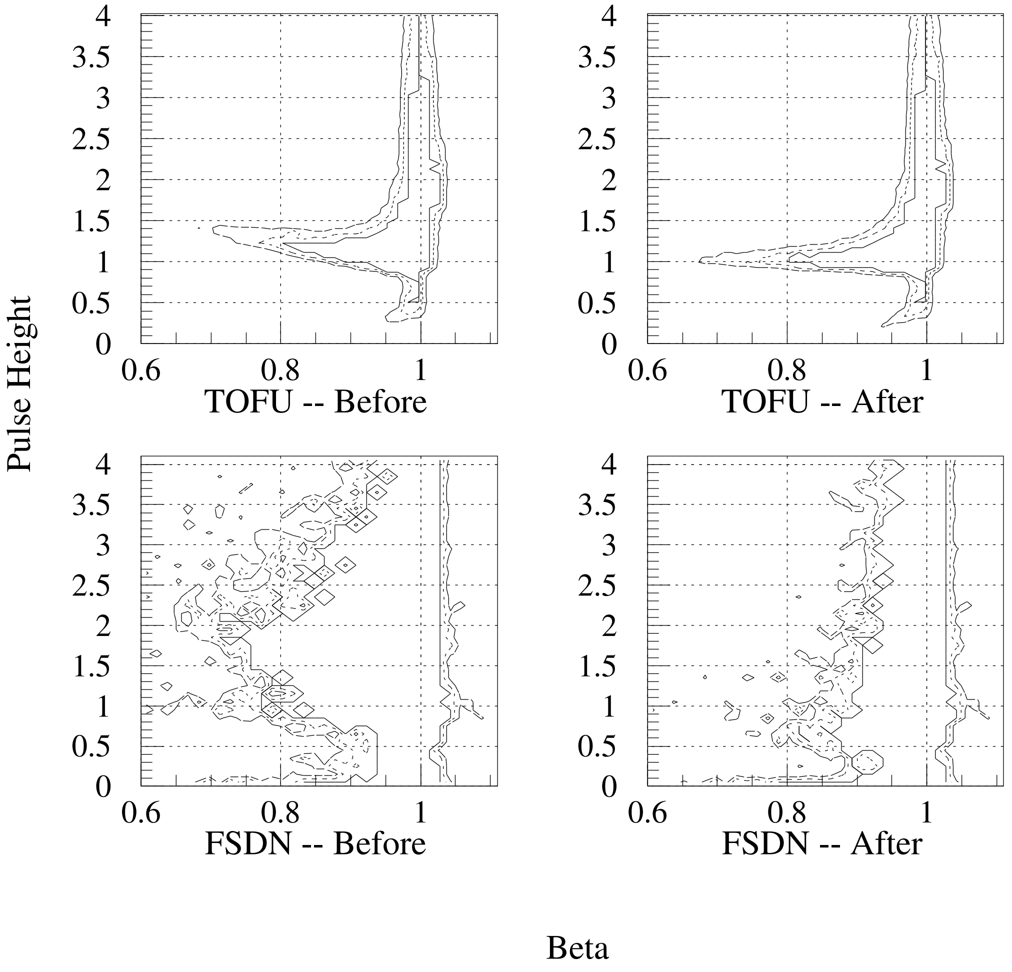

Figure 3.6: TOFU and FSCI pulse height distributions as a function of β before and after the Bethe-Bloch correction.

the TOFU (charge > 1) and the other from low velocity particles. Therefore, to blindly cut on the energy deposition in the TOFU would translate to a β dependent cut efficiency.

The Bethe-Bloch formula gives the energy loss per unit pathlength as [55]

$$\frac{dE}{dx} = \frac{4\pi N e^4}{mc^2\beta^2} z^2 \left(ln \frac{2mc^2\beta^2\gamma^2}{I} - \beta^2 \right) \tag{3.10}$$

which may be simplified to

$$\frac{dE}{dx} = f(\beta) z^2. \tag{3.11}$$

Note that the energy deposited in either of the scintillator slats is simply some unknown function of beta times the square of the charge. Instead of attempting to perfectly model this dependence, if we ignore the exact functional form of dE/dx we can simply parametrize the single charge pulse height as a function of β in the TOFU and the FSCI to find the functional form of $f(\beta)$. Dividing the measured pulse-height distribution by $f(\beta)$ should cause the pulse-height distributions to be simply proportional to z^2 from Eq. 3.11. This normalized distribution, shown in the right two plots of Fig. 3.6, allows for momentum and specie independent cuts on the pulse height distribution.

3.7.2 Landau Distribution

Shown in Fig. 3.7 is the measured pulse height distribution in TOFU. Three peaks are evident in the distribution corresponding to charge = 1, two charge = 1, and charge = 2 particles. While the peaks are distinguishable, the widths of the distributions are wide enough to smear into one another. In the particle identification routine, however, we would like to make strict cuts on charge = 1 and charge = 2 particles. In this section we will outline a technique of fitting the spectra shape of the pulse height distribution in order to understand the efficiency of cuts in this space.

The energy spectrum of particles traversing a scintillator is determined by the Landau distribution [55] given by

$$f(x,\delta) = \phi(\lambda)/\xi, \tag{3.12}$$

where

$$\phi(\lambda) = \frac{1}{\pi}\int_0^\infty exp(-uln(u) - u\lambda)sin(\pi u)du \tag{3.13}$$

$$\lambda = \frac{1}{\xi}(\Delta - \xi(ln\xi - ln\epsilon + 1 - C)) \tag{3.14}$$

$$ln\epsilon = ln\left(\frac{(1-\beta^2)I^2}{2mc^2\beta^2}\right) + \beta^2 \tag{3.15}$$

$$\xi = B/\beta^2 \tag{3.16}$$

with $C = 0.577$ (Euler's constant) and B a function of the scintillating material. The CERN standard libraries provide the functional form of a Landau distribution in their common code (see the functions *dislan* and *denlan*). Through these libraries, we can fit the TOFU pulse height distribution to three

Landau functions, corresponding to charge = 1; two charge = 1; and charge = 2. The results of the fit are shown in Fig. 3.7.

Notice that the fit describes the distribution well at low pulse-heights but begins to deviate slightly at higher pulse-heights. Also notice that the deposited energy peaks are decidedly non-linear since, from the Bethe-Bloch parameterization above we would expect that the charge = 2 peak would be located a four times the charge = 1 peak. This is a well-known attribute of this detector due to the fact that the high-voltages on the photo-multiplier tubes were run high in order to increase the gain. Therefore, the deviation of the fit at large pulse-heights may simply be due to the non-linearity of the TOFU pulse-height response.

A second iteration at fitting the pulse-height distribution in TOFU included an attempt at parametrizing the non-linearity of this detector's response. In order to perform this function we compared the TOFU pulse-height distribution to that of the FSCI, since the FSCI does not suffer from the same non-linear deficiencies. For example, shown in Fig. 3.8 is a plot of FSCI pulse-height vs TOFU pulse-height clearly showing the non-linearity of TOFU with respect to FSCI. Clear peaks for charge = 1, two charge = 1, charge = 2 and charge = 3 are apparent. The FSCI peaks occur at the correct points (1, 2, 4, and 9 respectively) while the TOFU peaks occur at 1, 1.6, 2.5, and 3.6.

As a first order approximation this measured distribution can be used to parametrize the non-linearity of TOFU. We use the assumed non-linear curve of

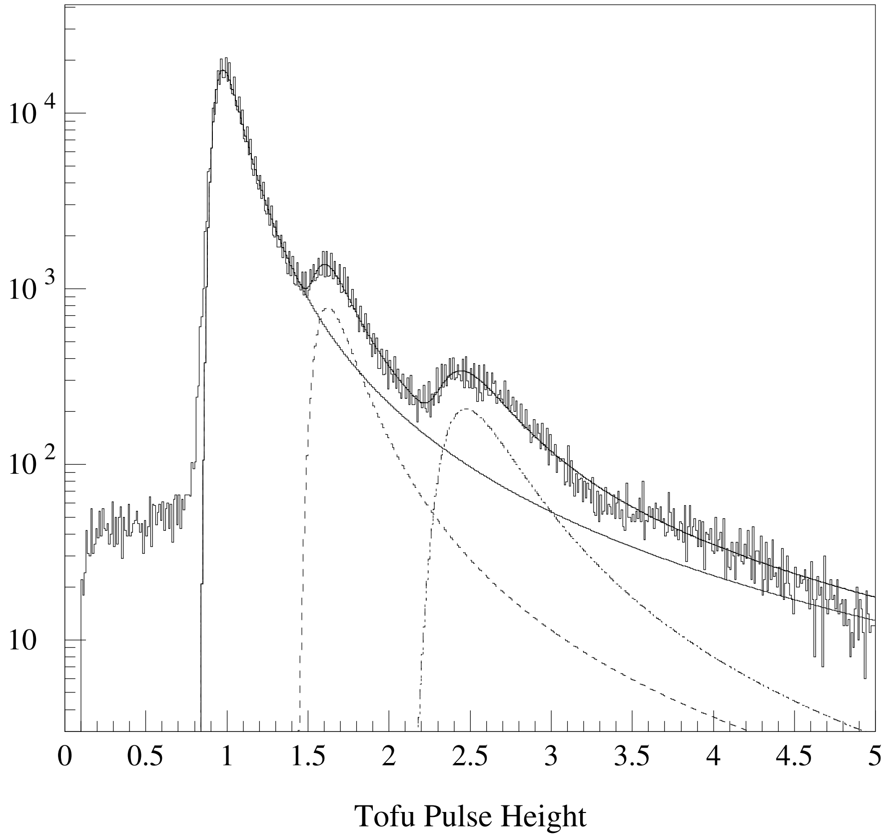

Figure 3.7: TOFU measured pulse-height and the fit to 3 Landau distributions corresponding to charge 1, two charge 1, and charge 2.

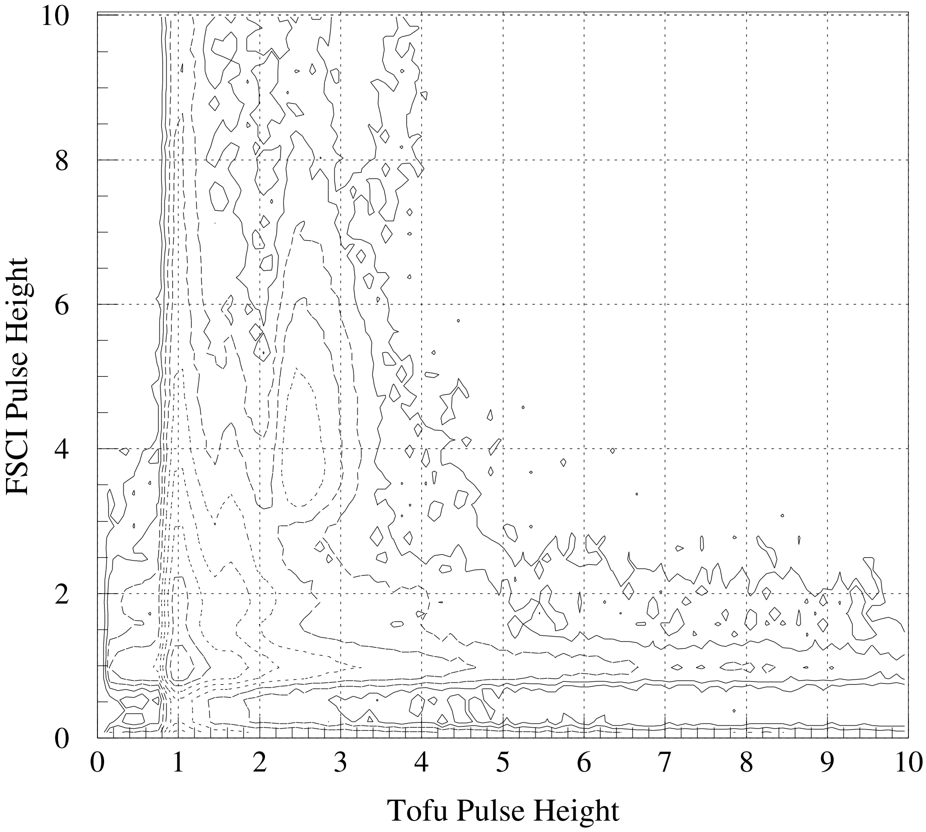

Figure 3.8: FSCI vs TOFU pulse-heights showing the clear nonlinearity of the TOFU.

$$(P.H.)' = A * (1 - e^{-(P.H.)/B}) \tag{3.17}$$

where $P.H.$ is the theoretical peak of the pulse height of that charge and $(P.H.)'$ is the measured peak value. The values of $A = 472 \pm 10$ and $B = 476 \pm 15$ describe the distribution relatively well and this non-linear function is used to re-fit the TOFU distribution to 3 Landaus, shown in Fig. 3.9. Note that the non-linear response appears to fit the distribution better around the charge $= 2$, $(P.H.)' = 2.5$ peak though it does not describe the distribution above $(P.H.)' = 3.5$; this section of large energy deposit may be due to higher charge particles, as can be seen from Fig. 3.8

Finally, these fits are used to deduce the efficiency of our cuts in the TOFU. For this analysis, we take the linear fit and non-linear fit to be indicative of the approximate error in our knowledge of the TOFU efficiencies. For example, the "standard" E877 TOFU pulse-height cut is from 0.7 to 1.4; the linear fit concludes that this cut rejects 12.5% of the signal whereas the non-linear fit predicts a 9.23% rejection rate. The relative uncertainty in these values, as given by these two methods, will act as an uncertainty in the overall yield of charged particles. In general, charge = 2 cuts will be less well known and will, therefore, have larger uncertainties. The cut inefficiencies evaluated via this method are displayed in Table 3.2.

3.8 Particle Identification

> *Some people are afraid of heights. Not me, I'm afraid of widths.*
> [Steven Wright]

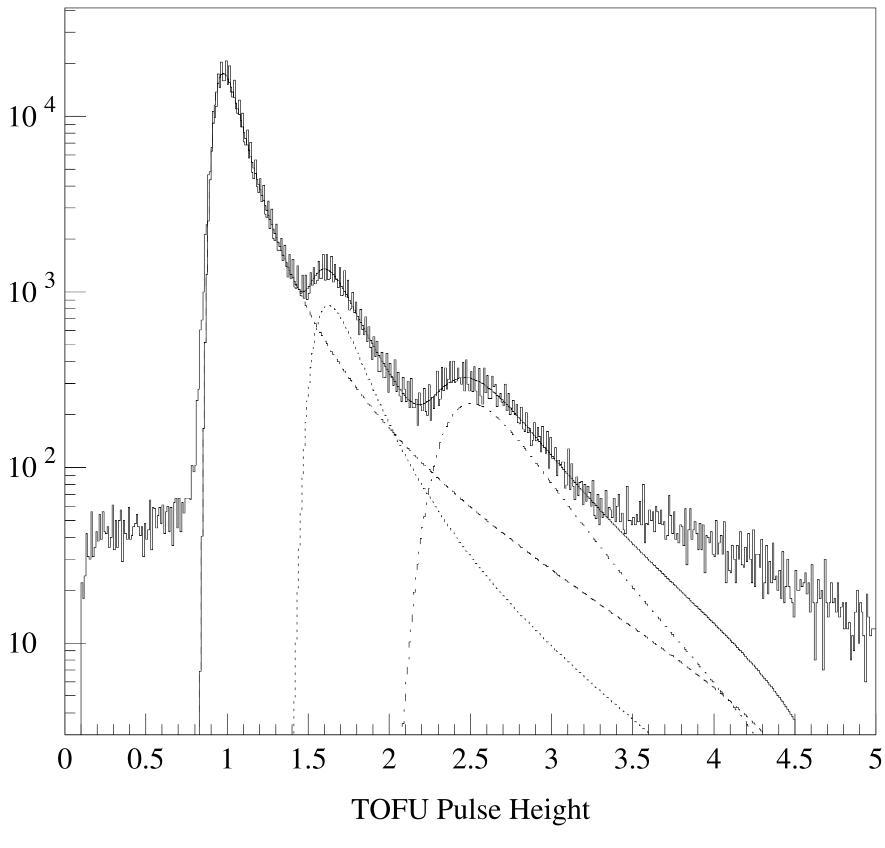

Figure 3.9: The TOFU pulse-height distribution fit to 3 non-linear Landau functions as described in the text.

Charge	Lower Pulse Height Cut	Upper Pulse Height Cut	Percentage of Signal Kept	
			Linear	Non-linear
1	0.7	1.3	83.5	86.6
	0.7	1.4	87.5	90.8
	0.7	1.5	90.0	93.2
	0.7	1.6	91.6	94.9
	0.7	1.7	92.9	96.0
	0.7	1.8	93.8	96.8
2	2.2	3.0	72.6	79.6
	2.2	3.1	76.4	84.1
	2.2	3.2	79.4	87.6
	2.2	3.3	81.8	90.2
	2.2	3.4	83.7	92.2
	2.2	3.5	85.3	93.8

Table 3.2: TOFU cut efficiencies on charge = 1 and charge = 2 particles.

The particle identification routine for protons, pions, and kaons in the 1994 data set is described in detail elsewhere [56] and is identical to that performed in the 1993 run [47]. Determination of the identification of any particular track requires knowledge of its momentum and time of flight. Time of flight was measured by the TOFU; momentum, by the drift chambers. Assuming the target was the origin of all tracks, the rigidity of any track can be determined from the radius of curvature of the track (R) through the magnet and the value of the magnetic field B:

$$\frac{rigidity}{e}\frac{\sqrt{px^2+pz^2}}{Ze} = RB \qquad (3.18)$$

where Ze is the charge of the particle. [2] The final momentum component, p_y, is calculated from measurements of the vertical position of the track at the

---

[2] At the STEP1 level, we assume that all particles are $Z = 1$; in the event of an

TOFU. The reconstructed mass of each track is given by

$$m^2 = \frac{p^2}{\beta^2\gamma^2} \tag{3.19}$$

where β and γ are calculated from the time of flight measurement coupled with the known distance to the TOFU slat.

Shown in Figure 3.10 is a plot of momentum versus reconstructed mass squared with this method. The momenta of all particles is multiplied by the charge in the plot so that negative particles are displayed below the axis and separate from the positive tracks. Note that the mass squared distributions for pions, kaons, protons and deuterons are clearly discernible though all of their mass peaks broaden at high momentum. These effects are due to the time of flight/momentum resolution and multiple scattering. Also note that there are a large number of tracks that have a negative m^2 value. These points correspond to particles with velocities close to the speed of light. At this point, the time resolution of the TOFU (85 ps) smears some particle's measured velocity above the speed of light. If we were to simply plot m as opposed to m^2, these points, which correspond to real tracks, would be lost in the presentation.

An analytical description of these mass peaks and widths has been attempted by previous analyses in E877 for both the '93 and '94 data sets [47, 56] and are based upon an analysis by [59]. The analysis assumes a constant time of flight resolution and a variable momentum resolution that can be decom-

---

individual analysis which measures $Z = 2$ the momenta must all be multiplied by 2.

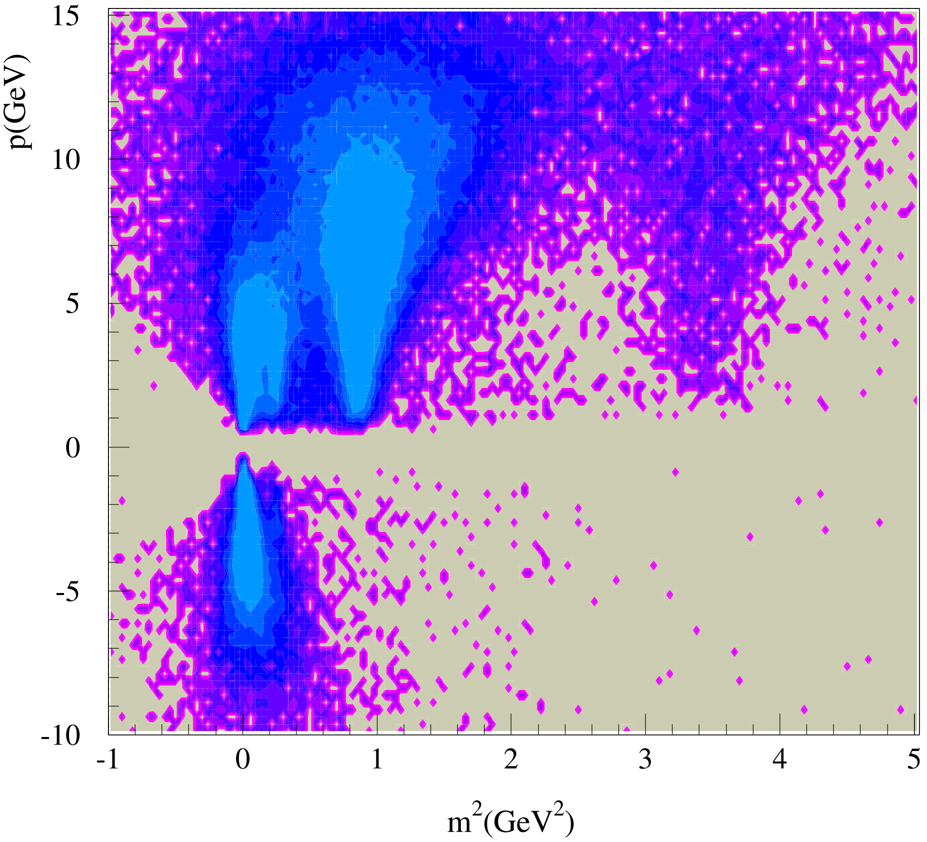

Figure 3.10: Momentum vs mass^2 for all particles.

posed into independent multiple scattering and angular resolution terms

$$\sigma_p{}^2 = \sigma_{p(ang)}{}^2 + \sigma_{p(M.S.)}{}^2 \tag{3.20}$$

where $\sigma_{p(ang)} = c_1 p^2$ and $\sigma_{p(M.S.)} = c_2 p/\beta$. Since the mass resolution is determined by the time of flight and momentum resolutions

$$\sigma^2_{m^2} = 4m_0^4(\frac{\sigma_p}{p})^2 + \frac{4p^4}{\beta^2}(\frac{\sigma_{TOF}}{t_{v=c}})^2. \tag{3.21}$$

where $t_{v=c}$ is the time for a v=c particle to reach the TOFU slat, such that

$$\sigma^2_{m^2} = c_1^2(4m_0^4 p^2) + c_2^2(4m_0^4(1+\frac{m_0^2}{p^2})) + c_3^2(4p^2(m_0^2+p^2)) \tag{3.22}$$

where c_1, c_2, and c_3 are constants representing the angular, multiple scattering and time of flight resolutions respectively.

These three coefficients are determined by fitting the mass^2 distributions as a function of momentum for the pions, kaons, protons and deuterons to a Gaussian. Then, the mean and sigma of the Gaussian fits were fit to the functional form of Eq. 3.22. The mean for each specie was found to be constant as a function of momentum, indicating that the spectrometer is correctly aligned, and within 2% of their nominal value [56]. Shown in Fig. 3.11 are the resulting $\sigma_m{}^2$ of the pion, kaon, proton and kaon fits. The theoretical distribution of the width of the peaks is also displayed and describes the data well.

The fitted values of c_1, c_2, and c_3 are expected to be constant for all particle specie. In fact, as is shown in Table 3.3, we find that they are slightly

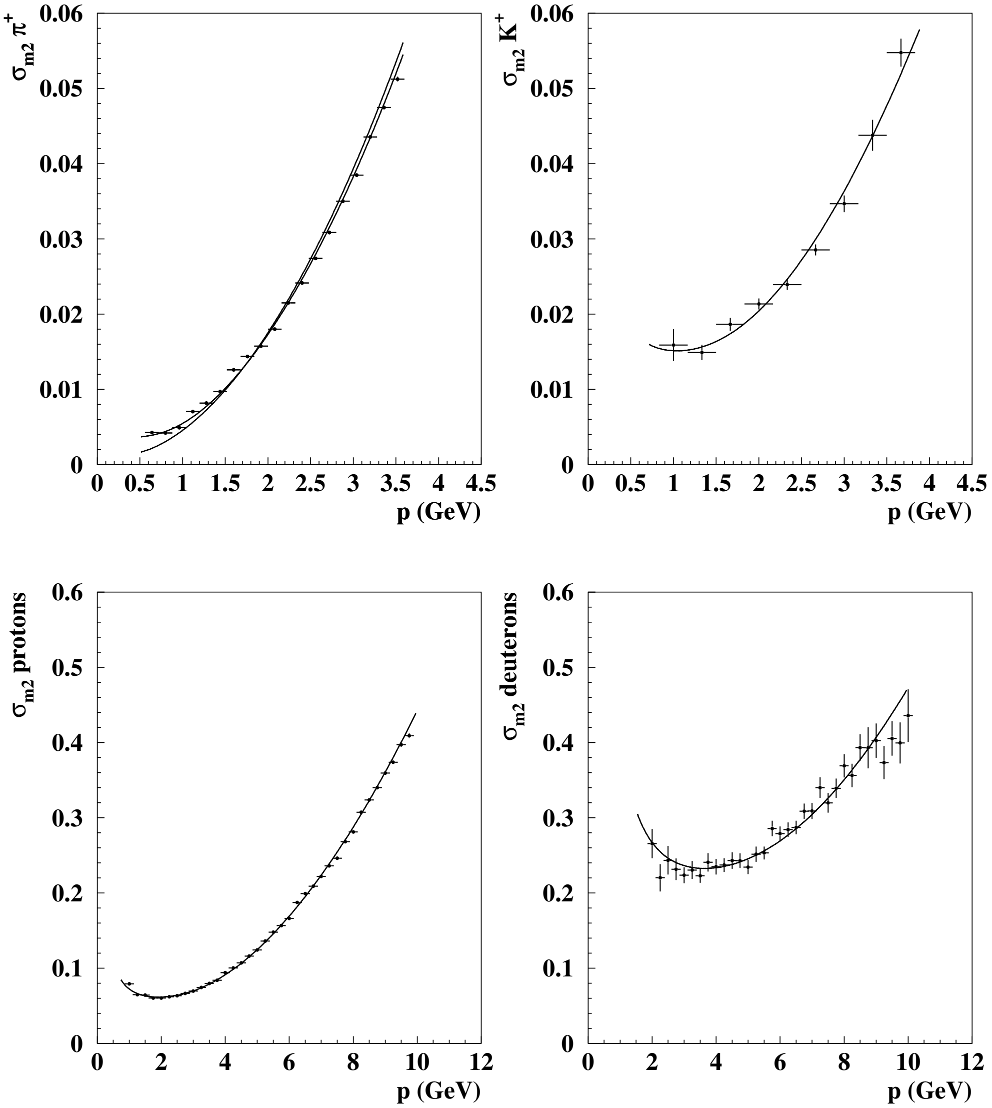

Figure 3.11: The width of the fits of the mass squared distributions for π^+,K$^+$, protons and deuterons to Equation (3.22) as a function of momentum. The two curves for pions are determined using first a free fit to the just the pion spectra, which produces the lower curve at low p_t, and the average value of c_2 from the other particle species. The figure is taken from [56] and represents the standard offline definition of particle identification for E877.

particle	c_1 $((GeV/c)^{-1})$	c_2	c_3	$\sigma_{tof}(ps)$
π^+	0.0024	0.0289	0.002181	90
K$^+$	0.0024	0.0277	0.001846	76
proton	0.0024	0.0298	0.002177	90
deuteron	0.0024	0.0273	0.001945	80

Table 3.3: The values of the fit constants for particle identification. The fit was performed by requiring that the values are consistent with one another as described in the text. The time of flight resolution, σ_{tof}, was computed assuming a constant path length of 41.12 ns for a $v = c$ particle.

different. Note that the kaon and deuteron fitted values are similar yet different from the pion and proton distributions. This systematic is probably due to the fact that the fitted mass^2 plots for deuterons and kaons incorporated an estimate of the background from protons and pions, respectively, which may have biased the fits. For this reason, kaons and deuterons, whenever they are measured by E877 are always accompanied by a systematic study of this background (see Section 3.9 and [56]).

However, in the standard preliminary identification of particles, each point in $p - mass^2$ space is assigned an identification corresponding to this theoretically guided fit. Any point in this space is assigned a particle identification if its mass^2 is within 1.5σ of a particle species' band and 2.5σ distanced from significant peaks to either side in mass^2. E.g., π^+ are identified as those within 1.5σ of the π^+ mean but at least 2.5σ distanced from the K^+ band. Shown in Figure 3.12 is the identified bands for all pions, kaons, protons and deuterons.

In Figure 3.13 is the acceptance in p_t and y for all particles identified via this method. The acceptance is simply the distribution in momentum-space

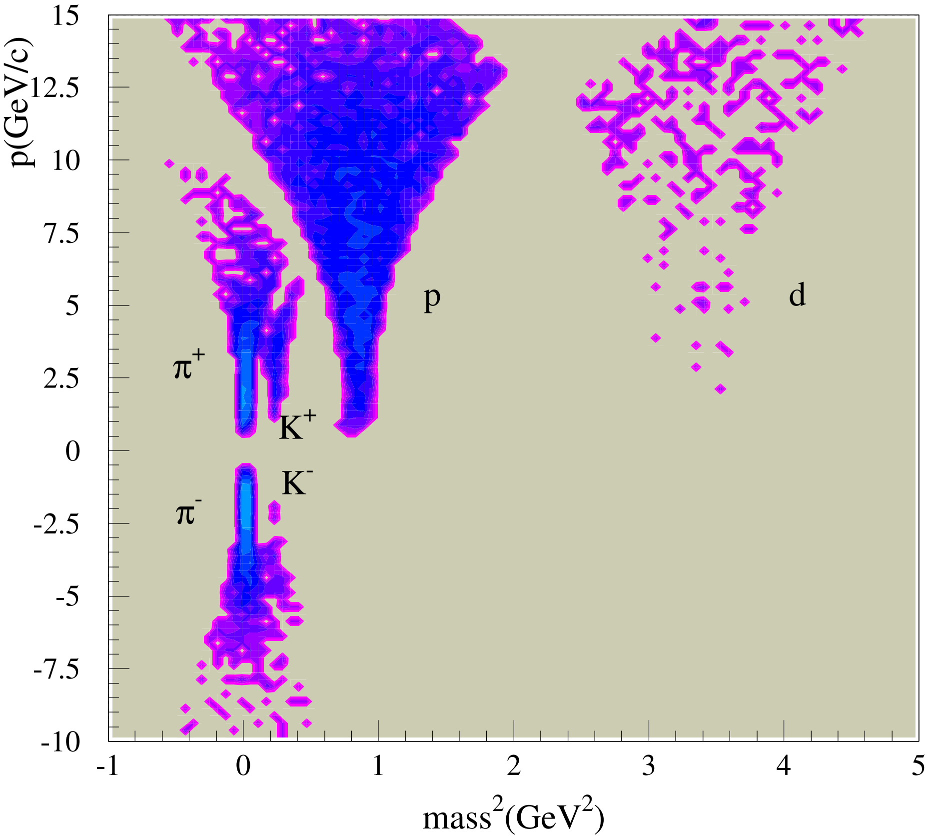

Figure 3.12: Momentum vs mass^2 for all identified particles.

of particle trajectories that could pass through our spectrometer. Figure 3.13 is generated from the distribution of the reconstructed momenta of particles in the forward spectrometer. The right side edge of each plot is due to the maximum momentum restriction of each particle specie; the left hand edge is due to the spectrometer edge and the cut at low p_t is due to the deadened region in the drift chambers through which the beam passes. This deadened region causes a band of unidentifiable particles in the π^- spectrum; by changing the polarity of the magnetic field, the band is recovered in the π^- and present in the spectra of the positive particles. Of particular note is the fact that heavier particles are measured at rapidities much lower than beam; protons are detected at low transverse momentum past mid-rapidity ($y = 1.6$, beam is at $y = 3.2$) and deuterons are measured down to $y = 1.0$. This added acceptance at mid-rapidity will aid in comparisons to other experiments, the majority of which measure light fragments at mid-rapidity.

3.9 Gleaning Light Fragments from the Data

As has been demonstrated in the previous section, the extraction of identified particles from the reconstructed momentum and mass is non-trivial even for abundant particles. For light fragments we will find that this difficulty is compounded by the fact that the background can often be as large as the signal and can vary across the reconstructed mass^2 peak. In order to construct the invariant cross-section of a particular particle specie, the yield of this specie in each region of phase space must be determined. This yield is then corrected

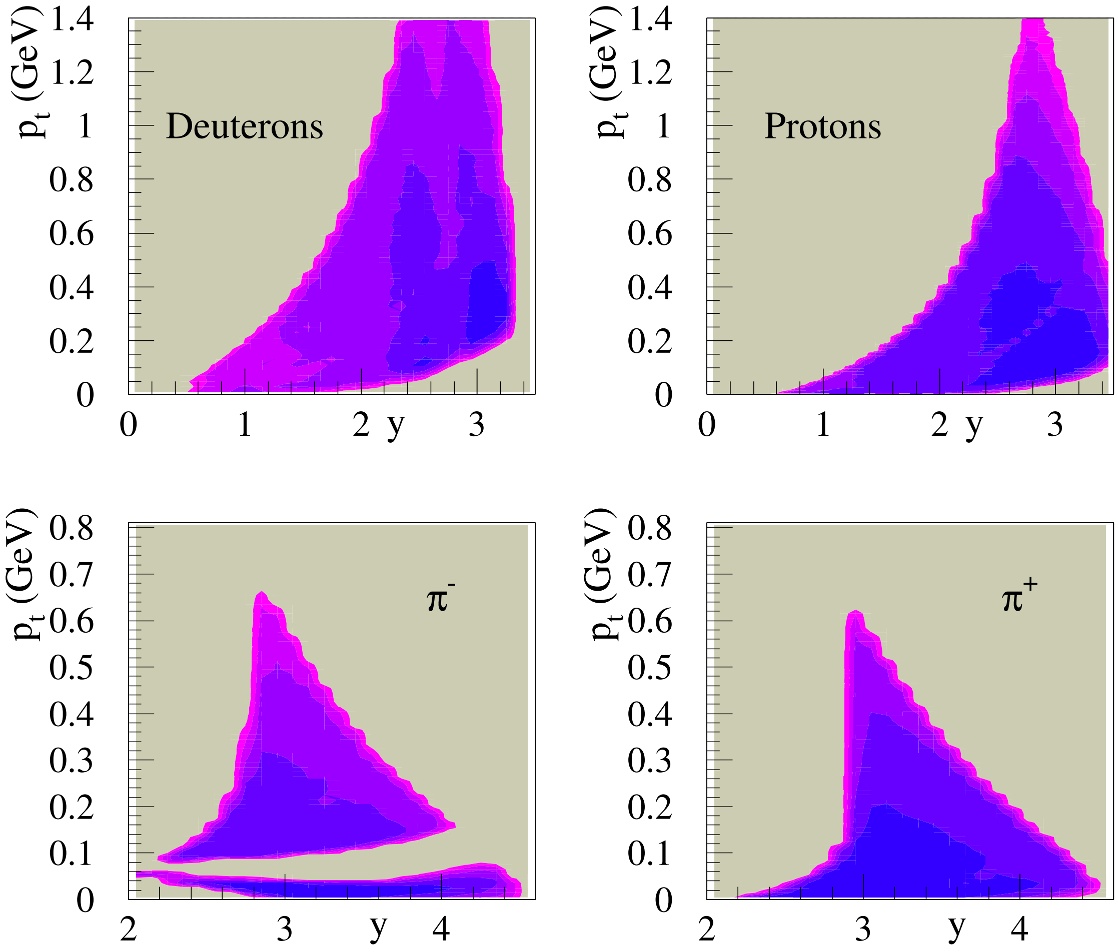

Figure 3.13: Acceptance for various species in the E877 spectrometer as a function of p_t and y.

for the known experimental efficiencies of the apparatus. In Section 3.10 these efficiencies will be discussed. In the current section the methods for gleaning these light fragments from the data as a function of p_t and y will be discussed in detail.

3.9.1 Deuterons

The deuteron reconstructed mass^2 distribution is complicated by the fact that the proton peak is nearby and therefore, at momenta above 10 GeV/c, significantly contaminates the deuteron distribution. In order to reduce these effects, a systematic and thorough background subtraction technique was developed. Shown in Figure 3.14 is the reconstructed mass^2 in several regions of phase space, divided into p_t and y bins. These four regions are representative of the reconstructed mass^2 spectrum in all measured regions. At low momentum, the upper-left most plot, the deuteron and proton peaks are clearly distinguishable along with an exponential tail from the proton distribution, most likely corresponding to resonance decays into protons (such as the Λ). [3] In this region of phase space, the mass^2 distribution is fit to two Gaussians and an exponential background. At higher momenta, the proton and

---

[3] Long lived resonances, especially Λ's, which decay in the spectrometer will not be reconstructed correctly by our tracking algorithm, which assumes the target as a point on the trajectory. Therefore, though the Λ's will be reconstructed near the proton peak, since the determination of their momenta and time of flight is unsound, the Λ peak will be much more broad than the proton.

deuteron mass^2 distributions broaden, due to the momentum resolution of the apparatus, and the exponential background drops to negligible. In this region of phase-space, shown in the upper right portion of the figure, the mass^2 distribution is easily fit to two Gaussians. The third region (the lower left plot in Figure 3.14) conspires in such a way that the deuteron distribution is not distinguishable from the proton distribution. At this point, the momentum resolution smearing coupled with the approximately equal particle yields for protons and deuterons, causes the peaks to overlap and become indistinguishable. Therefore, E877 cannot discriminate deuterons from protons in this region. However, at beam rapidity calculated assuming the deuteron mass, the contamination of protons is minimal because the proton would need to be traveling at twice beam momentum, an impossibility for our collisions. Thus, a deuteron peak is again visible (lower right portion of Figure 3.14) and the yield can be determined by fitting this region to a single Gaussian.

The yield of deuterons in each bin of phase space can be determined by fitting the mass^2 space to a multi-parameter function which always includes a Gaussian fit to the deuteron peak. This results in a deuteron yield for each bin (N_d) determined by

$$N_d = \sigma_d A_d \sqrt{2\pi} \tag{3.23}$$

where σ_d and A_d are the sigma and amplitude of the Gaussian fit to the deuteron peak. Those regions of phase space that fall between a clear two peaks with a background and simply two peaks without any background, the

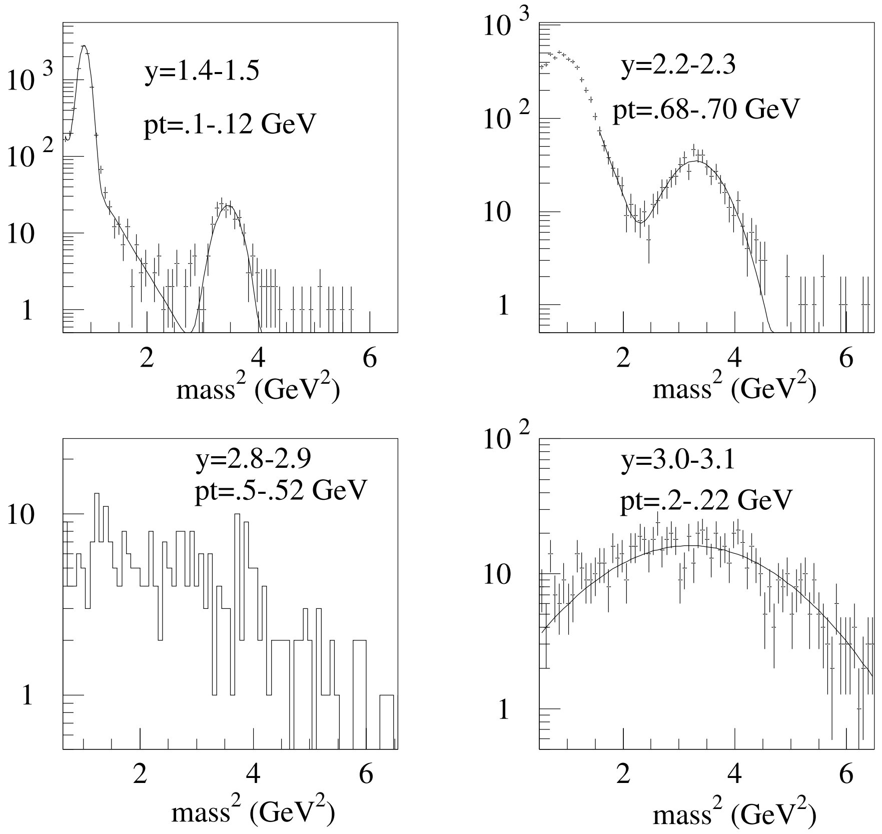

Figure 3.14: Multi-parameter fits to the deuteron mass^2 distribution. See the text for details.

upper left and right plots in Figure 3.14, respectively, have been fit to both functions in order to determine the systematics of the fitting choice. The resulting yield of deuterons is similar from both fits to within 5%.

3.9.2 Tritons

Beyond the problem of the 1-2 orders of magnitude difference between the triton and deuteron yield, the triton signal is further complicated by the fact that its mass^2 distribution is also wider than the deuteron's. However, a technique similar to that used for the deuterons can also be utilized to measure the yield of tritons in our collisions. In Fig. 3.15 is the reconstructed mass^2 distribution in various y bins for $p_t < 0.5$ GeV/c. A clear triton peak is visible couched next to the deuteron peak. The yield of tritons can be calculated for each region of phase space by fitting this distribution to a Gaussian centered at the mass of the triton with an exponential background, coming from the deuteron tail, underneath; several examples of these fits are shown in Fig. 3.15. Then, exactly as in the deuteron yield calculations, the yield is given by the integral under the Gaussian, or $\sigma_t A_t \sqrt{2\pi}$.

3.9.3 Helium

Similar to extracting the triton signal, the ^3He signal is found by first recalculating the mass^2 assuming now that all particles are charge = 2, instead of charge = 1 as is assumed in the standard STEP1 (see Section 3.6). This will cause all charge = 1 particles to be plotted at double the actual mass such

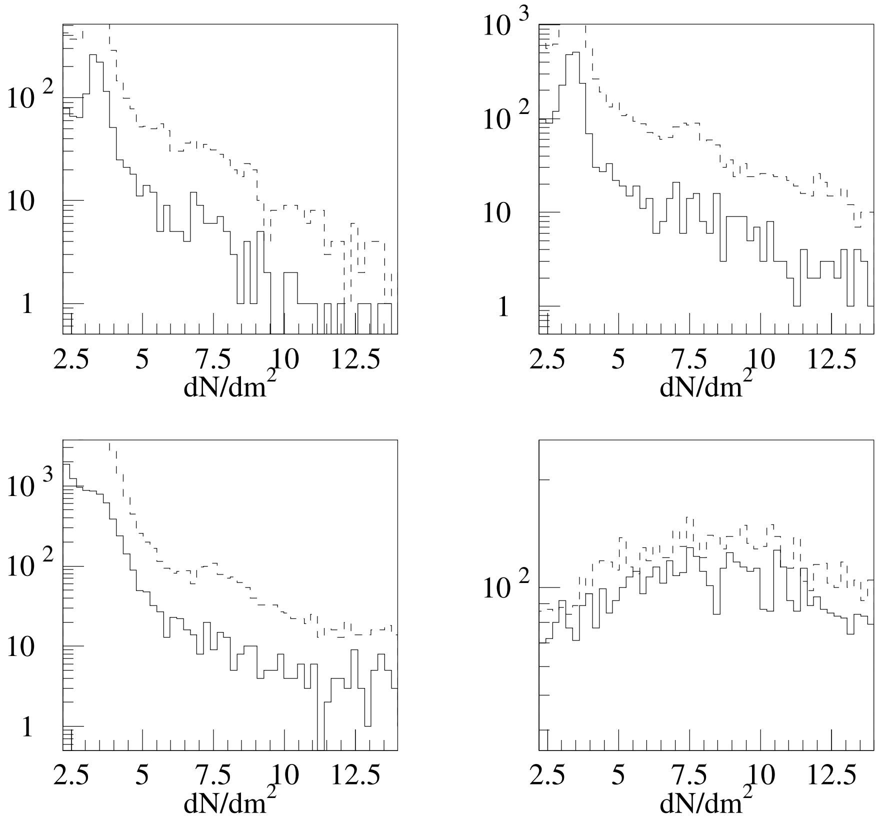

Figure 3.15: Mass^2 peaks for various rapidities assuming the triton mass. A clear peak is seen at the triton mass. This peak, though coupled with a large systematic error due to the small signal-to-background ratio is fit to a Gaussian at the mass of the triton plus an exponential background from the deuteron peak.

that the ^3He peak is found between the proton and deuteron peak, as shown in Fig. 3.16. For this distribution, we first cut on the energy deposited in the TOFU, requiring it to be between 2.2 and 3.5, in order to cut on charge = 2 particles; see Section 3.7 for details. The ^3He peak, located at $mass^2 \sim 9$ GeV^2, is clearly differentiated from the protons and deuterons at mid-rapidity, located at $mass^2 \sim 4$ GeV^2 and $mass^2 \sim 16$ GeV^2, respectively. However, the peak is is lost under the proton peak above $y \sim 2.0$. The yield of ^3He in each bin may be extracted by fitting the mass^2 distribution to a Gaussian at the mass of ^3He and an exponential tail from the proton peak.

^{4}He is inextractable from our experimental measurements at any point in phase-space away from beam-rapidity due to the low yield of ^{4}He produced in heavy ion collisions and passing through our spectrometer, as is described in Appendix B. However, at beam rapidity we do measure ^{4}He. Due to the fact that we measure the momentum/charge with our spectrometer, ^{4}He particles plotted in momentum vs mass^2 assuming charge = 1 are located underneath the deuteron signal. To extract the ^{4}He signal from data, a separate method must be formulated than those outlined above. First, we cut on the ^{4}He peak in momentum vs mass^2 utilizing the function for the peak width as a function of momentum determined in Section 3.8. The TOFU pulse height distribution within these particle identification cuts has two peaks, corresponding to charge = 1 and two charge = 1 particles, at all but beam rapidity where an additional charge = 2 peak arises. These peaks are fit, in several bins of p_t and y to both the linear and non-linear Landau distributions, as described in Section 3.7, and the yield is then determined from the integral under the fit to the charge

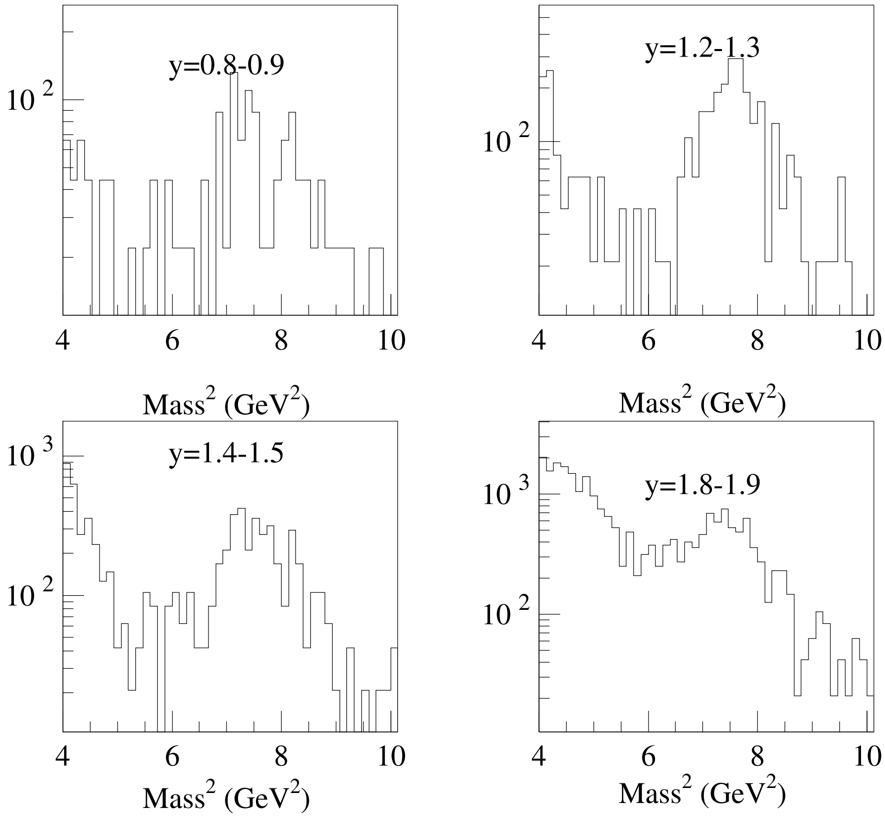

Figure 3.16: Mass^2 peaks for various rapidities assuming the ^3He mass and $p_t < .5$ GeV/c. A clear peak is seen at the ^3He mass which is lost under the proton tail for rapidities above $y \sim 2.0$.

= 2 distribution. An example of this fit is shown in Fig. 3.17

3.10 Experimental Efficiencies

Our experimental measurements of particle yields have associated inefficiencies related to the reconstruction of tracks. Therefore, in order to reconstruct yields of particle specie as a function of p_t and y, these efficiencies must be studied and corrected. Since a variety of cuts are performed on the data, explicitly and implicitly, and acceptance and reconstruction efficiencies can decrease the number of measured tracks, the yield of particles as a function of rapidity and p_t in our collisions must account for these inefficiencies.

As the spectra presented in this thesis are normalized to the number of collisions, any cut in our analysis which decreases the number of collisions without biasing the sample will not affect the data; this includes all cuts on SILI, BVER and BSCI as well as the calorimeters, all of which determine either a good beam particle or event class. Therefore, these cuts, described in Sections 3.2 and 3.6, do not bias our total yields.

However, there are various cuts which do affect the yield of measured particles in our apparatus. Among them are:

- TOFU pulse height cuts.
- PID cut efficiency.
- DRCH/MWPC track reconstruction efficiencies.

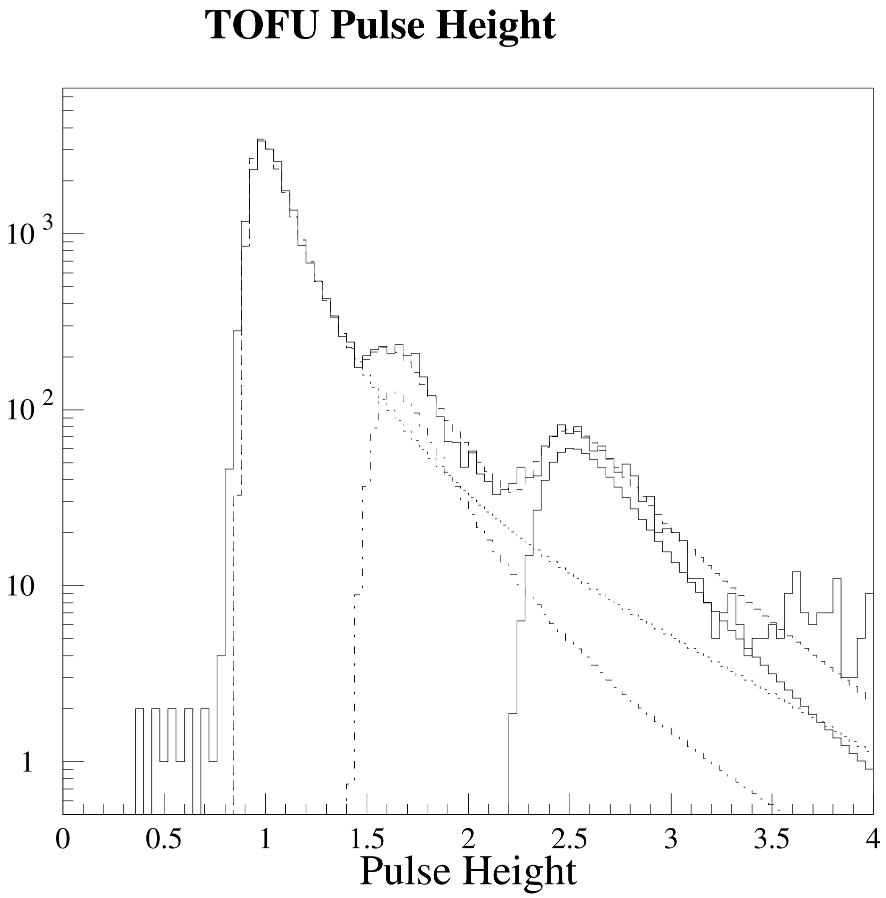

Figure 3.17: A fit to the TOFU pulse height distribution for all particles at beam rapidity and from 0.5 to 1.0 GeV/c in p_t.

- Drift chamber occupancy inefficiencies.
- Acceptance cuts.

The first two items are independent of momentum: the TOFU pulse height cut is a one time correction, described in Section 3.7 and particle identification cuts are well determined from the momentum dependent standard 1.5σ cut described in Section 3.8. In this case, implemented for proton and pion spectra, we determine the amplitude and width of the Gaussian m^2 distribution and thus the total integral is determined. However, in the light fragment analysis, the standard PID routine is not implemented and the total yield of fragments is simply determined from multi-parameter fits described above. In this case no effective particle identification inefficiencies exist as they do in the standard particle identification routine. Finally, the track reconstruction inefficiencies have been studied for this apparatus by [47] and found to be better than 99% in reconstructing tracks passing through the forward spectrometer. This high efficiency results from the pattern recognition code, described above. As such, the first three items on the above list effectively boil down to the momentum independent TOFU pulse-height cut.

However, the last two items in the list, concerning occupancy and acceptance, do have dependencies on the momentum of the particle and involve more complicated effects. These have been modeled [45, 47] with two simple routines, descriptions of which are given below.

3.10.1 Drift Chamber Occupancy

Should two tracks traverse similar paths through the spectrometer such that they pass through the same cells in DC2 and/or DC3, either one or both of the tracks may not be reconstructed by QUANAH. In order to compensate for this effect, the raw hits in the drift chamber are used to estimate the reconstruction inefficiencies and correct for them [47].

From the measured data the primary track density in each of the two drift chambers is determined, which translates to a determined probability of each wire firing. This distribution is shown in Fig. 3.18. Additionally, the probability of independently reconstructing two close tracks is determined [47]. These two parameters can be used to determine the probability of track reconstruction as a function of the position in each chamber. These probabilities, along with their correlation are sufficient to determine the overall reconstruction as a function of p_t and y.

This model, with some variations, has been successfully used to correct for inefficiencies in tracking due to two overlying tracks and, compared to GEANT simulations and an independent analysis, shown to provide consistent results [47]. From this analysis, it was found that the efficiency for reconstructing tracks in our spectrometer varies from 62% to 87% across the drift chamber face due to close-lying tracks. Therefore, as a function of position in the drift chamber, which is equivalent to the momentum of the particle, our data are corrected by this calculated efficiency.

It should be noted that, due to their intrinsic cell size, DC3's efficiency for

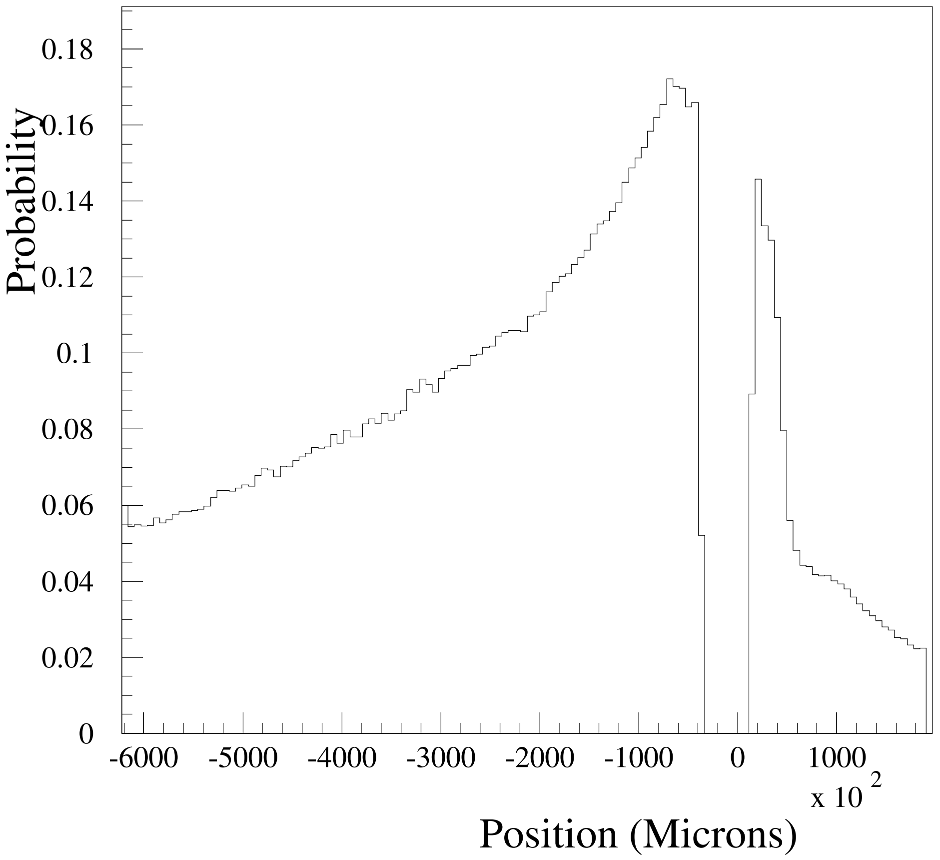

Figure 3.18: The probability of a wire firing in DC2. Notice the region at position = 0, corresponding to the deadened region of the drift chambers, through which the beam passes.

reconstructing neighboring tracks drops off at 2cm, DC2's, at 1cm. Since the TOFU is located directly behind DC3 and has a scintillator slat spacing of 1cm, the occupancy correction for DC3 automatically accounts for any tracks which strike the same TOFU slat. Therefore, no additional correction is needed to account for the TOFU occupancy.

3.10.2 Acceptance

Finalized spectra are presented in various p_t and y bins and, thus, the *absolute* yield of each particle specie is required. However, our apparatus accepts only a small fraction of the entire Au-Au collision and so we must, with software models, correct for these cuts made by our experiment. A simplified model for such a calculation of the acceptance of our apparatus was devised [45] for the '92 data set and was extensively modified [47] for the '93 data set. This model, described below, was used in this and other theses for the '94 data set [56].

Instead of performing a full-blown GEANT simulation in order to model our experimental response, a simple model which mimics the GEANT simulations, was developed. The user inputs the measured beam position and angle into the program as well as the expected rapidity and transverse momentum spectra. Then, the Monte Carlo program passes this distribution through the apparatus, one track at a time, and determines if it passes through the acceptance of the forward spectrometer. In order to minimize those effects due to edges of detectors or the collimator, fiducial cuts were made on both the measured and Monte Carlo tracks. Also, any simulated or real tracks which hit a dead or sporadic TOFU slat were removed. Therefore, the probability of a particle with a particular p_t and y passing through our detector and being reconstructed can be calculated and used to correct the raw yields found in Section 3.9.

As a final caveat, when the acceptance does not vary significantly over a single bin, the exact formulation of the input momentum distribution is insignificant. However, at the edges of the acceptance these variation can be significant and so the acceptance program is implemented iteratively on the spectra, using the corrected output as input, until there is no change in the resultant spectra over iterations.

3.10.3 Summary

Thus, for each bin of the phase-space area $p_t dp_t dy$ the number of collision ejectiles per event is determined. This total is corrected for experimental efficiencies,presented and analyzed as a function of p_t and y in the subsequent chapter.

Chapter 4

Measurements of Light Fragments

Light fragments from heavy ion collisions are essentially dual natured. They can be interpreted in a model which accounts for their single particle nature, in which case the transverse spectra are compared to those of other single particle specie. Alternatively, light fragments can be interpreted as a correlation function via the coalescence parameter B_A which characterizes the volume and flow parameters of the source. Additionally, E877 has the ability to measure beam-rapidity light fragments, a unique measurement at AGS energies. The beam-rapidity region is governed by different processes than non-beam regions and may provide insight into the fragmentation of nuclear matter and the liquid-gas phase transition.

In this chapter we will approach each of these methods. In Section 4.1 light fragment invariant spectra will be measured and discussed in light of a thermal model; comparisons of fragments to lighter specie will aid in this interpretation. Subsequently, in Section 4.3, an excitation function of the coalescence parameter for A = 2 and A = 3 light fragments will be shown and comparisons to other correlation functions will be made. Comparisons to previous and current measurements of the coalescence parameter will favor viewing Au + Au light fragment production as indicating an increased freeze-out volume as compared to Si + Pb and Si + Al collisions at the AGS. Quantitative calculations will be performed in Chapter 5 to extract the source size and temperature parameters of the source from these measurements. In Section 4.4, beam rapidity fragments will be presented and compared to lower energy results of the fragmentation region.

4.1 Light Fragment Single Particle Spectra

In the context of a flowing, thermal model [18] the measured transverse Boltzmann temperature of single particle specie can be interpreted as an underlying temperature parameter (T_B) and a transverse boost velocity (β_t), as was discussed in Section 1.3.1 The fact that all particle specie are boosted with a common velocity implies that heavier particles (e.g. d, H, He) will have a mean transverse momentum that is higher than that for lighter particles. As was shown in Fig. 1.3, the measured slope parameter T is approximately linear with ejectile mass, consistent with a constant boost velocity. Note also that the slope of the line in T vs. mass space increases with the size of the colliding system. This increase with source size has been attributed to an increase in the number of secondary collisions and produced particles for larger colliding nuclei, a trend which tends to drive the system to expand further. The larger the number of participants in the nuclear collision, the greater the transverse expansion due to these collisions.

Since the Boltzmann temperature parameters for pions ($T_B \approx 30 - 60$ MeV) and protons ($T_B \approx 100 - 300$ MeV) have been measured for our collisions in [47], one could expect that the deuteron and ^{3}H/^{3}He temperature parameters should be higher. In this section we will present invariant spectra of ^{2}H, ^{3}H, ^{3}He and compare them to proton and pion spectra previously measured by E877 [47].

4.1.1 Deuterons

Following the method outlined in Chapter 3, deuteron invariant multiplicities are calculated. Shown in Figure 4.1 is the deuteron spectra measured in the E877 spectrometer with a centrality cut on the 4% most central collisions.[1] Recall that each data point is the result of a multi-parameter fit in mass^2 space, corrected by the acceptance of our experiment as described in Section 3.10. The error bars in Fig. 4.1 represent only those related to the fit, and thus are indirectly related to statistical uncertainties, and do not reflect systematic error bars which have been estimated to be approximately 10% [47, 57].

While the protons and pions measured by our experiment [47] have temperatures between $100 - 300$ MeV and $30 - 60$ MeV [2] respectively, the deuteron

---

[1] Deuterons from 6-9% and 10-20% centrality regions are shown in Appendix C.

[2] The measured Boltzmann temperature is dependent on rapidity as would be the case for a simple thermal model where $d^3N/d^3p \propto exp(-m_t \cosh(y)/T_B)$. As such, the Boltzmann temperature is higher near mid-rapidity and falls off towards beam

spectra at mid-rapidity are very flat and are not describable by a finite temperature parameter. Since hadronic spectra are known to be essentially non-thermal [47], deviating at low p_t from a pure thermal distribution, the indeterminacy of our temperature measurement is likely due to the limited p_t acceptance of our apparatus: *i.e.* because E877 measures at low transverse momentum, our measurements tend to be near the shoulder of the 'shoulder-arm' transverse spectra. From $y = 2.1$ to $y = 2.6$, not only do the spectra become less flat than at mid-rapidity, we begin to measure far enough out in p_t to determine an effective temperature of the deuterons of $T_B(y = 2.5 - 2.6) = 205 \pm 15$ MeV, subject to the caveats previously noted.

The measured invariant multiplicities are consistent with those measured by E864 [62] and E866 [80] for Au + Pb and Au + Au collisions, respectively.

4.1.2 ^{3}He

Shown in Fig. 4.2 is the measured invariant multiplicity of ^{3}He for the $p_t = 0 - .5$GeV. Note that the ^{3}He acceptance in y is larger than that of the deuteron, reaching down to y = 1. However, the ^{3}He signal is statistics bound and, therefore, much larger rapidity and transverse momentum bins are needed in order to acquire enough statistics to produce a measurable yield in each bin. For rapidity bins 1.7-1.8 and 1.8-1.9, we measure ^{3}He out to a p_t of 1GeV. These points are shown in Fig. 4.3.

The error bars shown in Figs. 4.2 and 4.3 include only those deduced

---

rapidity.

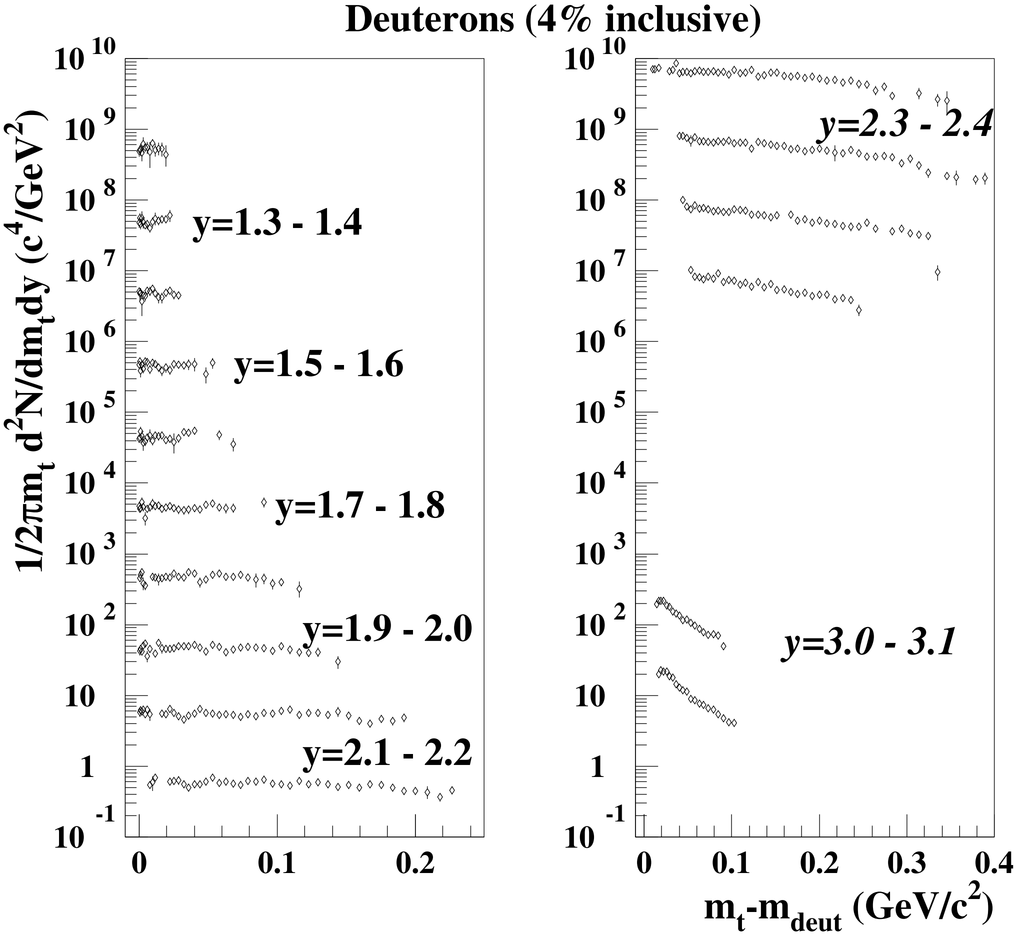

Figure 4.1: Invariant multiplicities of deuterons for the 4% inclusive centrality bin measured by E877. The spectra for $y = 3.1 - 3.2$ and $y = 2.1 - 2.2$ are correctly normalized and each rapidity bin below these is multiplied by successive powers of 10 for ease of display.

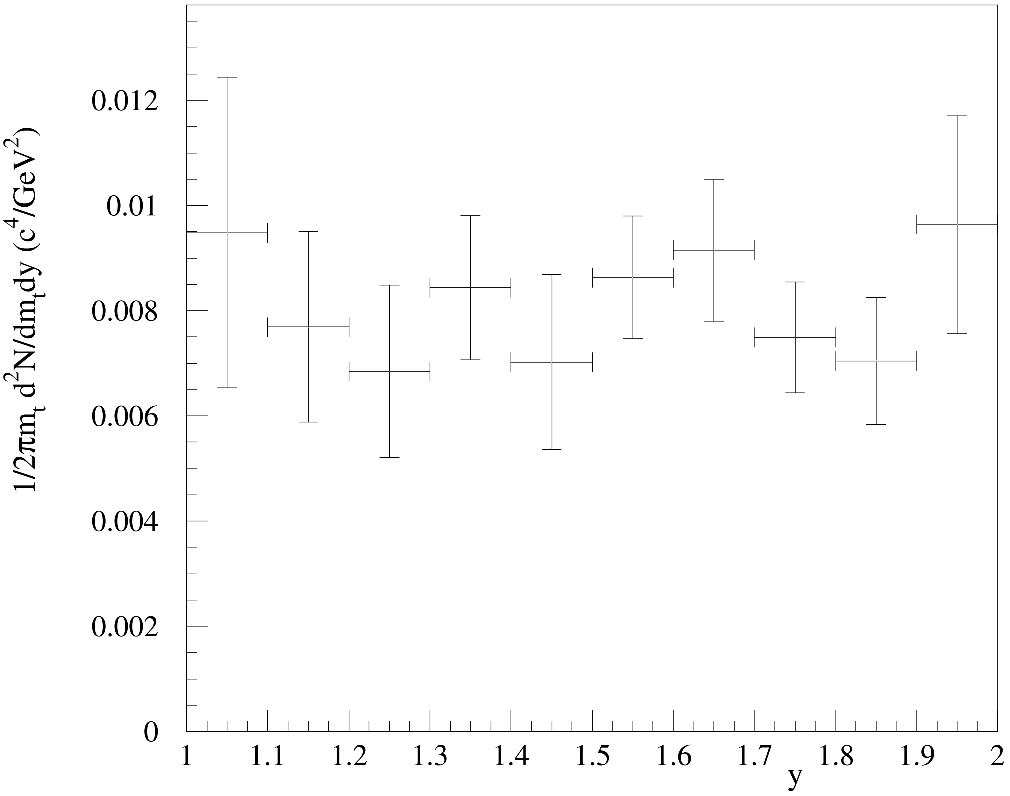

Figure 4.2: The ^{3}He invariant multiplicity as a function of rapidity for $p_t = 0.0 - 0.5$GeV.

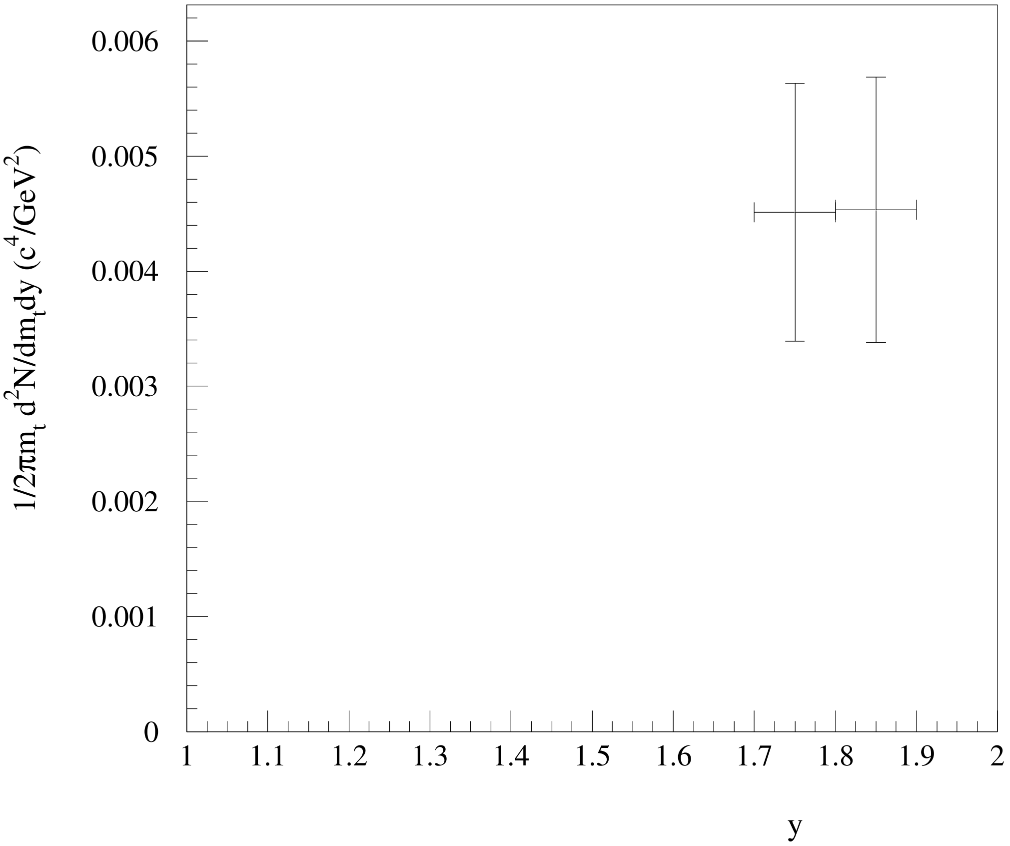

Figure 4.3: The ^{3}He invariant multiplicities for $p_t = 0.5 - 1.0$ GeV.

from the Gaussian fits described in Section 3.9.3 and therefore do not include systematic error bars. As ^{3}He is extracted from the mass^2 distribution by first cutting on the TOFU pulse-height ($2.2 < TOFU_{PH} < 3.5$), we have determined the effective signal of charge = 2 particles removed to be 85.3% (93.8%) for the linear (non-linear) fit; see Section 3.7 for details. We therefore assume a correction of 89.55% and accept an extra 5% systematic uncertainty in the absolute value of the invariant multiplicity; yielding a total systematic error of 12-16%.

The acceptance calculation for ^{3}He is performed assuming a particular shape of the transverse momentum distribution as described in Section 3.10.2. As we only have two bins in the transverse momentum spectra for ^{3}He, the iterative method, in which the output distribution is utilized as an input into the acceptance calculation, is not as effective for this case. The transverse temperature in the two rapidity bins in which we have more than one transverse momentum bin is found to be approximately 180 MeV and this value is utilized as input into the acceptance calculation. However, corrections for 450MeV (50MeV) have shown a 5% increase (decrease) in the relative yield of the reconstructed ^{3}He spectra.

Note that ^{3}He is extractable from the mass^2 distributions only for rapidities between y = 1 and y = 2. While ^{3}He at beam rapidity are accepted into the experimental apparatus, due to the increase in the m^2 distributions at large momentum, the ^{3}He peak is overwhelmed by the proton and deuteron peaks beyond y = 2 and are therefore unmeasurable. The invariant multiplicity for ^{3}He at low p_t is flat over our measured rapidity range about mid-rapidity

$p_t = 0.0 - 0.5$GeV/c	$p_t = 0.5 - 1.0$GeV/c
$.0080 \pm .0005$GeV^{-2}	$.0045 \pm .0008$GeV^{-2}

Table 4.1: Invariant Multiplicity of ^{3}He $(1/2\pi p_t d^2N/dp_t dy)$ at mid-rapidity

$p_t = 0.0 - 0.33$GeV/c	$p_t = 0.33 - 0.67$GeV/c
$.0069 \pm .0009$GeV^{-2}	$.0074 \pm .0008$GeV^{-2}

Table 4.2: Invariant Multiplicity of ^{3}H $(1/2\pi p_t d^2N/dp_t dy)$ at mid-rapidity

$(y = 1.6)$, similar to the deuterons. The values of the invariant multiplicity averaged over rapidity are shown in Table 4.1 These data are in agreement with preliminary spectra from E866 Au + Au [80] and E864 Au + Pb [62] reactions at low p_t.

4.1.3 Tritons

^{3}H are gleaned from the mass^2 distributions via the method described in Section 3.9.2. Due to their low yield coupled with the fact that the deuteron peak washes out most of the signal, only a few bins in rapidity and p_t can be extracted. Shown in Fig. 4.4 is the triton invariant multiplicity for $p_t = 0.0 - 0.33$ GeV as a function of rapidity; the error bars only reflect the uncertainty in the fitted function and do not include any systematic errors. The average invariant multiplicity over the measured rapidity range is shown in Table 4.2.

The acceptance calculation for tritons follows that described above for ^{3}He since the total yield can only be determined in two p_t bins. As such the invariant multiplicity distributions are determined poorer than for more abundant particles and is dependent on assumptions of the input distribution to the acceptance calculations, see Section 3.10.2. Varying assumptions of

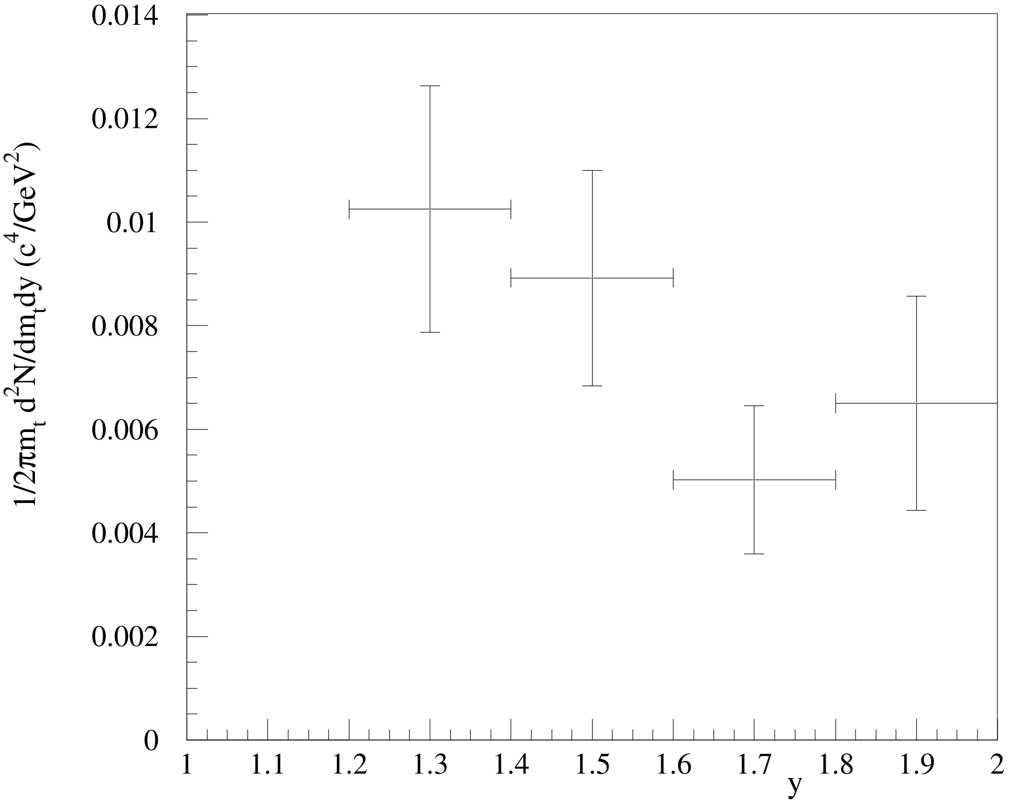

Figure 4.4: The ^{3}H invariant multiplicity as a function of rapidity for $p_t = 0.0 - 0.33$GeV/c.

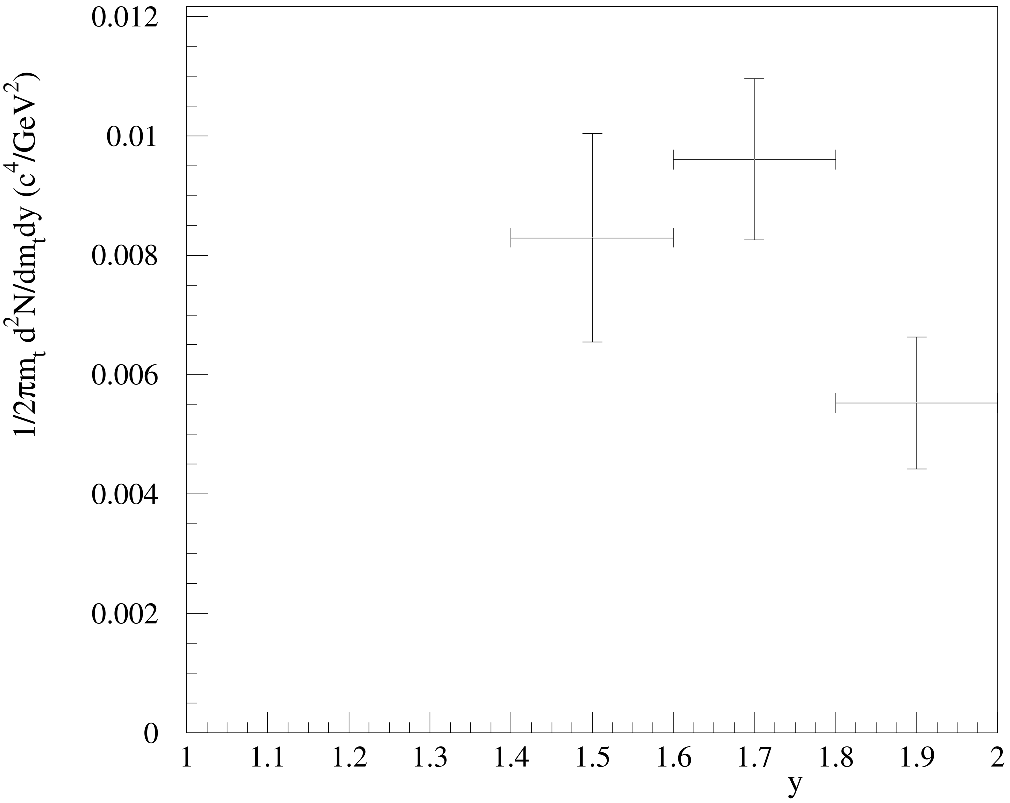

Figure 4.5: The ^{3}H invariant multiplicity for $p_t = .33 - .66$ GeV/c.

this distribution were found to change the overall ^{3}H invariant multiplicity by 5%. As such an extra 5% systematic error is additionally assumed for the ^{3}He multiplicities, resulting in a total 12-16% systematic error.

One should expect that the invariant multiplicities of ^{3}H and ^{3}He would be consistent within an overall constant to account for any disparity in isospin in the source. We find that, accounting for all statistical and systematic error bars, these multiplicities are consistent with one another.

4.2 Coalescence vs. Fragmentation

To aid in visualizing the deuteron multiplicity, a three dimensional plot for the 4% inclusive centrality bin is shown in Fig. 4.6. In this plot, it is easier to see that the deuteron spectra are not only relatively flat as a function of p_t but are also flat as a function of rapidity. Further, the deuteron multiplicity is highly peaked at beam and target rapidities, a fact that has caused speculation as to whether or not deuterons from heavy ion collisions are all fragmented spectator matter and, therefore, not formed via coalescing pairs from the fireball region.

In the opinion of the author, this conjecture might be naively discarded by pointing out that the binding energy of a deuteron (2.24MeV) is much smaller than the momentum boost of a couple GeV necessary to displace it from the beam region to mid-rapidity. However, we will let the data be the proof and investigate this conjecture through the centrality dependence of the data.

Shown in Fig. 4.7 is the invariant multiplicity of deuterons for both

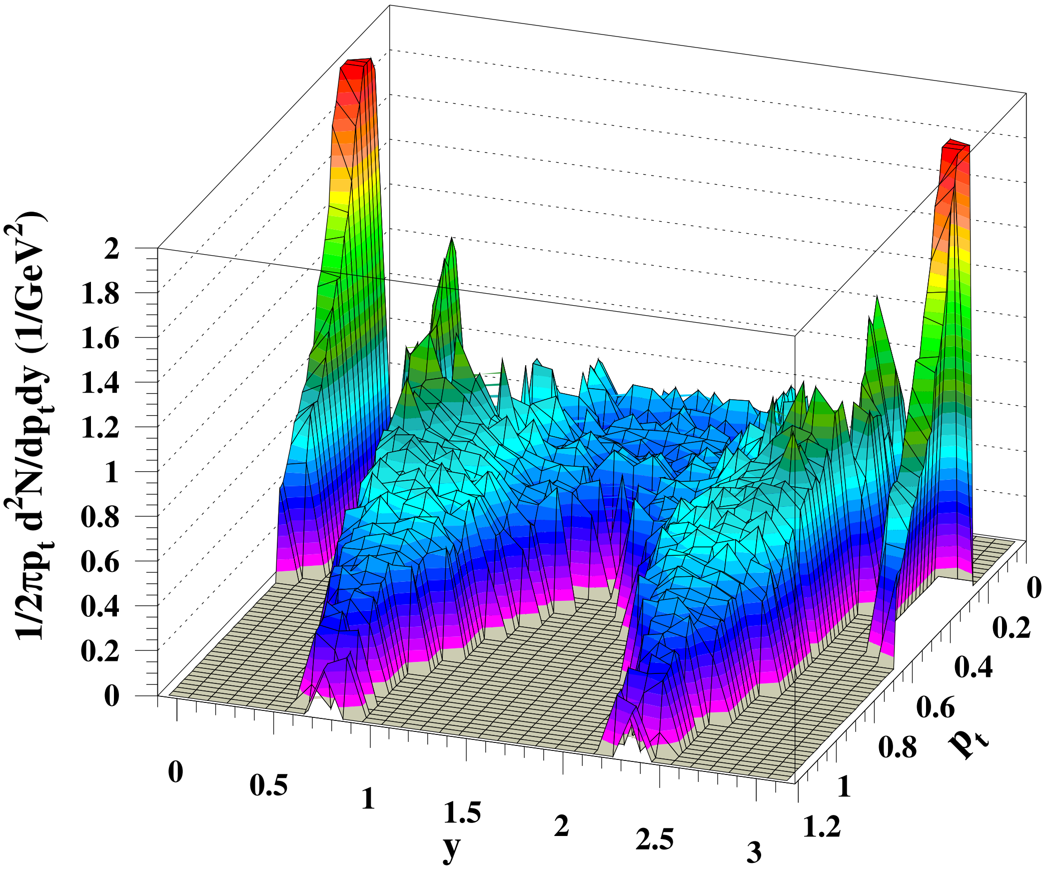

Figure 4.6: Invariant multiplicity as a function of p_t (GeV/c) and y for deuterons.

Centrality Percentage	Participants	Spectators
0-4%	347	47
6-9%	278	116
10-20%	221	173

Table 4.3: Approximate number of participants and spectators for various centrality bins.

the 4% inclusive and $6-9\%$ centrality cuts. The fractional change in the number of participating nucleons between these two centralities is relatively small, though the fractional change in the number of spectator nucleons is significant. From the hard sphere calculation shown in Appendix E we can determine the number of participants and spectators for each of the centrality bins. These results are shown in Table 4.3. Note that between the top two centralities, the number of interacting nucleons decreases by a factor of 1.3 while the number of spectators increases by a factor of 2.5. This is equivalent to what is seen in the data, where there is little difference between the two centrality regions in the mid-rapidity range and a factor of two difference in the beam rapidity deuteron multiplicities. We thus conclude that the deuterons in the mid-rapidity region are formed from coalesced nucleons in the interacting fireball region while only those within .1 units of beam rapidity and at low p_t are fragmented from the beam spectator region.

4.3 The Coalescence Parameter B_A

After the light fragment invariant spectra have been determined, the coalescence parameter for both A=2 and A=3 nuclei can be calculated. This

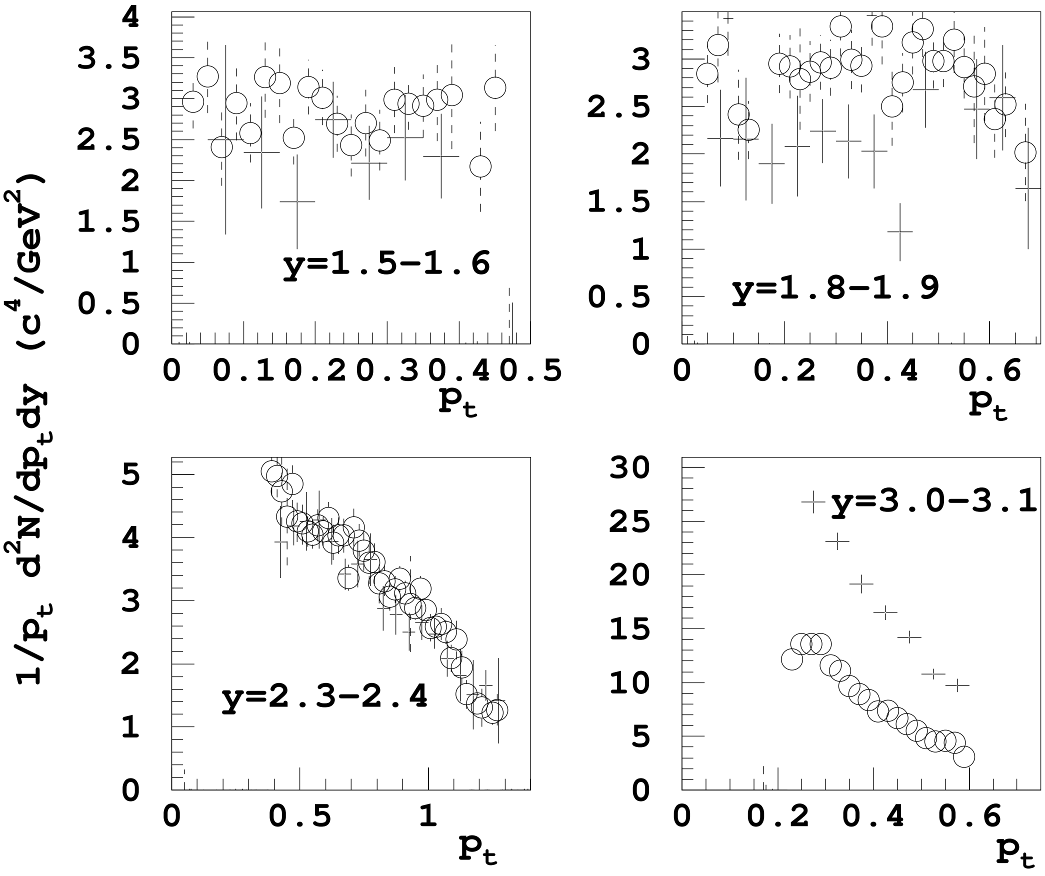

Figure 4.7: Deuteron invariant cross section for two different centralities at mid and beam rapidities. The circles and crosses represent the 4% inclusive 6-9% centrality bins, respectively.

calculation is performed in this section for deuterons and ^{3}H/^{3}He in Sections 4.3.1 and 4.3.2, respectively. In Section 4.3.3 these values will be compared to measurements for other systems and energies.

4.3.1 Deuterons (B_d)

As described in Chapter 1, deuteron production has traditionally been described in terms of a coalescence parameter, B_d defined as

$$E_d \frac{d^3 N_d}{dp^3}(P_d) = B_d \left(E_p \frac{d^3 N_p}{dp^3}(P_p) \right)^2 \tag{4.1}$$

where $P_d = 2P_p$; that is, the deuteron and proton distributions are evaluated at the *same velocity*. B_d, in simple theories, is independent of transverse or longitudinal momentum though both Bevalac and SPS data have noted a p_t dependence of B_d at mid-rapidity [21, 64]. The exact reason for this dependency is unclear but may be due to collective flow behavior [69].

Since B_d is ideally the deuteron invariant multiplicity divided by the proton and neutron invariant multiplicities, one might consider normalizing the ratio of deuteron to proton^2 in Eq. 4.1 by the neutron-to-proton ratio of the system at freeze-out. Naively, one could simply use the neutron-to-proton ratio of the colliding nuclei as this value. However, even in p-p collisions [65] the ratio of neutrons to protons at freeze-out is $\sim .7/1.3$, nearly equilibrating over isospin in the nucleon sector. In a heavy-ion collision, it is expected that each proton and neutron will suffer several such interactions resulting in a system with nearly as many neutrons and protons at freeze-out. This qualitative argument is also consistent with pion isospin content: the π^-/π^+ ratio is approximately 1.2 [40], weighted towards negative isospins. Therefore, the data presented are uncorrected for any neutron to proton ratio.

To calculate B_d for our apparatus, 1993 proton spectra are utilized [47]. The data sets from '93 and '94 have been shown to be consistent [56], however, the 1993 configuration included measurements in two polarities of the magnet setting such that the proton spectra cover phase space more completely [47]. The statistics of the 1993 data set is lower by a factor of ten and, as such, the deuteron yield is extremely low. Therefore, the 1994 deuteron spectra and 1993 proton spectra are utilized to determine B_d.

Ideally B_d is the deuteron invariant multiplicity divided by the proton invariant multiplicity squared *evaluated at freeze-out.* Since our measurement of the proton spectra includes those protons from hyperon decays (*e.g.* Λ, Σ, Ξ) which decay long after the collision has already frozen out ($c\tau_\Lambda = 7.89$ cm), they need to be removed from the calculation of the coalescence parameter. A study of this contamination has been done previously [47] and is modified and expanded in Appendix A.

After the hyperon contamination has been accounted for, B_d is calculated over all measurable phase space. Shown in Fig. 4.8 is B_d for various rapidities as a function of p_t for the 4% most central events. Note that B_d is fairly constant over transverse momentum though it clearly depends on rapidity, being nearly a factor of 2 larger at $y \approx 2.1$ than at mid-rapidity. This difference cannot be accounted for by hyperon contamination. We attribute the dependence of B_d on rapidity to longitudinal source-size dependencies [30, 69, 79].

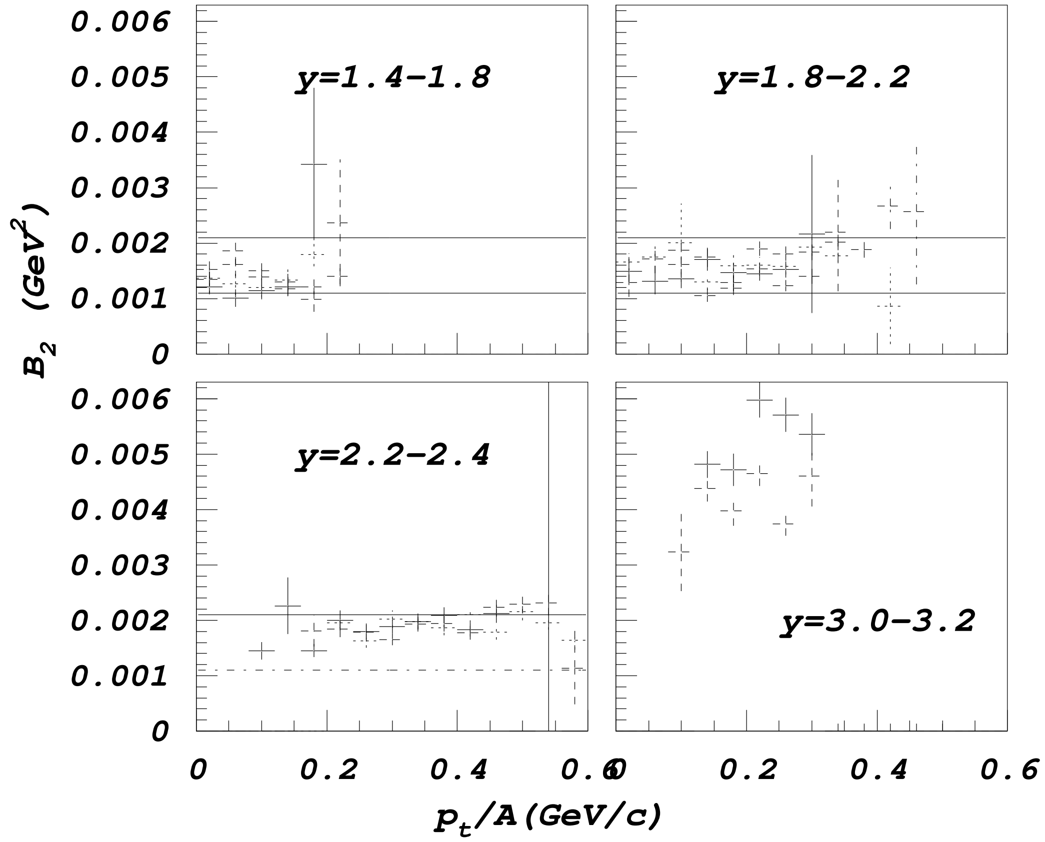

Figure 4.8: B_d as a function of p_t and y for the 4% most central events. The lines correspond to the upper and lower bounds taken as the error bar of B_d measured by E877.

At beam rapidity, B_d is significantly larger and highly dependent upon transverse momentum. However, since this is a region of fragmentation from the spectator region, it is not anticipated that it will be amenable to a coalescence picture. We will only utilize the value of B_d at non-beam rapidity regions for the coalescence analysis.

The average value of B_d over the entire phase space of the acceptance, excluding the beam region, will be taken as our experimental value with error bars consistent with the rapidity variations: $B_d = (1.5 \pm .5)10^{-3} GeV^2$. This value is consistent with E878 central Au+Au ($B_d \approx (1.8 \pm 1)10^{-3} GeV^2$) and E864 central Au+Pb ($B_d \approx (.6 \pm .4)10^{-3} GeV^2$) preliminary measurements [62] at $y = 1.7$ and $y = 1.9$ respectively.

Shown in Fig. 4.9 is B_d for the centrality cut of 6-9%. Here B_d shows the same dependencies for the lower centrality, independent of p_t and increasing away from mid-rapidity. The values for this bin are consistent with those from the 4% inclusive centrality bin: $B_d = (0.8 \pm 0.4)10^{-3}\mathrm{GeV}^2$.

4.3.2 Tritons/^{3}He (B_3)

Similar to calculations for deuterons above, we can determine B_3 for tritons and ^{3}He determined by

$$E_3 \frac{d^3 N_3}{dp^3}(P_3) = B_3 \left(E_p \frac{d^3 N_p}{dp^3}(P_p) \right)^2 . \tag{4.2}$$

For calculations of B_3, a full function of p_t and y, as was performed for deuteron, is unfeasible due to the limited number of bins for A=3 particles.

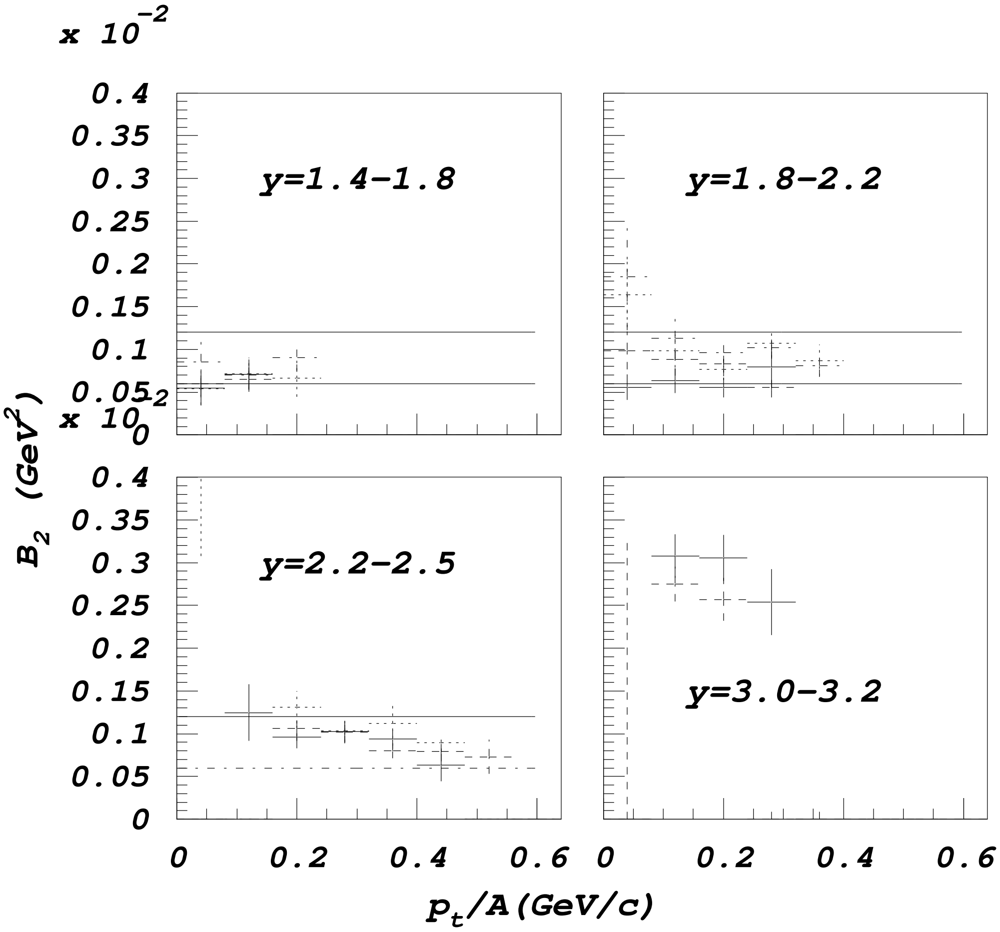

Figure 4.9: B_d as a function of p_t and y for the 6-9% most central events. The lines correspond to the upper and lower bounds taken on the error bar of measured B_d.

Therefore, we calculate this ratio by utilizing the p_t averaged value of the proton invariant spectra and the first bin in p_t of the ^{3}H or ^{3}He spectra. Since these spectra overlap only within $1.2 < y < 2.0$, the approximation of the proton spectra as a constant is fine since we do not measure beyond $p_t = 0.3$ GeV in these bins; the proton spectra are constant throughout this transverse momentum region. The proton spectra used are corrected for Λ feed-down.

Shown in Fig. 4.10 are the calculated values of B_3 at $p_t = 0$ for both ^{3}H and ^{3}He as a function of rapidity for the 4% most central collisions. Both distributions are flat within our statistical error bars and, therefore, we determine them as single valued functions. For our experiment

$$\begin{aligned} B_{^3H} &= (1.19 \pm .29)10^{-6} GeV^4/c^6 \\ B_{^3He} &= (1.25 \pm .23)10^{-6} GeV^4/c^6. \end{aligned}$$

These figures include only statistical error bars. Systematic errors are estimated to be 15-22% due to experimental efficiencies, TOFU cuts, and Λ feed-down corrections. Notice that the measured values of $B_{^3H}$ and $B_{^3He}$ are the same, consistent with the coalescence assumption.

4.3.3 Excitation Function of B_A

> *A new scientific truth does not triumph by convincing its opponents and making them see the light, but rather because its opponents eventually die, and a new generation grows up that is familiar with it.* [Max Plank]

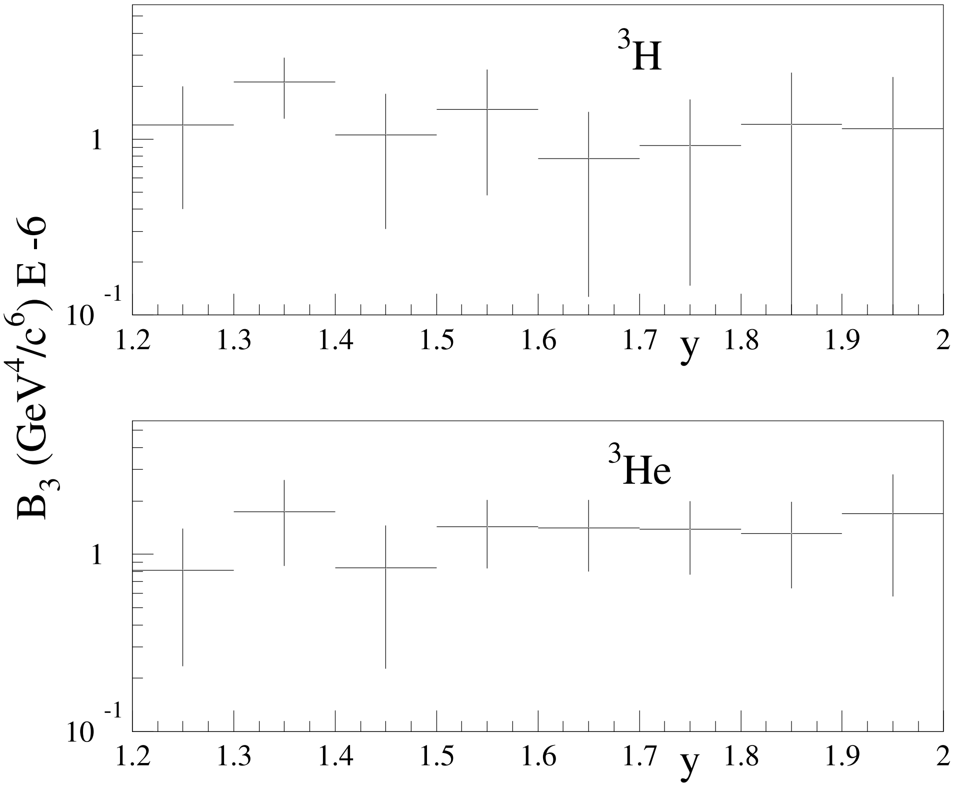

Figure 4.10: B_3 for ^{3}H and ^{3}He as a function of y for the 4% most central collisions. Error bars reflect only statistical errors.

Deuterons: B_d

Recall from Chapter 1 that the coalescence factor was first assumed to be constant for all systems and energies in heavy-ion and p-p collisions but has recently been noted to be dependent on the volume of the system at freeze-out.

Shown in Figure 4.11 is an excitation function of B_d for various centralities and systems from Bevalac to SPS energies including the values determined in this thesis. As was described in Chapter 1, the precipitous drop at AGS energies has been qualitatively described as an increase in the volume at freeze-out [30] and, from density matrix models, is approximately proportional to the inverse volume of the system at freeze-out[36]. This theory is consistent with measurements from this thesis as well. The value of B_d for Au + Au collisions is less than that for Si + Pb collisions by a factor of 2 or 3, consistent with the HBT measurements of relative increase in volume between these two systems [70].

Furthermore, this increase in the relative volume is also consistent with preliminary proton-proton correlations measured by E877 [58]. The proton-proton correlation arises from the combination of coulomb, strong and Fermi interactions which produce a characteristic 'dip-bump' as shown in Figs. 4.12. The height of the correlation at $q \sim 20$MeV, which decreases by a factor of three from Si + Pb to Au + Au collisions, is related to the volume of the system at freeze-out in simple models [71]. Therefore, the measured B_d, which could be interpreted as a proton-neutron correlation [33], is consistent with the proton-proton correlation results.

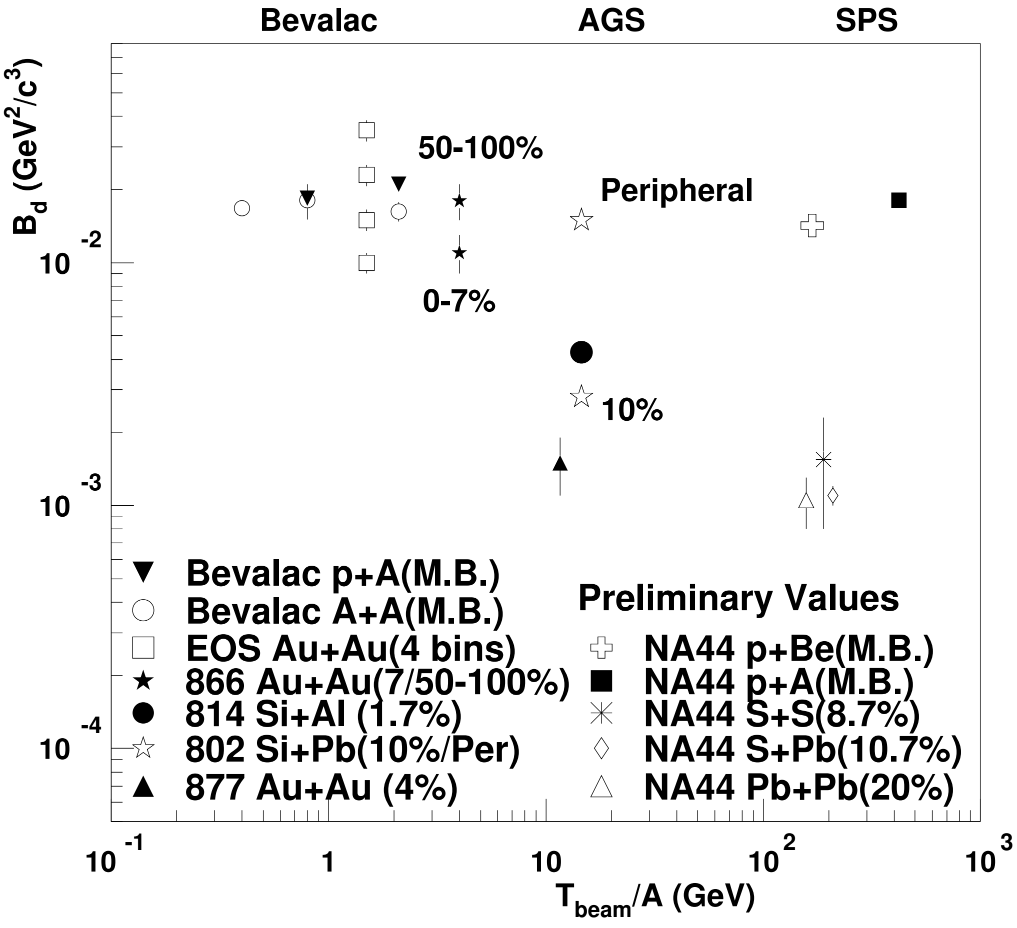

Figure 4.11: B_d for a variety of systems and energies. The values in parenthesis are the centrality cut, where 'M.B.' corresponds to minimum bias events. The data are taken from [20, 21, 22, 23, 27, 28, 29, 64]. All NA44 data points are preliminary.

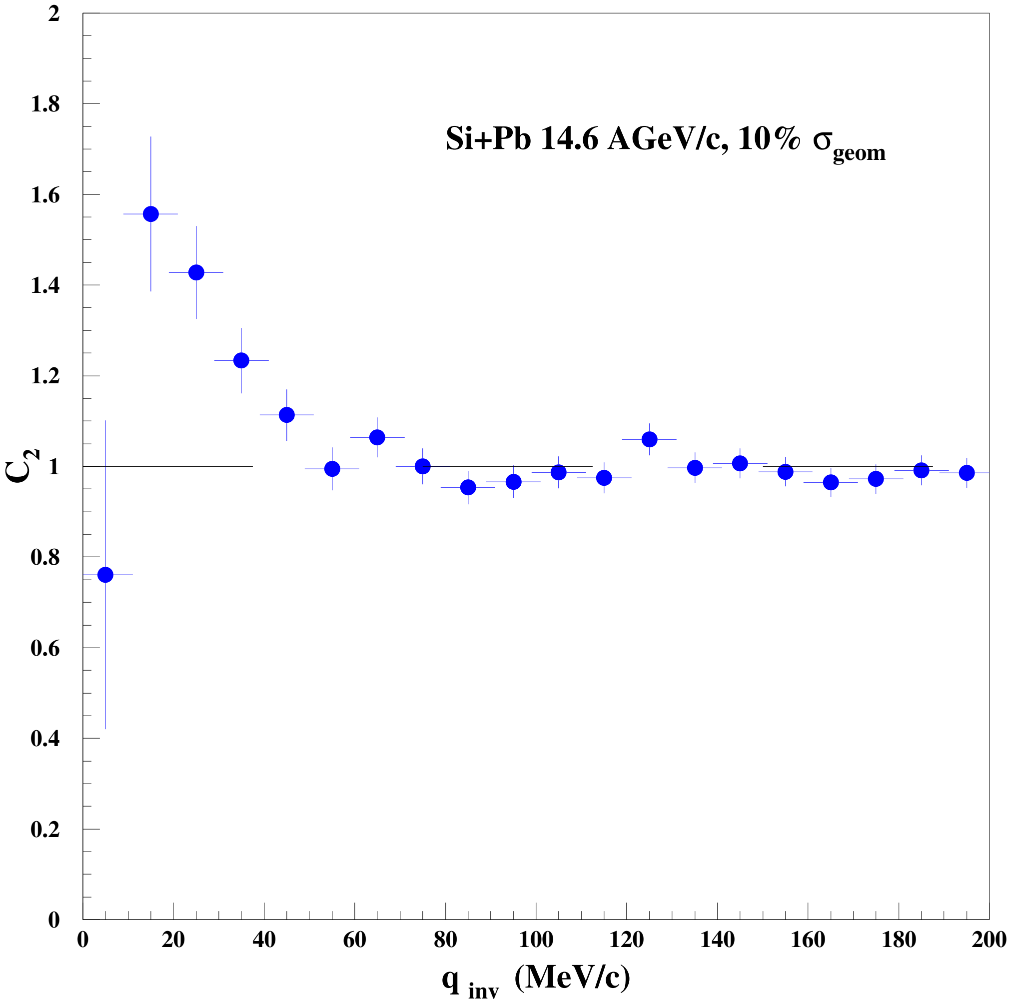

Figure 4.12: Proton-Proton correlations from [58] for Si + Pb collisions measured by E877.

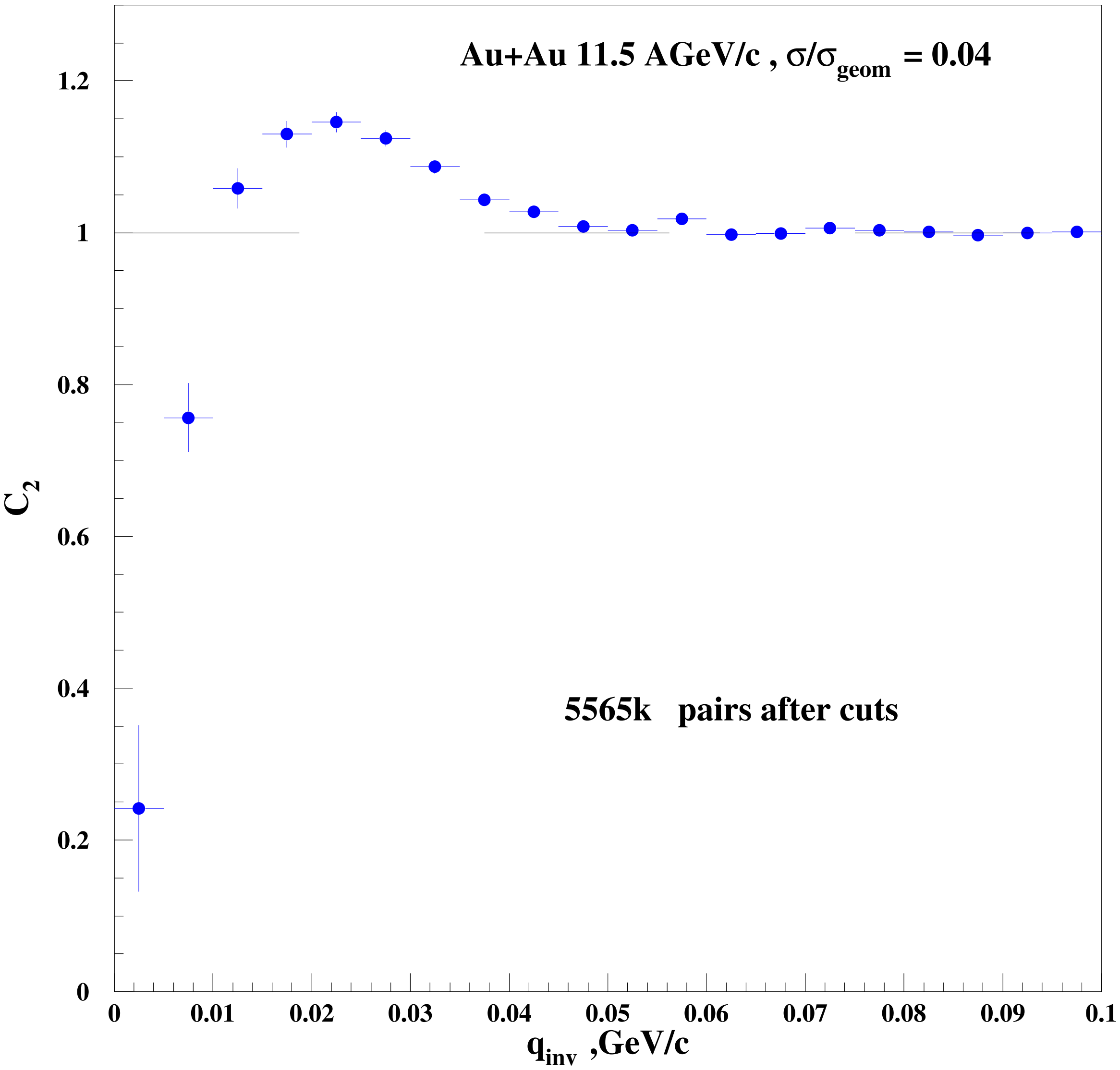

Figure 4.13: Proton-Proton correlations from [58] for Au + Au collisions measured by E877.

Intruigingly, preliminary NA44 data [28, 64] for S + S (8.7% central), S + Pb (10.7% central) and Pb + Pb (20% central) collisions, which have been corrected for hyperon contributions to the proton spectra, are consistent with Au + Au values at AGS.[3] This limiting behavior is inconsistent with any simplistic theory of deuteron production which would predict an inverse volume dependence of the coalescence parameter. Instead, it appears from the limited data that this parameter may have reached another saturation point that begins near the pion production threshold, where the system must necessarily expand significantly before freezing out.

Although the points from NA44 and E877 Au + Au collisions are consistent within error bars, it should be noted that the NA44 measurements are taken at various centralities which may conspire in such a way as to account for the coincidence: the Pb + Pb collisions are measured for the most 20% collisions while the S+ Pb are at 10.7%, and the S + S are at 8.7%. This change in centrality, which we have learned from the E814 measurements may significantly change the coalescence parameter [22], is arranged in such a way that the choice of centrality cut and system size may have canceled to cause the points to all over-lie. This systematic should be checked; ideally, one would

---

[3] NA44 publications to date have chosen to quantify deuteron production by $(dN_d/dy)/(dN_p/dy)^2$. This is clearly a different parameter than is used in this thesis, from simple dimensional arguments. To get comparable results, their spectra have been taken directly from their publications [64] and utilized to calculate B_d. These values, which include an error bar which accounts for their measured p_t dependence, are plotted in Fig. 4.11.

like to see these same measurement for the most central few percent collisions to see if this saturation effect persists.

Tritons/^{3}He: B_3

Values of $B_{^3H}$ measured at Bevalac for nucleus-nucleus and proton-nucleus collisions [20] and Si+Pb collisions measured by E814 [22] are shown in Fig. 4.14 along with the data measured in this thesis. A similar plot for $B_{^3He}$ is shown in Fig. 4.15. A distinct feature of these spectra is an increase in B_3 from the lowest energy nuclear collisions at the Bevalac to a maximum value near $.1 < T_{beam}/A < 2$GeV of approximately $(1-2)10^{-4}$GeV^4/c^6. Similar to the measurements of B_d, the measured B_3 for both ^{3}H and ^{3}He decreases dramatically at the AGS energies by an order of magnitude for Si+Pb collisions and another order of magnitude for Au + Au collisions.

At lower energies, the nuclear force is a much larger contributer to the overall process of nuclear fragmentation. In this region, corresponding to the lower beam energy section of both B_3 curves, light fragments are formed by being boiled off an excited nucleus. As the beam energy is increased, the internal excitation energy of the system increases and the number of light fragments per nucleon^A increases. However, as we move beyond Bevalac energies, the coalescence parameter decreases dramatically. At this point a turnover occurs because the threshold for pion production has been crossed and the system size at freeze-out has increased beyond the mean radius of the light fragment [30]. Therefore, the shape of the B_3 curves can be qualitatively described by two competing mechanisms: an increasing nuclear excitation energy increases

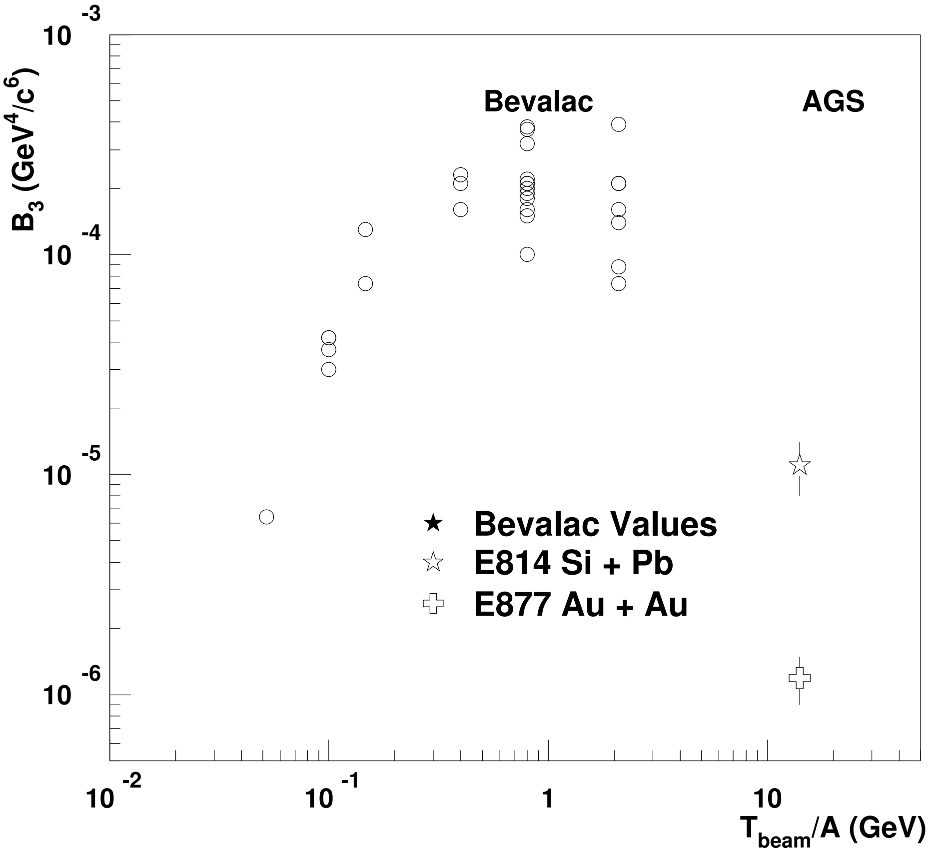

Figure 4.14: An excitation function of B_3 for ^{3}H. The circles correspond to Bevalac pA and AA collisions. The star and cross correspond to 814 Si + Pb collisions and 877 Au + Au collisions. Values are taken from [20, 22].

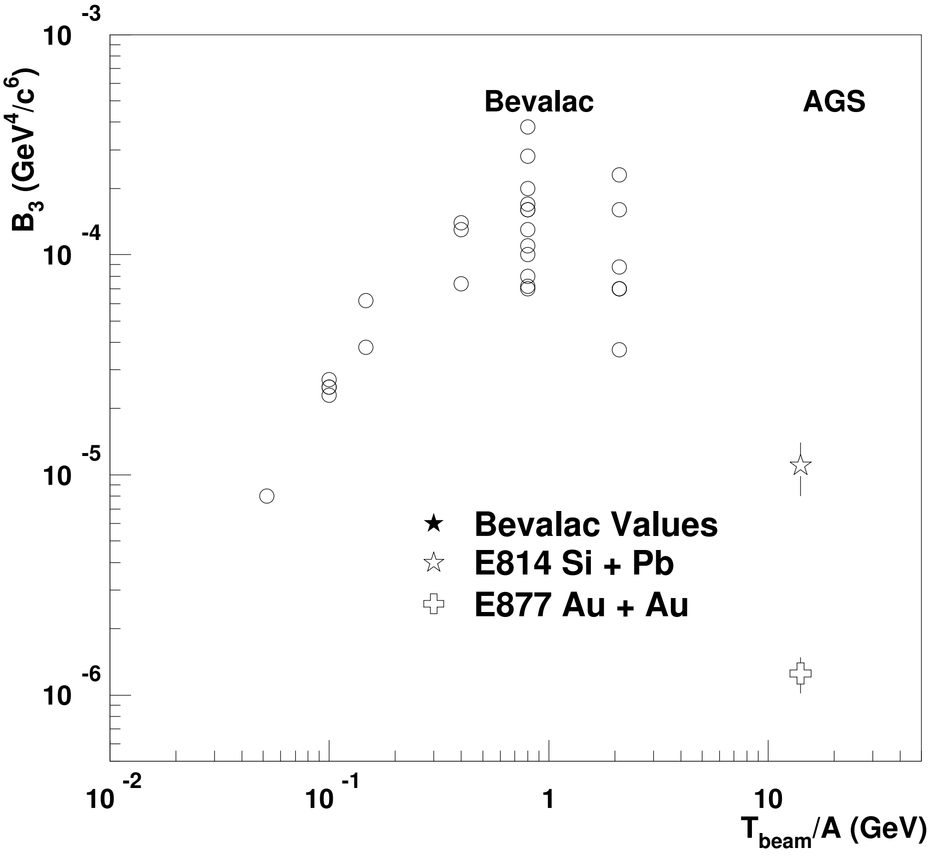

Figure 4.15: An excitation function of B_3 for ^{3}He. The circles correspond to Bevalac pA and AA collisions. The star and cross correspond to 814 Si + Pb collisions and 877 Au + Au collisions. Values are taken from [20, 22].

the light fragment yields from 50 MeV/A to 2 GeV/A in the Bevalac regime followed by a sharp decrease from volume effects at AGS energies.

4.4 Beam Rapidity Measurements

E877 has the unique opportunity to measure beam rapidity light fragments at AGS energies. The beam rapidity region contains information completely separate from that gleaned from mid-rapidity spectra, including insight into the nuclear liquid-gas phase transition and measurements of flow variables.

In this Section beam rapidity fragments will be presented and discussed in light of measurements at lower energies where systematic studies of this region have been performed. Although these studies are somewhat beside the central point of this thesis, we include them here for completeness.

4.4.1 The Liquid-Gas Phase Transition

Studies of the fragmentation of spectator matter have been a source of continual fascination in heavy-ion collisions, especially at lower energies. Above a beam energy of a few hundred MeV per nucleon, the distribution of fragments has been shown to be invariant with respect to the entrance channel by the ALADIN collaboration at SIS [24]; the average number of projectile like intermediate mass fragments (IMF's) as a function of the total bound charge in the fragmenting spectator matter is independent of target above 400 MeV. Qualitatively, one can understand an invariance of the fragment spectra as a function of entrance channel by considering the collision process from the point of view of a nucleus which is shaved of a large portion of nuclei. Above some beam energy, the distribution of the spectator matter will be independent of the beam energy because the participant particles will be removed before the spectators are aware of it. From that point on, only the dynamics of nuclear matter in its excited state will govern the fragment emission function.

The results of temperatures from isotope yields has been measured by the ALADIN collaboration as a function of the excitation energy of the spectator matter and a caloric curve has been deduced as is shown in Fig. 4.16 [25]. The authors speculate that this curve of a qualitative temperature versus excitation energy corresponds to a phase transition between a fermionic system at low excitation energy to a classical gas at high excitation energy, that is the nuclear liquid-gas phase transition.

Whether or not this curve actually corresponds to a phase transition, the measured temperature from isotope yields may be meaningless when compared to the energy spectra of those same fragments, which have a larger temperature by nearly an order of magnitude. This point seems to be inconsistent with the theory that the excited nuclear matter decouples at some thermal point. In fact, this analysis has come under scrutiny and may not be related to the an actual phase transition but may instead be related to dynamical processes that are non-thermal [26].

While a full study of the fragmentation region is beyond the scope of this thesis, the fact that E877 is in a unique position to make these measurements at AGS energies makes it incumbent on us to provide those measurements that are available. As such, the following two sections will discuss those fragments

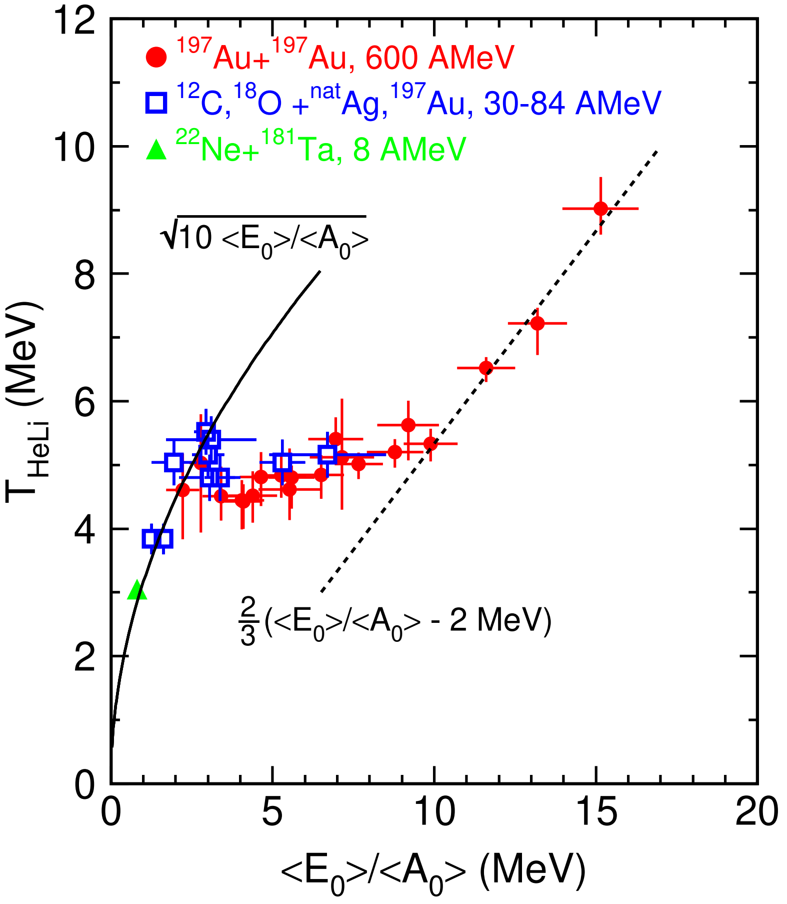

Figure 4.16: Caloric curve of nuclear matter as determined from the isotope ratio temperature and the excitation energy per nucleon. The lines correspond to a fermionic system at low excitation energy ($\sqrt{\langle E_0\rangle/\langle A_0\rangle}$) and a classical gas of elementary particles at high excitation energy ($\frac{2}{3}(\langle E_0\rangle/\langle A_0\rangle - 2MeV)$). Figure taken from [25].

measured by us at beam rapidity, deuterons and ^{4}He. While experiment 877 can measure the transverse energy distribution of spectator matter, similar to that measured at lower energies, we cannot confirm the isotope ratios measured by ALADIN because most fragments above ^{4}He are lost as they travel along with the beam particles through the deadened regions of the drift chambers.

4.4.2 Beam Rapidity Deuterons

Though a distinct gap occurs in the data from $y = 2.6{-}3.0$ due to the inextractability of deuterons from the proton peak (see Section 3.9), beam rapidity deuterons are clearly extracted and have a measured Boltzmann temperature of $T_B(y = 3.0 - 3.1) = 49.6 \pm 1.4\text{MeV}$ and $T_B(y = 3.1 - 3.2) = 42.5 \pm 1.1\text{MeV}$ for the 4% inclusive centrality bin.

The low temperature in this region of phase space derives from two separate sources and does not necessarily reflect the true temperature of the fragments. First, the low measured Boltzmann temperature at beam rapidity arises from simple conservation of energy considerations in a simple thermal model; that is, since a thermal distribution is given by $exp(-E/T) = exp(-m_t \cosh(y)/T)$ the fact that the temperature is low near beam rapidity is simply due to the $\cosh(y)$ dependence in the exponential. For example, the proton Boltzmann temperatures at beam rapidity have been found to be between 50 and 100 MeV [47] in the 4% inclusive bin, from a maximum near ~ 250 MeV closer to mid-rapidity. Furthermore, protons measured at beam rapidity are consistent with a thermal model and do not contain a measurable number of fragments from the spectator region [47].

However, as has been described in Section 4.2 above, these deuterons are consistent with a fragmentation scenario from the simple comparison of differing centrality bins. Therefore, we hypothesize that the beam-rapidity deuterons include allotments due to both fragmented spectator matter and coalesced nuclei from the interaction region. As a result, the deuteron spectra should be composed of two regions of different transverse shapes.

Shown in Fig. 4.17 are measured deuteron spectra at beam rapidity for three distinct centralities. The spectra are similar, within an overall constant, though the χ^2 difference between the 4% and 10-20% data points, within a normalization constant, is 3.12, implying that the spectra vary slightly beyond a simple multiplicative factor. Fitting each of these spectra to a Boltzmann temperature yields

$$\begin{aligned} T(\sigma/\sigma_0 = 4\%) &= 49.6 \pm 1.4\text{MeV} \\ T(\sigma/\sigma_0 = 6-9\%) &= 60 \pm 3\text{MeV} \\ T(\sigma/\sigma_0 = 10-20\%) &= 83 \pm 2\text{MeV}. \end{aligned}$$

These increasing Boltzmann temperatures are partially attributable to the fact that the spectra at beam rapidity are not described by a Boltzmann distribution, a fact shown by the fitted normalized χ^2 of 4.3 from the Boltzmann fit in Fig. 4.17. Since we expect that the deuterons at beam rapidity will be composed of two Boltzmann temperatures, from fragmentation and coalesced deuterons, a correct comparison should fit the spectra from different

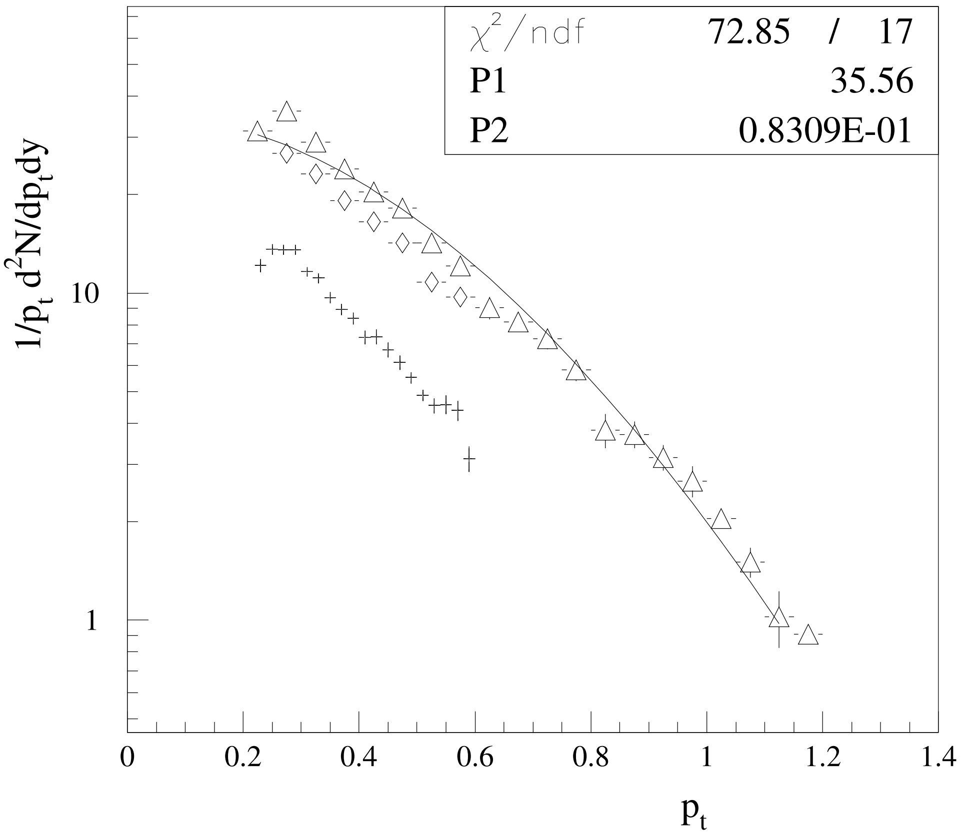

Figure 4.17: Beam rapidity spectra for various centrality regions. The triangles correspond to the 10-20% centrality range, the diamonds to the 6-9%, and the crosses to the 4% inclusive. The parameters and fitted line correspond to a Boltzmann fit $(P1 m_t/m_p \exp(-(m_t - m_p)/P2))$ to the 10-20% region.

centrality regions over the same p_t range. If the 10-20% and 6-9% centrality regions are fit to the same region in p_t as the 4%, we find that:

$$\begin{aligned} T_{lim}(\sigma/\sigma_0 = 4\%; p_t = .25:.55) &= 49.6 \pm 1.4 MeV \\ T_{lim}(\sigma/\sigma_0 = 6-9\%; p_t = .25:.55) &= 60 \pm 3 MeV \\ T_{lim}(\sigma/\sigma_0 = 10-20\%; p_t = .25:.55) &= 61 \pm 3 MeV. \end{aligned}$$

Therefore, there is a greater than 3 σ difference in the deuteron temperature between the most central and least central collisions measured by 877.

In Fig. 4.18 is the deuteron $d^2N/dp_x dy$ at beam rapidity for the 10-20% centrality region where x is the direction of the reaction plane. This spectra is determined by defining all deuterons emitted within 45^o of the reaction plane to be positive x while those emitted at greater than 135^o from the reaction plane to be negative x. The distribution has a Gaussian width of 443 ± 14 MeV, significantly larger than those widths measured at Bevalac energies [20] which are close to 70 or 80 MeV.

This significant variance from the Bevalac distributions implies that the region of invariance of beam fragments with respect to entrance channel has not been reached at the Bevalac. In order to determine if the AGS is the point of invariance, one would need to measure fragments at higher energies still.

Also from Fig. 4.18, one can determine the mean transverse momentum of deuterons at beam rapidity. The mean transverse momentum $\langle p_x \rangle$ and its excitation function has been used to study the collective behavior of heavy ion collisions [48]. We note that the raw deuteron value is 193 ± 11MeV/c.

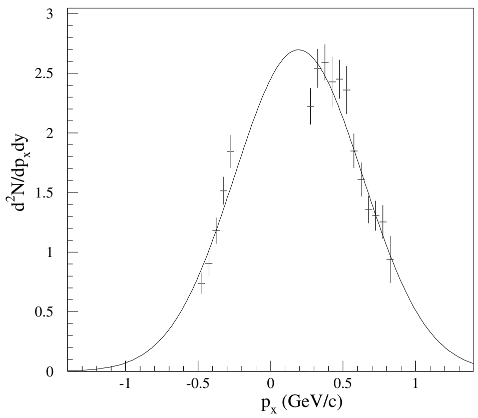

Figure 4.18: d^2N/dp_xdy at beam rapidity where x is the reaction plane direction.

However, our ability to measure this value is dependent upon our effectiveness in reconstructing the reaction plane. A thorough study of this resolution for E877 has been done [48] and the resolution for this centrality region causes a correction of 1.85, resulting in $\langle p_x \rangle = 360 \pm 21$MeV. The measure $\langle p_x \rangle$ of protons was measured for Au + Au collisions by E877 [48] and found to be 130 ± 10MeV. One might consider the deuteron mean transverse momentum to be a factor of two larger than the proton measurements simply from fact that the deuteron is composed from protons and neutrons at freeze-out and is coalesced at the same velocity. However, the measured $\langle p_x \rangle / A$ for deuterons is larger than that of protons.

4.4.3 Beam Rapidity ^{4}He

^{4}He is also measured in our experimental apparatus. Though the statistics of ^{4}He at non-beam rapidities is very low (see Appendix B), beam rapidity ^{4}He are extractable from the data set as described by the method in Section 3.9.3.

Shown in Fig. 4.19 is the ^{4}He multiplicity measured in our apparatus at beam rapidity for the 4% inclusive centrality bin. A measure of each point is made by fitting the TOFU pulse height spectrum for particles corresponding to beam rapidity ^{4}He utilizing both the linear and non-linear Landau distributions described in Section 3.7. The results for the two fits are similar and overlap within error bars. The Boltzmann temperatures fit to this distribution are $T(y = 3.0 - 3.1) = 199 \pm 3$ MeV and $T(y = 3.1 - 3.2) = 155 \pm 2$ with the non-linear pulse-height fit and $T(y = 3.0 - 3.1) = 194 \pm 8$ MeV and $T(y = 3.1 - 3.2) = 166 \pm 3$ for the linear pulse-height fit.

Similar measurements are also made in the 10-20% centrality region. Although there are more produced ^{4}He at beam rapidity in this region due to the increased number of spectators, the down-scaling of less central collisions results in fewer ^{4}He measured by our experiment in this region. Shown in Fig. 4.20 is the ^{4}He measured by E877 for the 10-20% most central collisions. The yield of ^{4}He is 10-15 times larger in the 10-20% region than in the 4% inclusive centrality, though the transverse spectra temperatures are similar with $T(y = 3.0 - 3.1) = 168 \pm 5$MeV and $T(y = 3.1 - 3.2) = 178 \pm 4$MeV. All points are determined from the non-linear pulse-height fit described in Section 4.4.3.

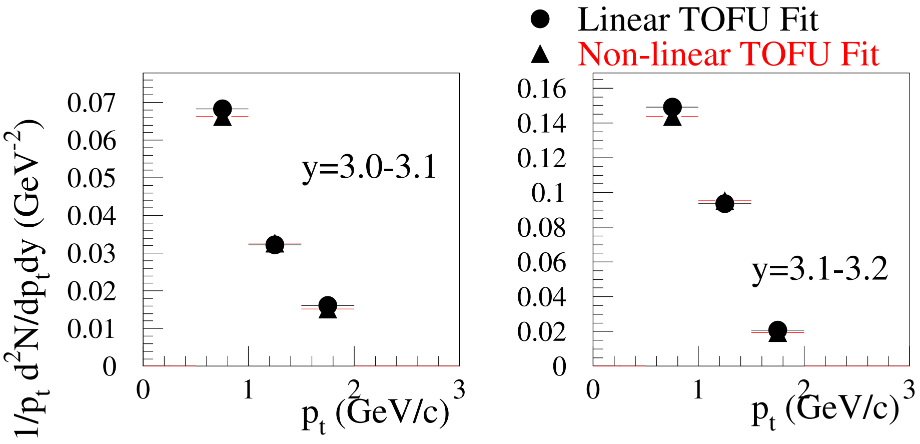

Figure 4.19: The ^{4}He multiplicity in two rapidity bins for the 4% inclusive most central collisions. The yields are determined by fitting the TOFU pulse-height distribution to both a linear and non-linear Landau as described in Section 3.9.3. The results for these two fits overlap within error bars as shown above.

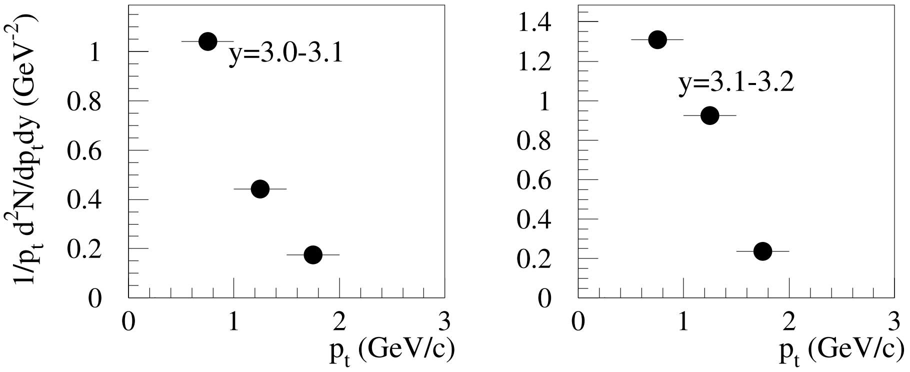

Figure 4.20: The ^{4}He multiplicity in two rapidity bins for the 10-20% most central collisions.

4.5 Summary

In this chapter we have shown multiplicity distributions of light fragments from heavy-ion collisions as measured by E877. Quantitative comparisons were made to other experiments and an excitation function of B_A from Bevalac to SPS energies was compiled. Our measured values of B_A can be qualitatively attributed to an increase in source size at freeze-out and follows the general trend of p-p correlations. Furthermore, light fragments at beam rapidity have been measured for completeness and the deuteron momentum distribution was found to be much wider than that measured at Bevalac energies, implying that the fragmentation mechanism is different between these two energy regimes.

Chapter 5

Model Results

The description of deuteron phase-space distributions is usually considered a second-order phenomena in the sense that first one must describe the proton and neutron distributions at freeze-out within a model before light fragments, via some form of afterburner, can be deduced.

Certain exceptions to this rule do exist, most notably some current day thermal model calculations [40]; however, other descriptions begin with an assumed phase-space distribution of nucleons. While deuteron yields are a second-order effect, we will find that they can be a sensitive parameter for models by discarding those that may describe nucleon distributions but fail with deuterons.

In the following chapter we will discuss various models for describing light fragment production and discuss their robustness. In Section 5.1 two simple models will be discussed, the thermal and analytic matrix models. In Section 5.3 a novel technique for describing source parameter will be outlined which uses a flowing thermal model with a coalescence afterburner. In this technique, the promise of deuterons to describe the volume of the system at freeze-out will be fulfilled and first results of a direct measure of the volume of the system at freeze-out within this model will be produced. In Section 5.4 we will discuss a more complicated cascade model, RQMD in a coalescence framework. Each of these models will aid us in our attempt to comprehend the processes behind fragment production including thermal, volume and collective motion effects.

5.1 Simple Model Calculations

5.1.1 A Thermal Description

To date, several simple models which include thermal distributions with an underlying collective flow have been utilized to describe the source of a heavy-ion collision [18, 76]. In these models it is argued that a high degree of thermalization and hydrodynamic expansion of the fireball region allows such a thermodynamic approach. Therefore particle ratios and spectra can be described analytically within such a model.

Transverse/Longitudinal Spectra

The transverse distribution in such a model is described by a thermal source with a velocity boost dependent on the radius r of freeze-out

$$\beta_r(r) = \beta_s(\frac{r}{R})^{\alpha} \tag{5.1}$$

where R is the radius of the source and β_s is the maximum boost velocity.[1] In this case the transverse spectra can be written as [19]

$$\frac{dN}{m_t dm_t} \propto \int_0^R r dr m_t I_0(\frac{p_t \sinh \rho}{T}) K_1(\frac{m_t \cosh \rho}{T}) \tag{5.2}$$

where $\rho = \tanh^{-1} \beta_r$ and

$$\begin{aligned} K_1 &= \int_0^\infty \cosh y e^{-z \cosh y} dy \\ I_0 &= \frac{1}{2\pi} \int_0^{2\pi} e^{z \cos \phi} d\phi. \end{aligned}$$

As an example of such a fit of the transverse spectra in Si + Pb collisions at the AGS as determined by [18] is shown in Fig. 5.1. Note that the fit is consistent with two choices of (T,β_s) coordinates alluding to a well-known fact of such models that the transverse spectra are consistent with a wide range of (T,β_s) coordinates and are to be highly correlated with one another.

An example of this phenomena is shown in Fig. 5.2 which displays χ^2 contours of fits to the S + Pb and Pb + Pb data from SPS collisions. The relationship between temperature and transverse flow velocity is highly correlated and temperatures as low as 60 MeV would still be consistent with the measured spectra as would temperatures of 150 MeV.

Note that the distributions fit to Eq. 5.2 include an arbitrary constant in the fitted function; that is, the absolute yields of the particle specie are insignificant for such a fitting procedure.

---

[1] The exponent α of Eq. 5.1 is often chosen equal to 2 to be consistent with hydrodynamic results [19].

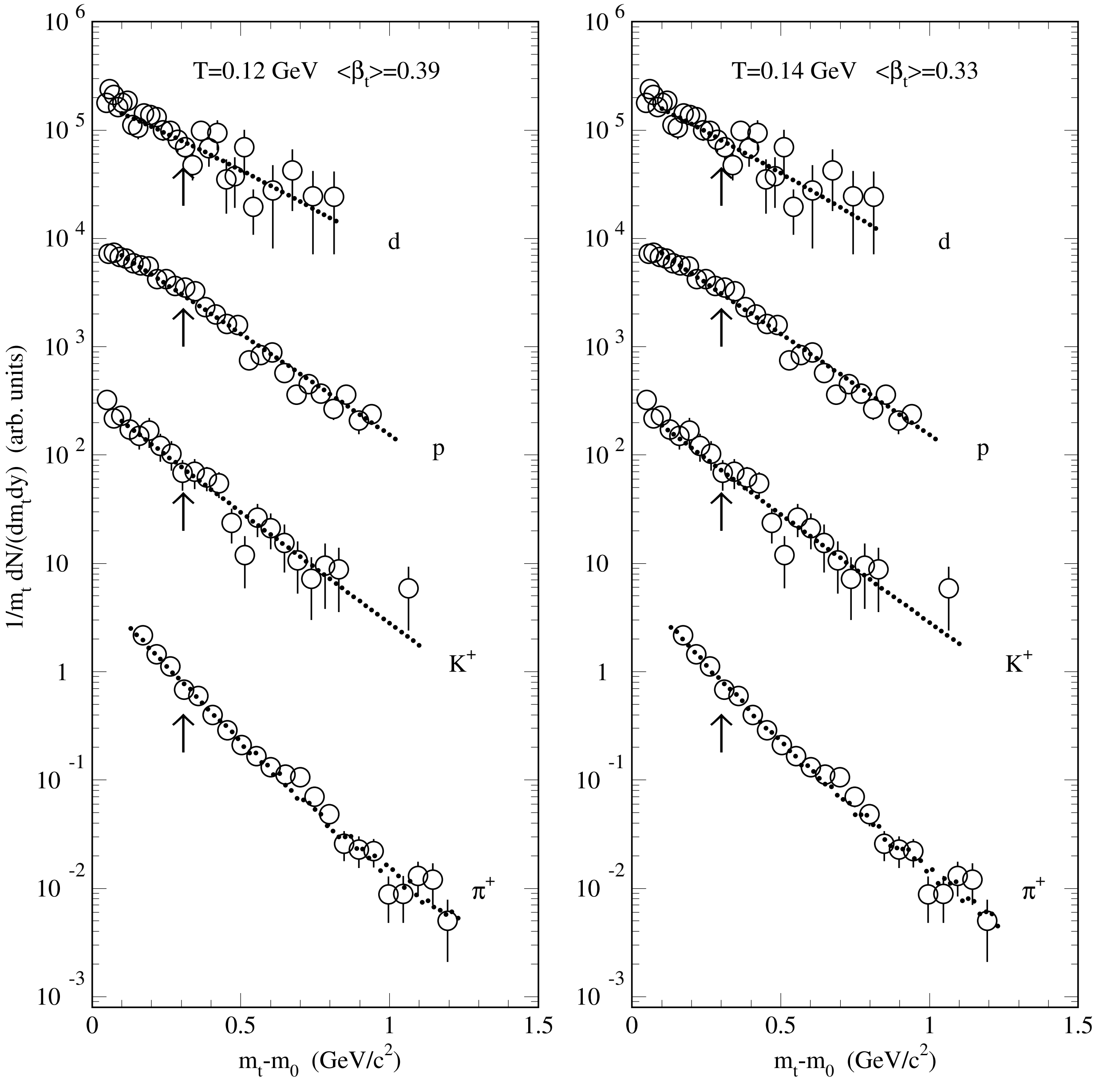

Figure 5.1: Transverse Si + Pb distributions fit to a thermal, transversely flowing model as described in the text. The arrows designate the lowest point that the transverse spectra were fit to in order to remove any low p_t effects. Figure taken from [18].

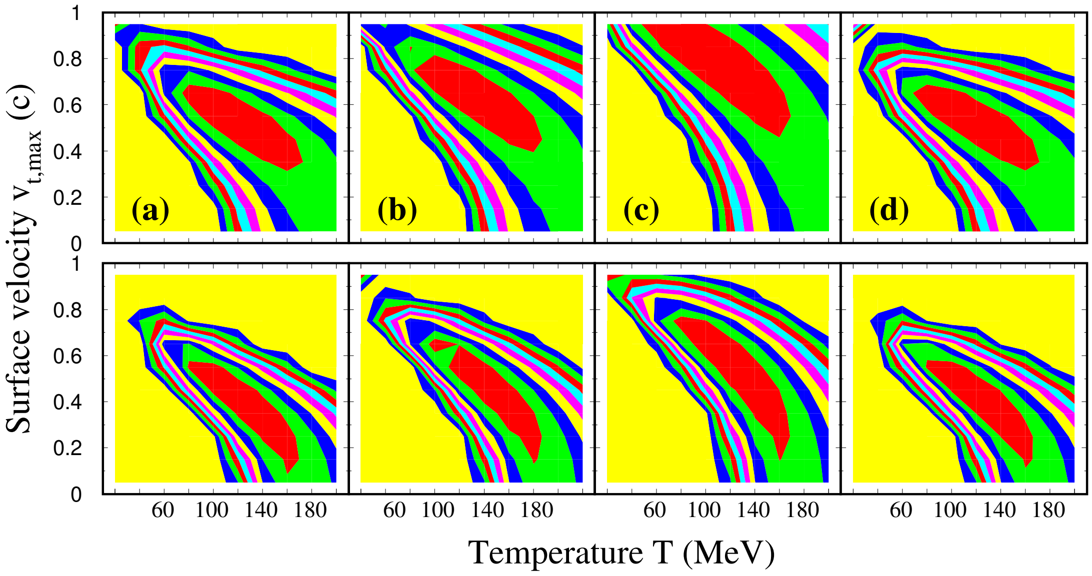

Fig. 2

Figure 5.2: χ^2 fitting maps of β_s vs temperature for Pb + Pb (top panel) and S + S (bottom panel) collisions. The data are fit to a thermal, transversely boosted source as described in the text with suppositions of $\alpha = 1$ (a), $\alpha = 2$ (b), and $\alpha = 3$ (c). Panel (d) is a fit using the RQMD velocity profile. The minimum normalized χ^2 contour corresponds to $1.0 < \chi^2 < 3.0$. Taken from [76].

The longitudinal distribution in this thermal model is described by the superposition of thermal sources over a rapidity interval $[-y_{max}', y_{max}']$ such that

$$\frac{dN}{dy} = \int_{-y_{max}'}^{y_{max}'} dy' \frac{dN_{iso}(y-y')}{dy'} \tag{5.3}$$

where dN_{iso}/dy is an isotropic emitting source

$$\frac{dN}{dy} \propto m^2 T(1 + 2\chi + 2\chi^2) exp(-1/\chi) \tag{5.4}$$

and $\chi = T/(mcosh(y))$.

This model agrees well with the shape of AGS and SPS longitudinal data for Si/Au and S/Pb beam, respectively [18, 40, 56].

Particle Yields

Thermodynamically, the particle yields are given by the grand canonical ensemble of non-interacting fermions and bosons in equilibrium at freeze-out temperature T [18]:

$$\rho_i{}^0 = \frac{g_i}{2\pi^2} \int_0^\infty \frac{p^2 dp}{exp[(E_i - \mu_b B_i - \mu_s S_i)/T] \pm 1} \tag{5.5}$$

where μ_b and μ_s are the baryon and strangeness chemical potentials, g_i is the spin-isospin degeneracy of particle i with total energy E_i, baryon number B_i and strangeness S_i.

Two fundamental differences between this model and the coalescence models described in later sections are present. First, deuteron yields in this model are determined from the grand canonical ensemble and treated similar to produced particles. That is, E_i in Eq. 5.5 reflects the total energy of the deuteron, not its binding energy [41]. The deuteron is therefore considered a produced, not a coalesced, particle. The second difference between this model and the coalescence model described in Section 5.3.1 is that the thermal model assumes that there is local thermal equilibrium; therefore, the collective motion in the system (*i.e.* the "flow") is irrelevant to deuteron yields since, by transforming to a system moving with some overall velocity relative to the center of mass, any such dependencies can be removed. The entire freeze-out volume is then broken into several smaller subsystems in which the physics of deuteron creation is unchanged [41].

While the thermal model has had sufficient successes in describing particle ration in heavy-ion collisions [40, 56], we will not adopt it in this thesis because the thermodynamic parameters are non-trivially related to those used in the flowing, thermal source outlined below. As such, since it will not yield the variables we wish to use to describe heavy-ion collision dynamics with a coalescence mechanism, we will instead select the model described in Section 5.3.1.

However, it should be noted that studies of Au + Au collisions at the AGS with this model [40] have shown that the d/(p+n) ratio is bounded by a system with a temperature between 120 and 140 MeV and baryon chemical potential ($\mu_b = 540\text{MeV}$) to match pion production.

5.1.2 Analytic Descriptions

While an analytic model that accounts for all of the various physics elements present in a relativistic nuclear collision is still forthcoming, and may perpetually be so due to the inherent mathematical difficulties of accounting for all possible processes, several models have been devised [15, 16, 17, 32, 34, 36] which attempt to describe the coalescence of light fragments.

While all simple models deduce an approximate inverse volume dependence of B_2, others have attempted to also account for the finite size of the deuteron. For example, in a density matrix model [36], the coalescence volume can be related to the internal wave-function of the composite particle and the spatial distribution of the nucleons, such that

$$\gamma \frac{d^3N}{dk^3}(Z,N;k) = \left[\frac{4}{3}\pi {p_0}^3\right]^{A-1} (Z!N!)^{-1} \left[\gamma \frac{d^3N_p}{dk^3}\right]^Z \left[\gamma \frac{d^3N_n}{dk^3}\right]^N \tag{5.6}$$

which then, in a semi-classical model which includes the overlapping of proton and neutron wave-functions to coalesce deuterons produces

$$\frac{4}{3}\pi p_0 = \frac{3}{4}(8\pi)^{3/2}[\nu_d\nu/(\nu_d+\nu)]^{3/2}. \tag{5.7}$$

Here the deuteron wave function and proton/neutron spatial distribution are related to ν_d and ν, respectively, via

$$\psi_d(r) = (\nu_d/\pi)^{3/4} exp(-x^2\nu/4) \tag{5.8}$$

and

$$D_p(r) = (\nu/\pi)^{3/2} exp(-\nu r^2). \tag{5.9}$$

The coalescence parameter B_2 in this case can be analytically written as

$$B_2 = (\hbar c)^3 \frac{3m_d}{4{m_p}^2}(8\pi\nu_d\nu/(\nu_d+\nu))^{3/2}. \tag{5.10}$$

Note that, in this model, the coalescence factor B_2 is not simply inversely related to the volume of the source because when the source volume is comparable to the mean radius of the deuteron, B_2 reaches a limiting value. Shown in Fig. 5.3 is B_2 as a function of ν given the value of $\nu_d = .20fm^2$ determined by Sato and Yazaki [36]. As ν increases, which is related to the source size by $R_{rms} = \sqrt{3/2\nu}$, B_2 reaches a limiting value of

$$\lim_{\nu\to\infty} B_2 = (\hbar c)^3 \frac{3m_d}{4{m_p}^2}(8\pi\nu_d)^{3/2} \approx .14GeV^2 \tag{5.11}$$

nearly an order of magnitude larger than any measured value of B_2 from either nucleus or proton collisions.

Shown in Fig. 5.4 is the similar expression of B_3 vs ν:

$$B_3 = (\hbar c)^6 \frac{m_t}{m_p^3}\frac{1}{4}3^{3/2}(4\pi\nu_t\nu/(\nu_t+\nu))^3. \tag{5.12}$$

Again, a limiting value is reached as ν gets large such that

$$\lim_{\nu\to\infty} B_3 = (\hbar c)^6 \frac{m_t}{4{m_p}^3}3^{3/2}(4\pi\nu_t)^3 \approx .024GeV^4 \tag{5.13}$$

when $\nu_t = .36$ [36]. Again, this limiting value is larger than any measured B_t by any proton or nuclear experiment.

These model calculations of Sato and Yazaki provided reasonable values of the freeze-out radius for 400 MeV/nucleon Ne + U collisions, values from 3.7 to

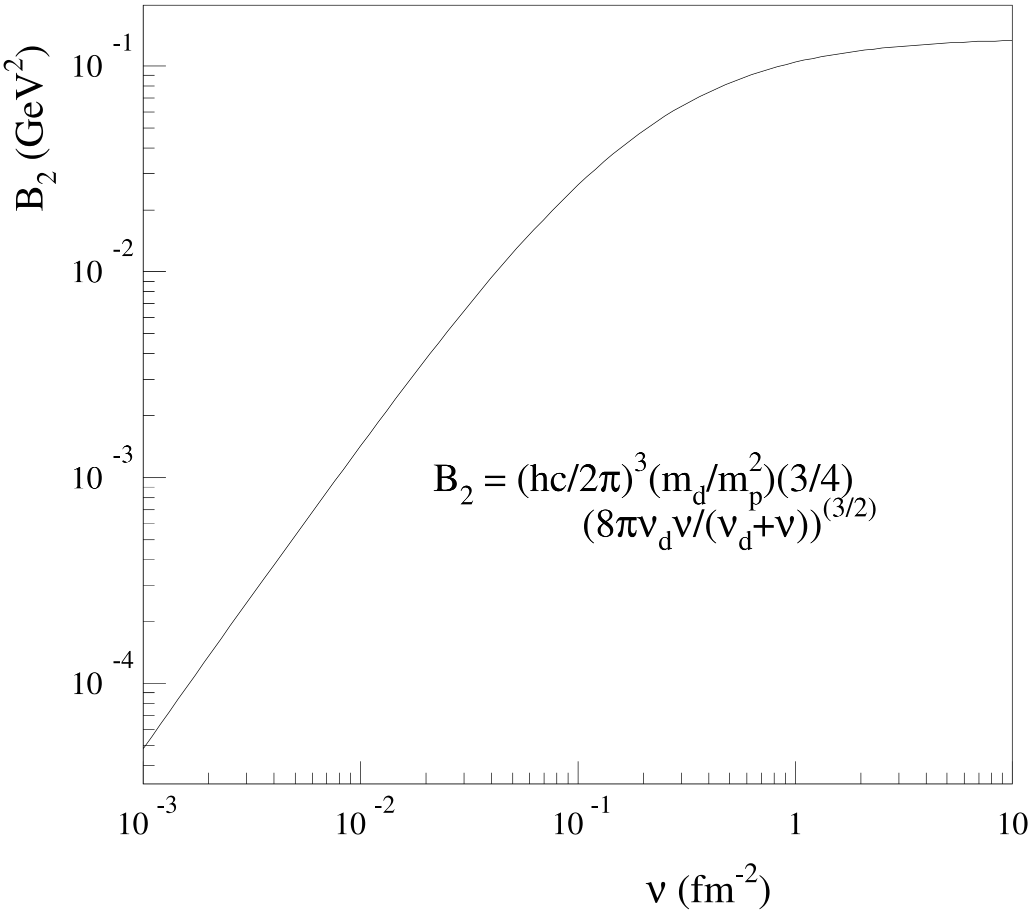

Figure 5.3: B_2 vs $\nu = \frac{3}{2{R_{rms}}^2}$ as calculated in a simple coalescence model by [36].

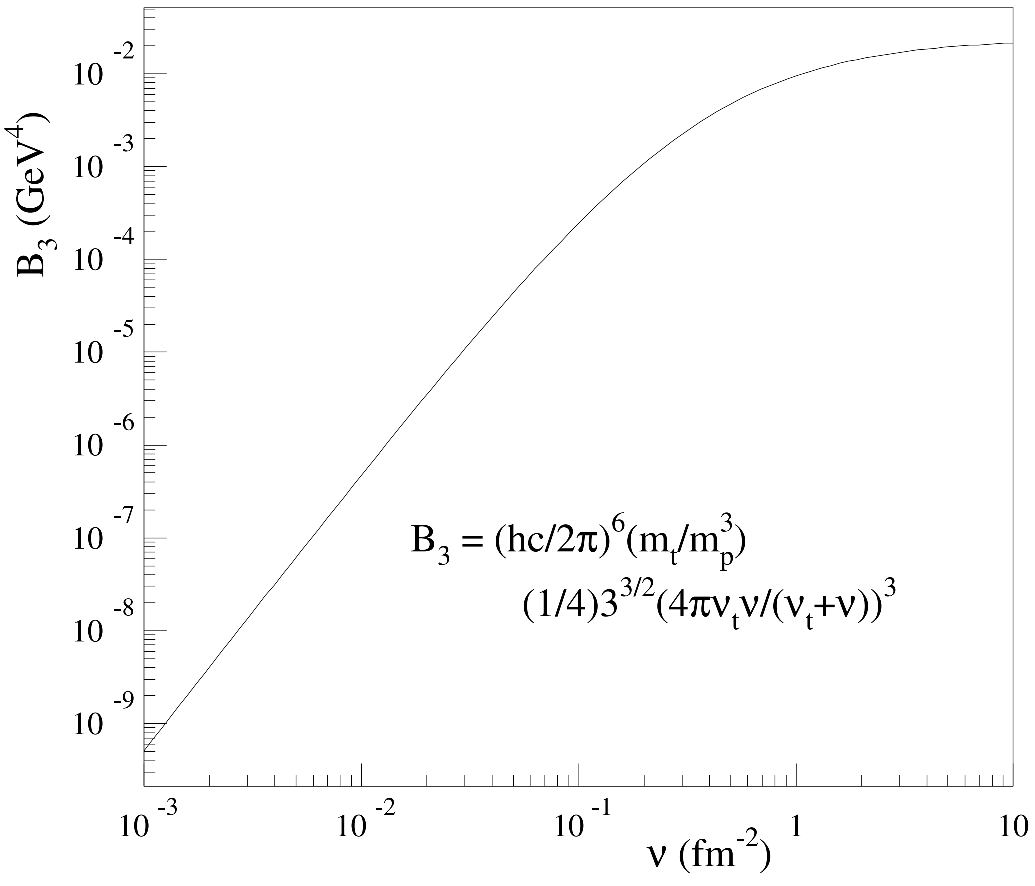

Figure 5.4: Same as Fig. 5.3 for B_3.

4.5 fm. This model, in interpreting our data, however, reveals a fundamental flaw. Given the measured $B_2 \approx 1.5\text{E}{-2}$ GeV^2 and $B_3 \approx 1.0\text{E}{-6}$ GeV^4, results in a ν determined to be $\sim 10^{-2}$, corresponding to a mean radius of $R_{rms} \sim$ 12fm! This result is in obvious disagreement with all other measurements of source size, including boson (π-π [66] and K-K [67]) and fermion p-p [58]) correlations measurements, which produce a value between 4 and 5.5 fm.

The reasons behind the failure of this model to reasonably describe the source at AGS energies must partially be due to the fact that the assumptions regarding the excited source of nucleons include no dynamic correlations. The addition of correlations, as we shall note in Section 5.2.1, can drastically change the yield of light fragments. Therefore, in order to correctly describe the coalescence mechanism we need to step beyond these simple models which leads us to determinations of yields that are not easily expressible through analytic means. Therefore, we will need to step into the arena of Monte Carlo simulations.

5.2 A Coalescence Afterburner

To assess the dependencies of the deuteron distribution from any particular Monte Carlo model, a procedure for coalescing deuterons should be devised which accounts for the coalescing of protons and neutrons into deuterons. To this end, a program to determine coalescence has been constructed by R. Mattiello [69, 79] which utilizes a method applied to bombarding energies from 1 GeV per nucleon in conjunction with the intranuclear cascade model and QMD

[72] as well as at AGS and SPS energies with the cascade models RQMD and ARC [37, 69, 79].

In this model, the number of deuterons is given by a summation over all proton and neutron pairs (i_n, j_p)

$$dN_d = \frac{3}{8} \left\langle \sum_{i_n, j_p} {\rho_d}^W(\mathbf{\Delta x}, \mathbf{\Delta y}) \right\rangle d^3(p_{i_n} + p_{j_p}) \tag{5.14}$$

where ${\rho_d}^W$ is the Wigner density of the Hulthén deuteron wave function and the value of 3/8 derives from spin (3/4) and isospin (1/2) considerations assuming no dynamical correlations in these sectors [30]. Therefore, by simply projecting the classical neutron/proton distribution on the deuteron wave-function via this Wigner method, we may determine the distribution of deuterons in phase-space given any particular source of nucleons

Note that the model does not include a third body for the coalescence of deuterons as described in Section 1.4.1, and therefore does not account for the precise mechanism for coalescing a proton and neutron since such a process requires a third body. However, as was alluded to in Section 1.4.1, this may be phenomenologically compensated by the presence of the hadronic source which acts as a large third body.

This model in future sections will be used to deduce deuteron distributions from various non-trivial models. However, we will adopt it now for some preliminary studies of light fragment formation.

First, in order to study the dependence of B_2 on the volume of a system at freeze-out, we have taken a simple model of one proton and neutron freezing out within some Gaussian radius R. The transverse distribution of the nucleons is taken to be a Boltzmann with a temperature of 150 MeV and the rapidity distribution is chosen to be similar to that measured by experiments at AGS, a Gaussian with $\sigma = 1.1$. Shown in Fig. 5.5 are the results of B_2, evaluated at mid-rapidity for a variety of different freeze-out radii. Plotted on the x-axis is $1/r^3$ which is proportional to the inverse volume of the system at freeze-out. Notice that, depending on the volume, the value of B_2 can vary by an order of magnitude. However, B_2 approaches the value of $\sim 10^{-2}$ (GeV^{-2}) as $V \rightarrow 0$, coinciding with the measured value for all pp and pA experiments and those AA experiments at Bevalac energies. The fact that the value of B_2 for this model approaches the limiting value measured by experiment emboldens us in our use of the coalescing program for the calculations of deuteron yields though this simple fact in and of itself does not endorse such a model. Furthermore, the qualitative trend of B_2 follows the arguments set forth in Section 1.4.1 where the deviation from the limiting value of B_2 near 10^{-2} is attributed to the expansion of the hadronic source beyond the mean radius of the deuteron.

As a further study of this model, the effects of volume and density on the value of B_2 is calculated for a large number of nucleons. Shown in Fig. 5.6 are the results of a Monte Carlo calculation with a Gaussian source of 150 protons and neutrons, similar to the number in a single Au + Au collision, evaluated for several different source volumes at freeze-out. The Boltzmann temperature is 150 MeV and the Gaussian rapidity distribution is $\sigma = 1.1$. An inverse volume dependence of B_2 is clearly manifest.

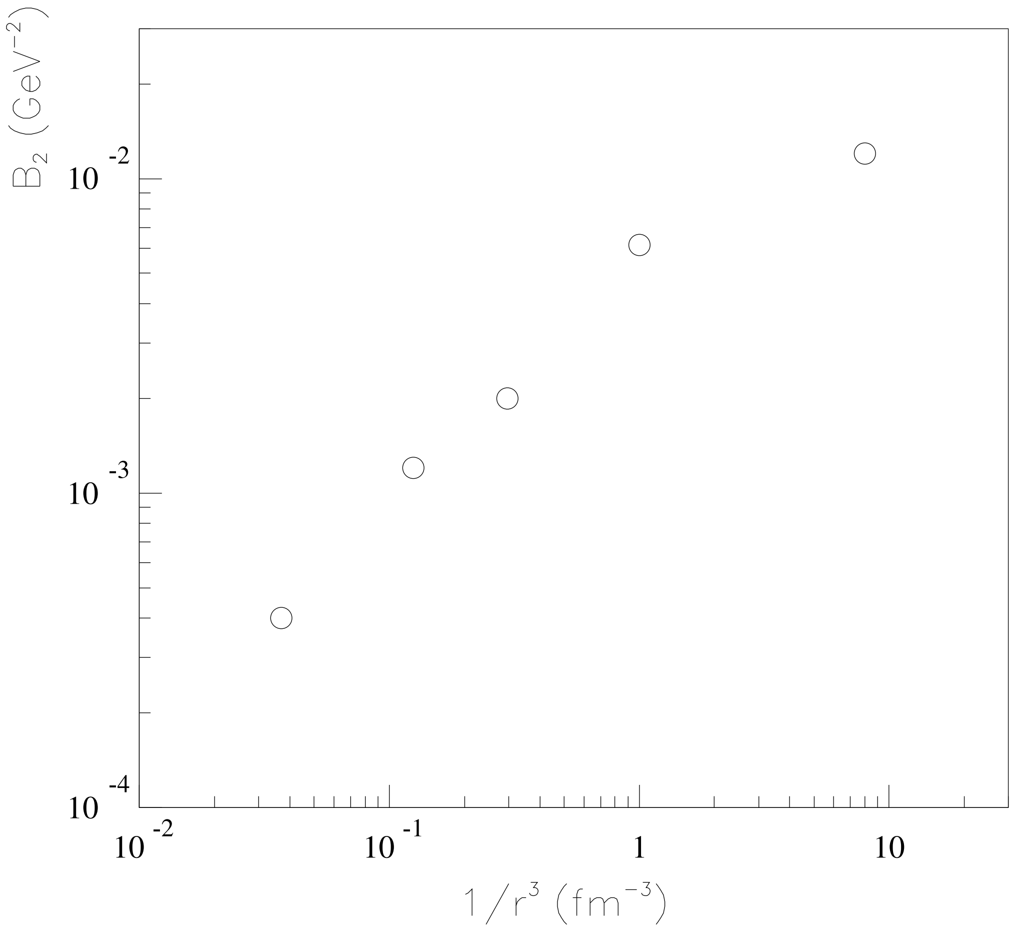

Figure 5.5: B_2 determined via a source of one proton and one neutron that freeze-out within a Gaussian source of radius r versus $1/r^3 \propto 1/V$.

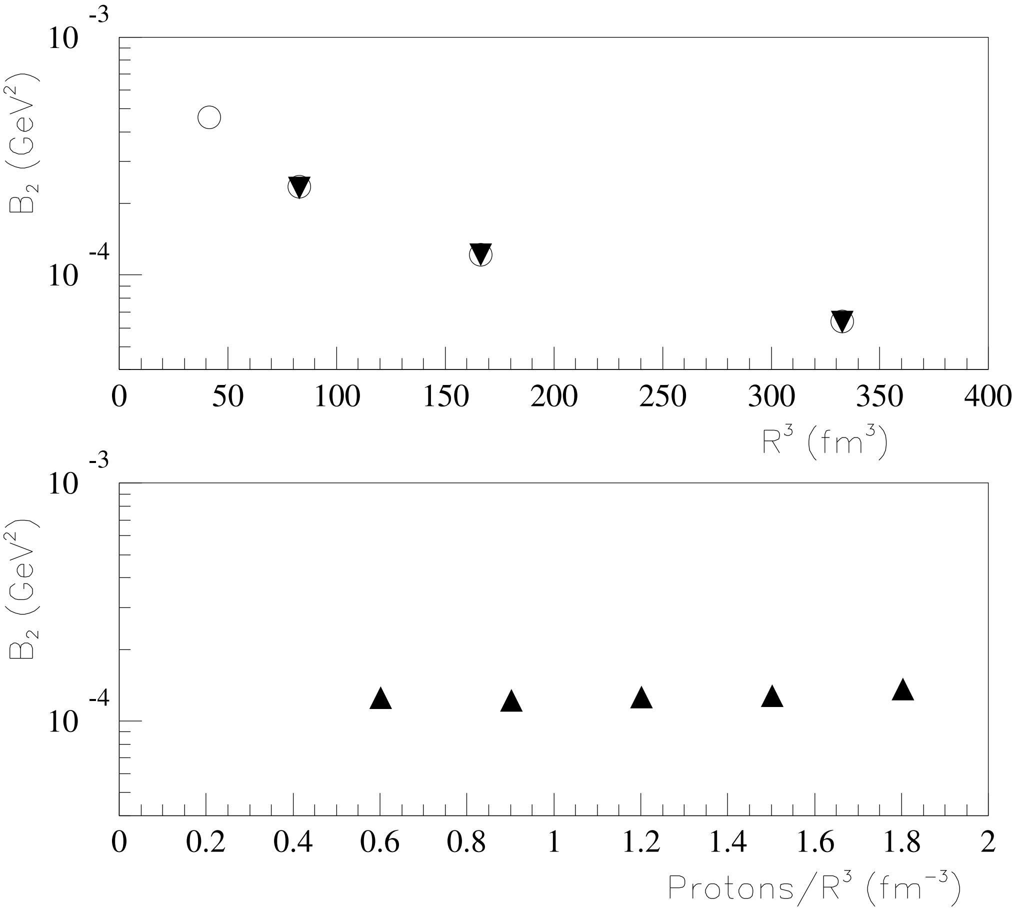

Figure 5.6: B_2 for various freeze-out scenarios in a simple thermal model. The top plot displays B_2 as a function of r^3 for a Gaussian,thermal source. The circles are for systems in which only r is changed, keeping the number of protons and neutrons the same. The upside-down triangles are for systems where the number of protons and neutrons are also changed such that the density at freeze-out is the same. The bottom plot displays B_2 as a function of the density at freeze-out for the case of 150 protons and neutrons.

Without further demonstration, one could argue that B_2 is not inversely proportional to the volume at freeze-out, but is instead proportional to the density. Such an argument appears to be intuitive; however, the construction of B_2 is such that the number of nucleons is divided out, that is B_2 is constructed to only be dependent on volume.

To demonstrate this fact, when the number of protons and neutrons is changed concurrent with the volume change such that the density is constant (the upside-down triangles in Fig. 5.6), there is no difference in the B_2 parameter. Furthermore, in Fig. 5.6 are displayed the results of a final calculation where the density of the system at freeze-out is changed, keeping the number of protons and neutrons the same. As is clearly shown, B_2 is independent of density over a wide range demonstrating that B_2 must be inversely dependent on the volume of the source at freeze-out for a simple thermal model.

Note that from Fig. 5.6 we can also determine the approximate thermal source size needed to describe the data in our collisions. The freeze-out Gaussian measured by E877 in correlation studies [58, 66, 67] is approximately 5.0 fm, which is a lower limit on a reasonable source size because identical particle correlations, by their nature, sample a smaller region of the source due to position-momentum correlations in the source [13]. The value of $R = 5.0$fm would produce a value of B_2 an order of magnitude smaller than the measured value. Therefore, in this simple thermal model, one would require a freeze-out volume 1/10 of 5.0, that is a freeze-out Gaussian radius of ~ 2.5 fm, significantly smaller than the radius of a Au nucleus (3.0 fm) and any conceivable freeze-out radius.

Therefore, we conclude that though a simple thermal Gaussian source may agree with the naive concept of B_2 as inversely proportional to volume, there are obvious deficiencies in this model. We will find, in the following sections, that one of these deficiencies is collective effects and position-momentum correlations.

5.2.1 Flow vs Volume

If you come to a fork in the road, take it. [Yogi Berra]

We have shown in the previous section that, in a thermal random source with a Gaussian freeze-out position profile, B_2 is approximately inversely proportional to the volume of the system at freeze-out. Therefore, given a variety of systems, comparisons of freeze-out volumes can be qualitatively performed simply from the relative ratios of B_2. However, a heavy ion collision does not freeze out according to such simple models and, therefore, is not easily interpretable in terms of a freeze-out volume. This is quickly demonstrated from the fact that the source size required to describe the measured deuterons would be greater than 10fm (see Section 5.1.2), six times the volume derived from correlations of pions [66] and protons [58] in the same collisions.

Shown in Fig. 5.7 are sample freeze-out variables determined by the cascade code RQMD. Note that not only do position-momentum correlations exist, but so do time-position, position-position, and momentum-momentum correlations. Any correlations which exist in the source will tend to drive the resulting deuteron distributions away from the standard thermal results described above. This can be understood qualitatively by considering the coalescence phenomenological model which requires a proton and neutron to be in a certain region of phase-space in order to produce a deuteron. A source with a correlation in position-momentum space implies that if two nucleons are within a certain region of position space from one another, than their relative momentum is restricted as well. In the most extreme case this implies that instead of requiring that two nuclei are within a certain $\Delta x \Delta p$ of one another, we need only require that they are within a certain Δx, as this necessarily implies that any momentum restriction is satisfied.

For example, R. Mattiello *et al.* [69] determined the distribution of deuterons at mid rapidity utilizing RQMD v1.08. In order to obtain a qualitative understanding of the change in the deuteron yields due to position-momentum correlations, the momenta and positions of the protons and neutrons at freeze-out were randomly redistributed and fed into the coalescence afterburner as well. Shown in Fig. 5.8 are their results both for the original deuteron distribution and that without correlations, which they designate as “without flow”. Note that the invariant cross-section for these two cases vary by a factor of 4 from one another, suggesting that the deuteron yield is governed more by the correlations between position and momentum in our collisions than by simple volume, which only accounts for a fraction of the invariant cross-section.

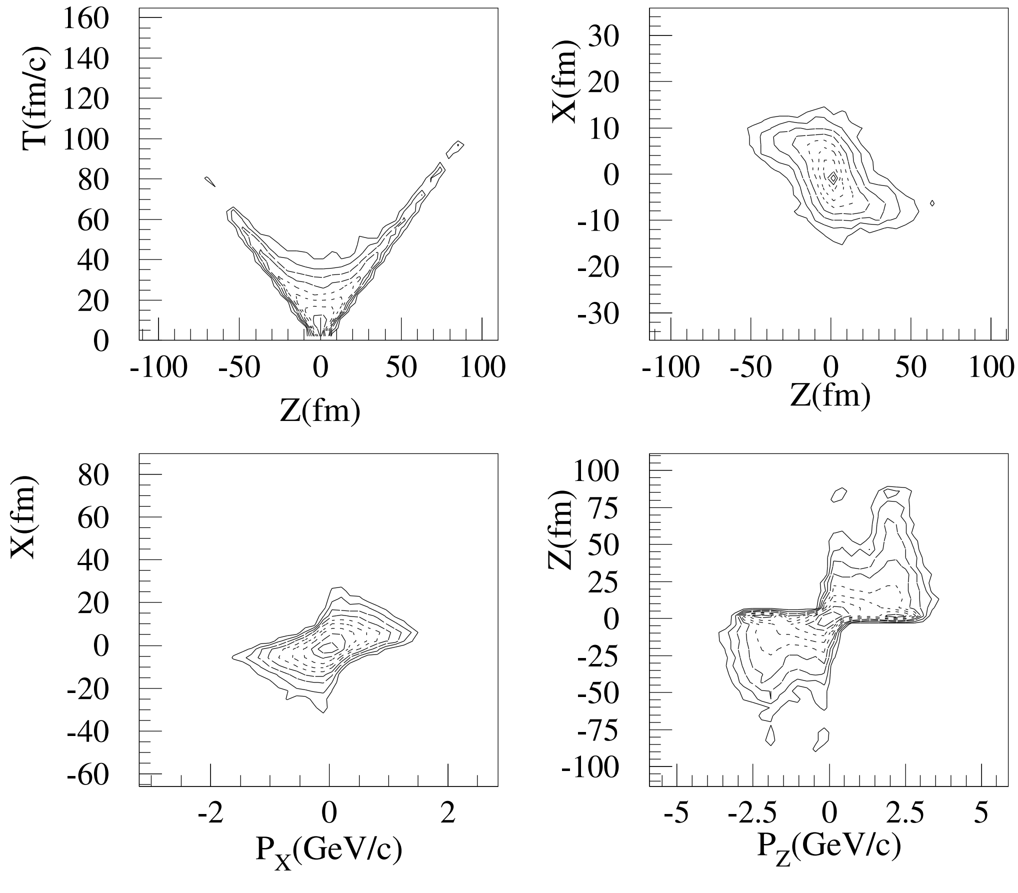

Figure 5.7: Freeze-out distributions for all particles as determined from RQMD 2.3.

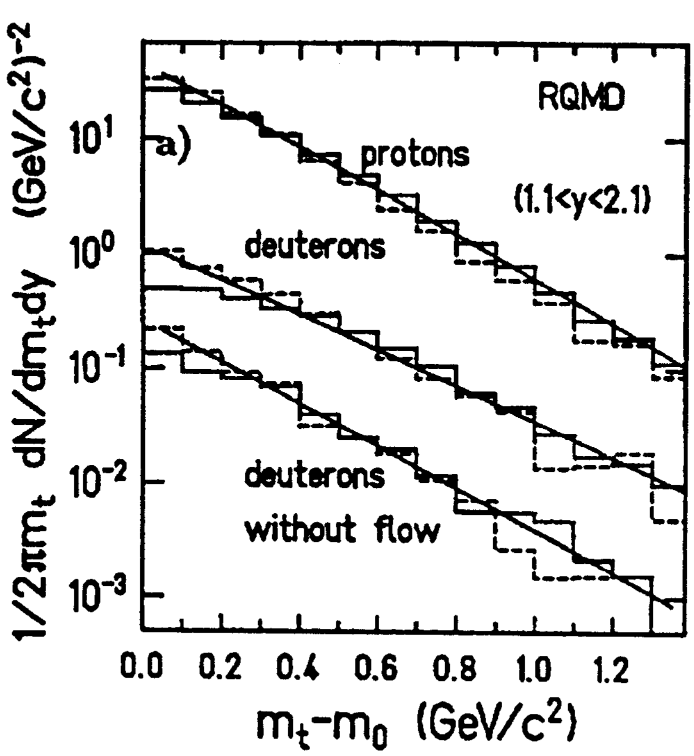

Figure 5.8: Prediction of the invariant transverse mass spectra of protons and deuterons for Au(11.6 A GeV)Au collisions at mid-rapidity ($1.1 < y < 2.1$) for central collisions ($b < 3fm$). The deuterons are calculated both normally and with the position and momentum of the particles randomly redistributed, corresponding to "without flow". Furthermore, the calculation was performed both with (solid line) and without (dashed line) mean-field potentials. Figure taken from [69].

5.3 Deuterons as a Model Constraint

As was shown in Section 5.1 particle spectra can be fit to a thermal distribution that includes underlying transverse and longitudinal boost velocities. This technique restricts the *shape* of the spectra but does not restrict the yield.

As was shown in Section 5.2.1 the *yields* of deuterons are highly sensitive to the degree of collective motion in the nucleon source. Therefore, instead of fitting with an overall normalizing constant to each spectra, the deuteron/proton ratio can be utilized as an extra, perhaps very sensitive, constraint in the fitting procedure.

The conceptual jump to including deuterons, however, is non-trivial due to the fact that the above model says nothing about the relative freeze-out distances of particles, a necessary component for determining deuteron yields. As such, though the yield of deuterons will become an extra constraining parameter, we now must include other fitting parameters beyond T and β_s, including the freeze-out position and time distributions. In the end we will find that deuteron yields will still be a more sensitive constraint to model calculations than found previously.

5.3.1 A Flowing Thermal Model

With the intent of describing the mechanism of a relativistic heavy-ion collision, several models have been devised. Among them are giant cascade models, including RQMD [68], ARC [37] and ART [73], and smaller, phenomenological models. The benefit of the larger cascade models is that a large number of mechanisms can be explicitly employed in the code. However, interpretations of such results are easily shrouded by the number of parameters needed to produce the code. As such, the simple fact that the output of the code describes the data does not necessarily imply that the code assumes the correct dynamic mechanisms. On the other hand, simple models are often used to describe heavy ion data with as few parameters as possible. These models benefit from simple phenomenological interpretation, though the physics behind such an interpretation may be lost in the simplistic assumptions.

In Section 5.4 the results of nucleons and deuterons from a cascade code will be discussed; in this section a simpler model, devised by S. Chapman, J.R. Nix, and U. Heinz [74] will be implemented to describe the nucleon source. This model uses an emission function (S) for a finite expanding thermalized source where

$$E_K \frac{d^3N}{d^3K} = \int d^4x S(x,K). \tag{5.15}$$

The source includes longitudinal and transverse collective motion with an underlying temperature, given by

$$S(x,K) = \frac{M_t \cosh(\eta - Y)}{(2\pi)^{7/2}\Delta\tau} exp\left[-\frac{K\cdot u(x)}{T} - \frac{(\tau-\tau_0)^2}{2(\Delta\tau)^2} - \frac{r^2}{2R^2} - \frac{(\eta-\eta_0)^2}{2(\Delta\eta)^2}\right] \tag{5.16}$$

where

$$\eta = \frac{1}{2} ln[(t+z)/(t-z)]$$

$$\begin{aligned}
\tau &= \sqrt{(t^2 - z^2)} \\
Y &= \frac{1}{2} ln[(1+\beta_l)/(1-\beta_l)] \\
K \cdot u(x) &= M_t \cosh(\eta - Y)\cosh\eta_t(r) - K_t \frac{x}{r} \sinh\eta_t(r) \\
\eta_t(r) &= \eta_f(r/R).
\end{aligned}$$

This model has most recently been used to glean information from pion correlation studies [75] but we will apply it here to gain insight into the physics of light fragment production.

Fig. 5.9 shows sample distributions in this model of position, momentum, and time variables. Note that there is a direct correlation between position and momentum in the beam (z) direction as well as a t vs z distribution that follows the theoretical expectation of a simple Bjorken model.

The primary new methodological result of this work is to use a parametrized source, such as the one given above, with a coalescence afterburner that forms deuterons from the proton and neutron distributions. Since deuterons are sensitive to collective effects in the source they can be used as a further constraint to thermal, flowing models which have, to date, left a large region of phase space available for describing the data. (See Section 5.1.)

Shown in Fig. 5.10 is an example of proton and deuteron spectra from the source function with measured protons from E877 [47] and E866 [63] overlaid. The parameters used to describe the protons in this plot are: $T = 110\text{MeV}$, $R = 5.5\text{fm}$, $\eta_f = .53$, $\Delta\eta = .73$, $\tau_0 = 3\text{fm}$ and $\Delta\tau = 1\text{fm}$. Notice that both the proton dN/dy and transverse spectra at mid-rapidity can be described by these parameters. The proton spectra can, in fact, be described by any

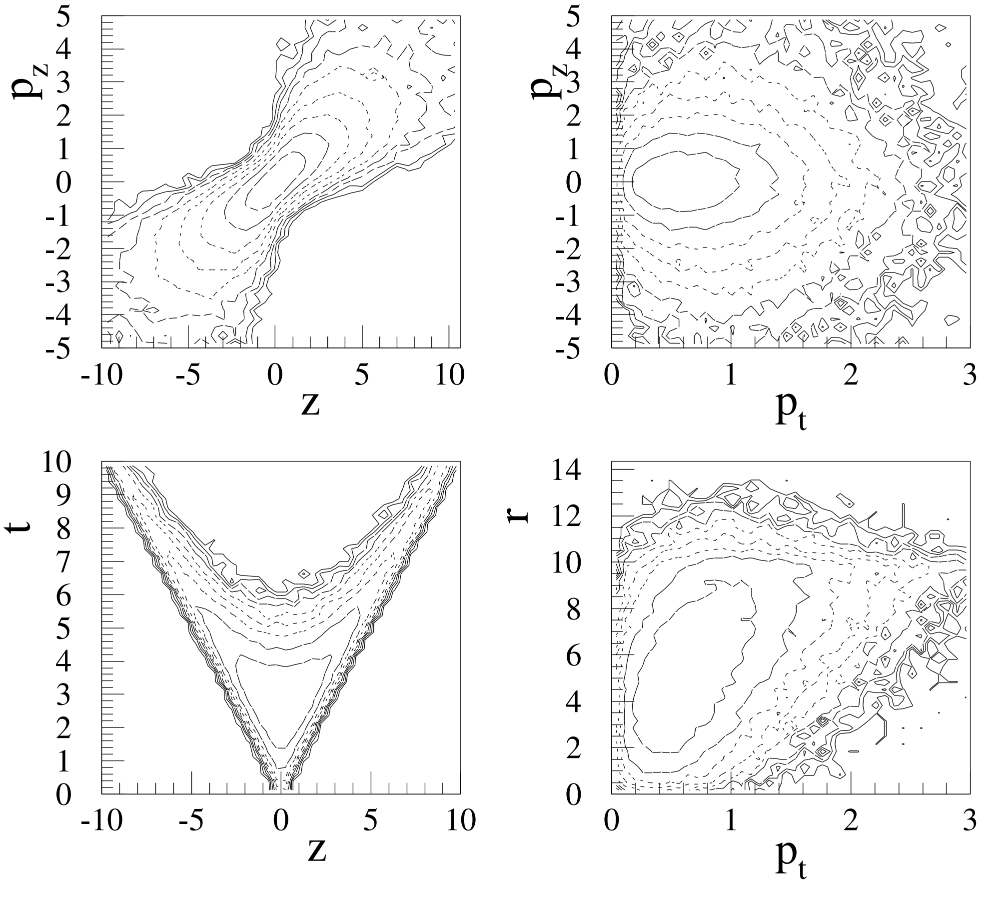

Figure 5.9: Correlations between variables in the flowing thermal model of [75].

reasonable combination of T, R, τ, and τ_0 provided that η and $\Delta\eta$ are varied accordingly in order to fit the transverse and longitudinal spectra respectively.

Also shown in Fig. 5.10 are the deuterons that would be produced from such a distribution of protons along with the measured deuterons at mid-rapidity with 10% systematic error bars; the statistical error bars in this region are smaller than the points. Note that the deuteron invariant spectra are over-predicted for this particular set of parameters implying that either the collective motion ($\eta_f/\Delta\eta$) has been overestimated or the radius R has been underestimated. As a change in the collective motion variables will, de facto, change the temperature of the system since the proton spectra are a constraint on these variables, the (T,R) space can be probed with respect to deuteron yields.

The technique used here for mapping out the χ^2 space of this model is as follows:

- An initial T and R are chosen
- From the assumption of T and R, η_f and $\Delta\eta$ are uniquely determined from the transverse and longitudinal proton spectra, respectively. The model is therefore fit with these two parameter to the proton spectra.
- After the proton distribution is determined, the deuteron yields are calculated with the coalescence afterburner described above.

We will assume that $\tau_0 = 3$fm and $\Delta\tau = 1$fm, producing a time distribution that is similar to RQMD results.

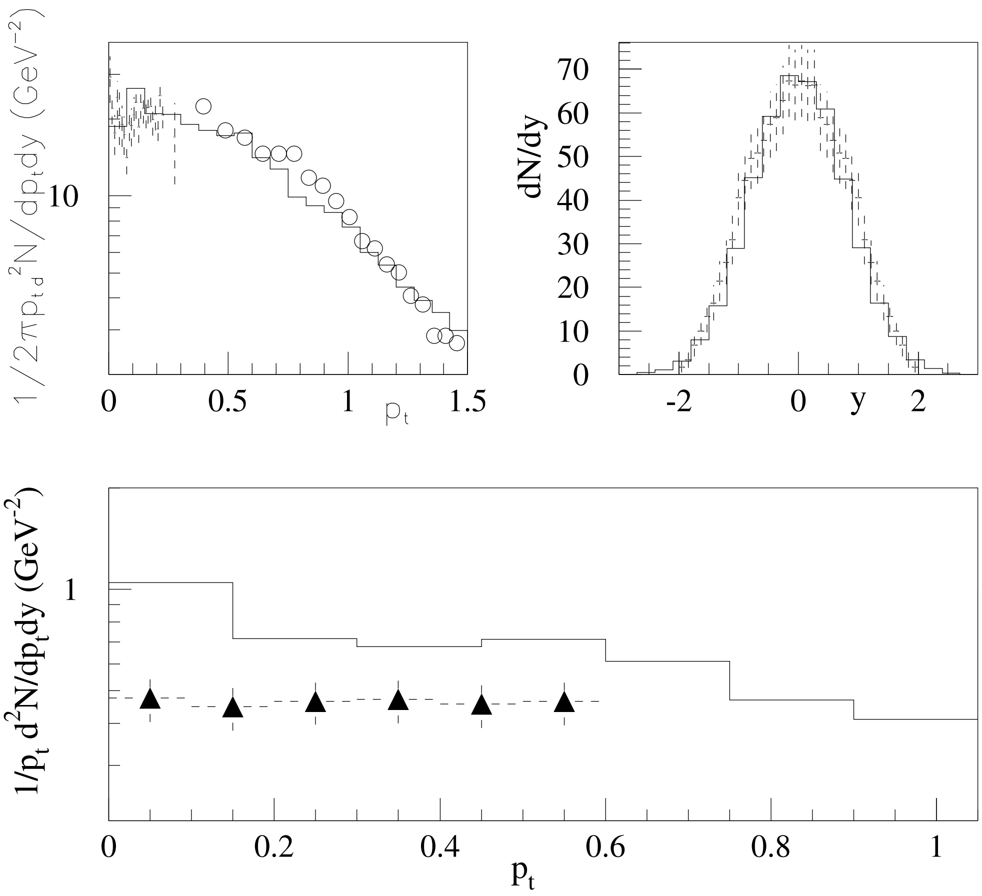

Figure 5.10: The source distribution of protons and deuterons compared with measurements. The source results are the solid lines. The proton transverse spectra are from E877 [47] at low p_t and E866 at high p_t [63] and the dN/dy distribution is calculated from both experiments [47]. The bottom plot is the calculated deuteron multiplicity distribution at mid-rapidity compared with the experimental measurements. The statistical errors for the deuteron measurements are smaller than the triangles and the overall 10% systematic error bars are shown.

As each of these calculations for one particular choice of T and R consumes a large amount of CPU time[2], a program which mapped out the entire χ^2 space of all of these parameters is beyond the scope of this thesis. We will instead introduce this technique and provide the first results of this system, outlining its strengths and weaknesses.

Shown in Fig. 5.11 is the distribution of the normalized χ^2 with respect to the measured deuterons calculated as a function of T and R. For each temperature, a number of Gaussian radii were chosen in 1fm intervals in order to find the minimum and map out a crude χ^2 space. The figure shows a clear minimum between R = 6 and 8 fm and T = 110 and 190 MeV and a possible second minimum near R = 4.5 fm, T = 190 MeV.

Any temperature between 110 MeV and 230 MeV is consistent with reasonable values of the transverse radius as correlation measurements by E877 [66] have resulted in transverse Gaussian radii between 4 and 5.5 fm. Viable options of temperature, however, are constrained by the pion transverse spectra. Since the pion spectra have a Boltzmann distribution near T = 150 MeV, any model which begins with an underlying temperature greater than 150 MeV will be inconsistent with pion measurements. For these reasons the minimum near T = 130 MeV and R = 7 fm is fit to an assymetric parabolic distribution in order to extract the minimum and 1σ error bars.[3] Since the χ^2 distribu-

---

[2] On the current SGI Challenge system, approximately 12 to 32 hours of CPU time is needed for each iteration of T and R.

[3] A correlation between T and R, although expected to be present in the results, was not determined in this analysis due to the limited number of data points

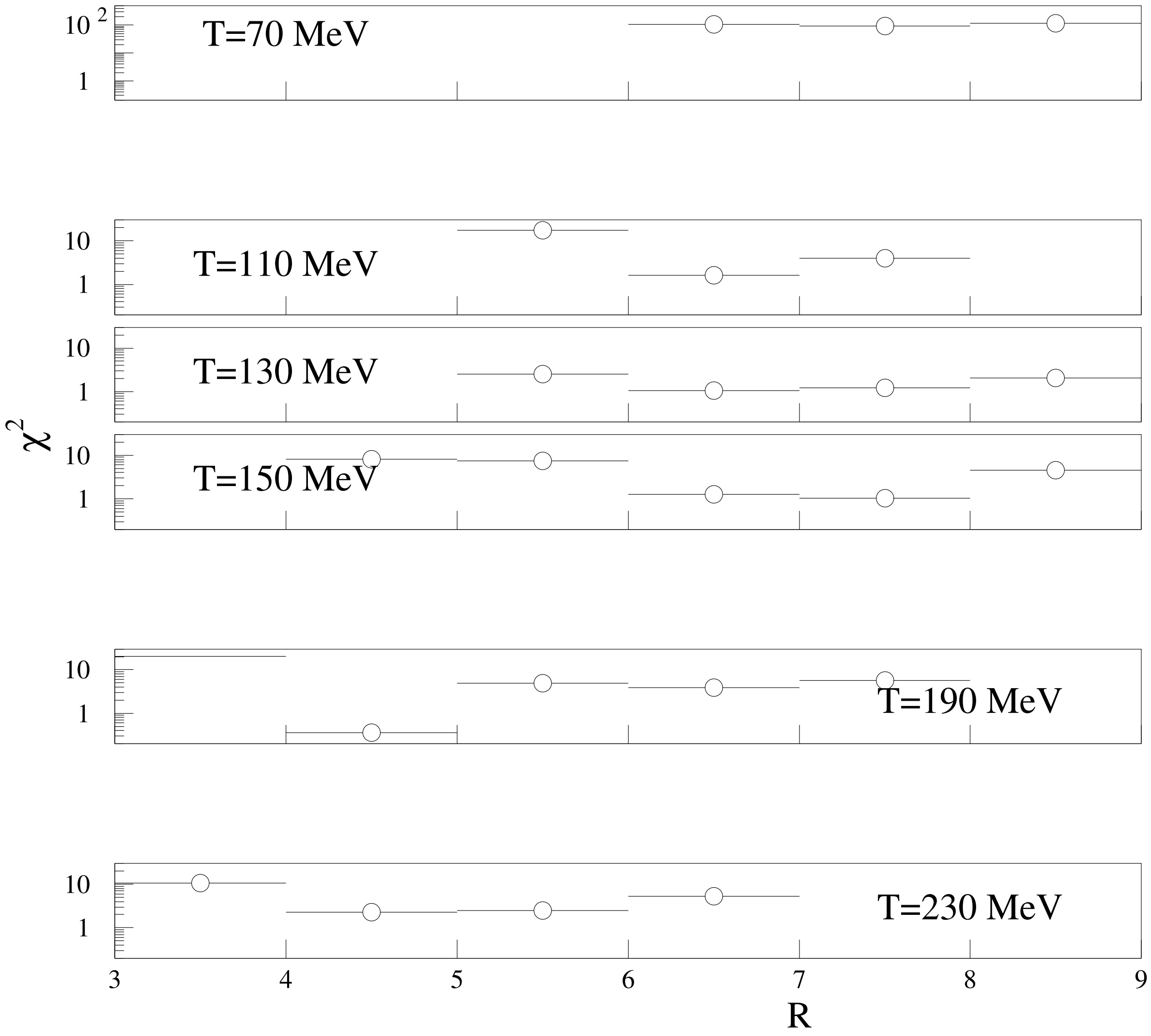

Figure 5.11: χ^2 map fit to a flowing thermal model as a function of R for a variety of choices of T. Spaces between plots are purposefully made in order to keep a ΔT of 20 MeV in the presentation of results.

tion is decidedly assymetric versus T and R the extra terms $A(R - R_s)$ and $B(T - T_s)$ are added to account for this assymetry. A fit to this distribution gives

$$\begin{aligned} R &= 6.5^{+1.7}_{-.4} fm \\ T &= 137^{+38}_{-12} MeV \end{aligned}$$

Note that this extraction of source attributes has been a promise of deuteron formation that has remained unfulfilled at AGS energies. However, from the parametrization of the source given above, these attributes can be extracted for each entrance channel, as a function of beam energy and colliding system.

The extracted radii of $R = 6.5^{+1.7}_{-.4}$fm is larger than that deduced from pion correlations [66] between 4.0 and 6.0 fm, though consistent within 3σ. Measurements of the source size from pion correlations are plagued by interpretations of the source, and it is generally believed that radii gleaned from pion correlations are simply a lower bound on the transverse radius [75]. The transverse radius of RQMD, a cascade model which includes collision dynamics and cross-sections, at mid-rapidity is near 5.9 fm, 2.0σ from the radius deduced from these flowing, thermal model calculations.

Finally, while models which deduce transverse radii from the deuteron multiplicity have been numerous, this model even more strongly constrains

---

available.

the temperature of the system at freeze-out and dramatically agrees with predictions of thermal models [40] which place the freeze-out temperature between 120 and 140 MeV.

While this technique has been shown to extract reasonable source parameters at mid-rapidity from proton and deuteron distributions, several drawbacks exist. First, the computational time that is required for such a calculation currently borders on unreasonable for the complete mapping of the T, R, τ_0, $\Delta\tau$ space. Optimizations of the code and search space could reduce this computational task to a few months.

Even should computational time cease to be a factor, however, a second deficiency of this model is that the source parametrization given above fails to simultaneously describe protons at mid-rapidity and 1 unit away. This fact can be trivially deduced by noting that the source function does not include a mechanism for producing a y dependence of the temperature parameter, a well known attribute of the proton spectra in our collisions [47]. As this model fails away from mid-rapidity, the results quoted above must be deemed preliminary, pending a full model of the source which can account for all such phenomena of single particle spectra. To date, no such simple parametrization has been devised.

5.4 Comparisons to the Cascade Model RQMD

> *If you don't know how to do something, you don't know how to do it with a computer.* [Anonymous]

In order to describe nucleus-nucleus collisions, several cascade codes have been developed: ARC, ART, RQMD, and others. In these codes, the creators attempt to describe the processes involved in heavy-ion collisions, including resonances, medium effects, and other phenomena. Individual physicists can then compare their measured data with the predictions of these codes and, hopefully, in the process determine which physics processes are necessary. In this fashion a coherent picture of these collisions can be formulated. To date the cascade codes have been fairly successful at describing general features of heavy-ion collisions including pion and proton multiplicities and rapidity distributions as well as flow results.

RQMD (Relativistic Quantum Molecular Dynamics) [68] is based on the propagation of all hadrons on classical trajectories in the framework of Hamilton constraint dynamics. The model includes string and resonance excitation, a finite formation time for produced particles, rescattering of secondaries and modified dispersion relations for baryons. While it does not incorporate light fragments explicitly, a coalescence afterburner has been devised which takes the distribution of protons and neutrons at freeze-out and forms deuterons out of those pairs that are close enough in phase space. Such a model has been developed by R. Mattiello [69] and has been described above in Section 5.2.

In the most recent publication of RQMD on fragments [69], a prediction of light fragment invariant spectra from Au + Au collisions at mid-rapidity was presented. This figure is reproduced in Fig. 5.12 along with the spectra measured in this thesis. The dotted line corresponds to RQMD calculations in cascade mode and the dashed line corresponds to the same code in mean-field mode in which effective baryon masses in medium are incorporated to show the effect on light clusters. The measured proton and deuteron distributions at mid-rapidity agree with the predictions of the mean-field results and rule-out the simple cascade results. The measured ^{3}H/^{3}He spectra, clearly a third order calculation, are consistently higher than the predictions of mean-field RQMD results, though the systematic error bars ($\sim$17%) are nearly sufficient to account for this difference.

Since this publication, the RQMD code has passed through several versions, the most recent of which is version 2.3. The same code of Mattiello [69] devised in [69] for coalescing fragments was employed on RQMD 2.3 for further results in this thesis. This newer version of RQMD differs from v1.08 most significantly in that version 2.3 changes the angular distribution of binary collisions such that more particles are emitted forward and backward of mid rapidity; version 1.08 produced more of an isotropic redistribution of particles.

Shown in Fig. 5.13 are the results of the proton invariant cross-section for the 4% most central collisions for RQMD in both cascade and mean-field mode overlaid with the measured proton spectra [47]. Note that the RQMD mean-field results agree with our measured protons near mid-rapidity and at low transverse momentum. However, the calculations deviate from the measured protons the closer one gets to beam-rapidity.

Shown in Fig. 5.14 are the results of deuterons in cascade and mean field calculations as a function of p_t and y. Again, we find that at mid-rapidity the calculations fairly represents the data though from y = 1.9 to beam rapidity RQMD results do not describe the yield nor the shape of the deuteron spectra.

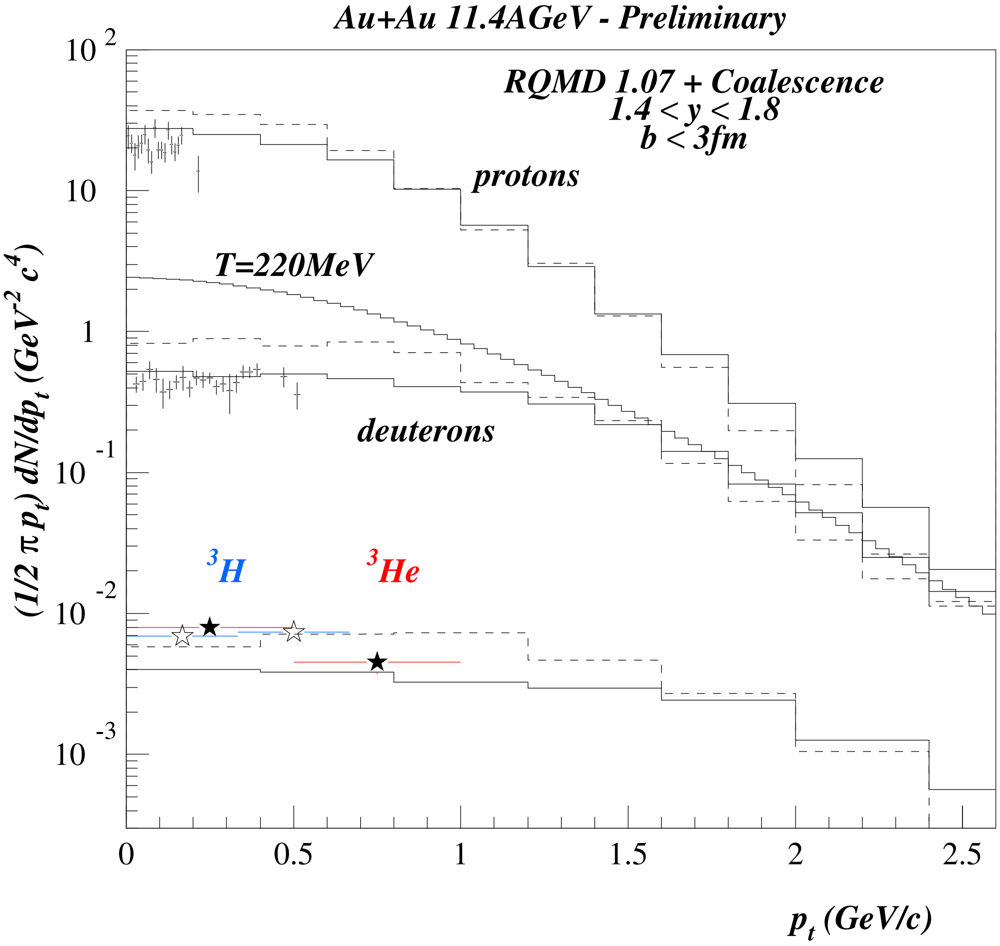

Figure 5.12: Measured Proton and Light Fragment invariant spectra at mid-rapidity compared to calculation of RQMD 1.08. The dotted (dashed) line corresponds to RQMD calculations in cascade (mean-field) mode. A fit of a thermal distribution to the tail of the deuteron distribution show that it is consistent with T = 220 MeV and inconsistent with deuterons at lower p_t. Measured protons and deuterons are the points with error bars and ^{3}H (^{4}He) are displayed as the open (solid) stars. RQMD calculations were done in [69].

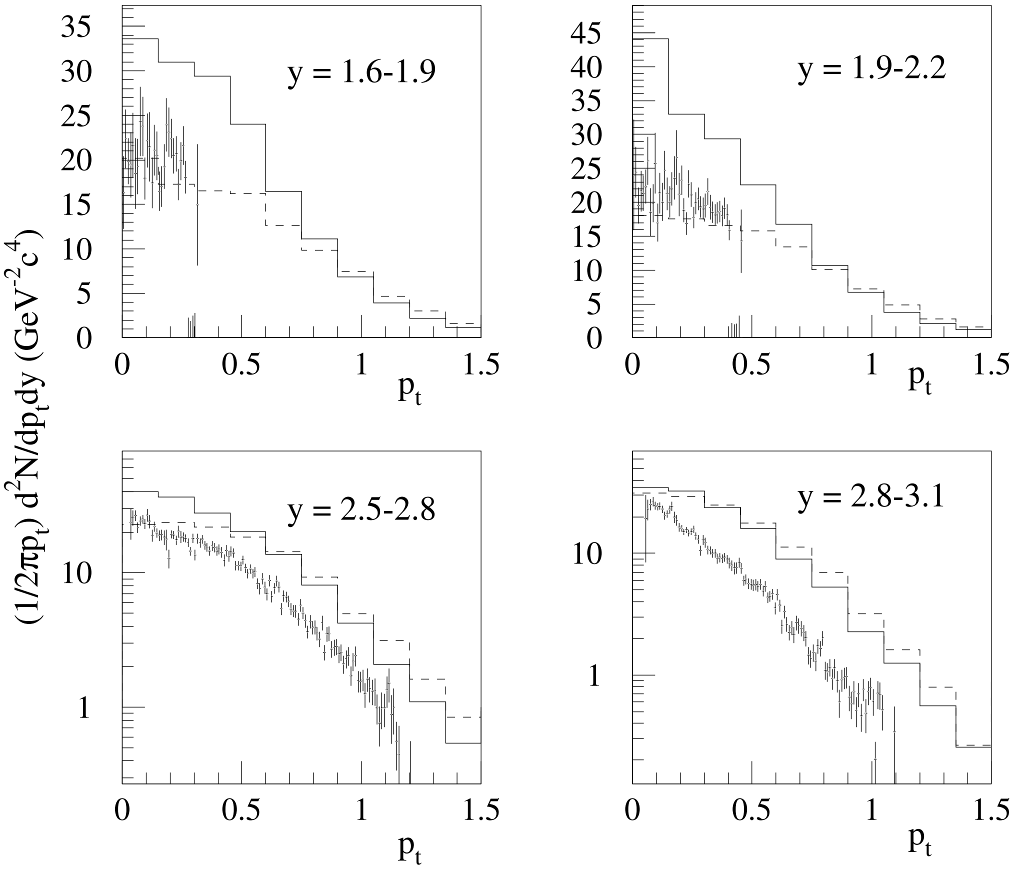

Figure 5.13: Protons from RQMD v2.3 in both cascade (solid line) and mean-field (dotted line) mode overlaid with the data measured by E877 in [47].

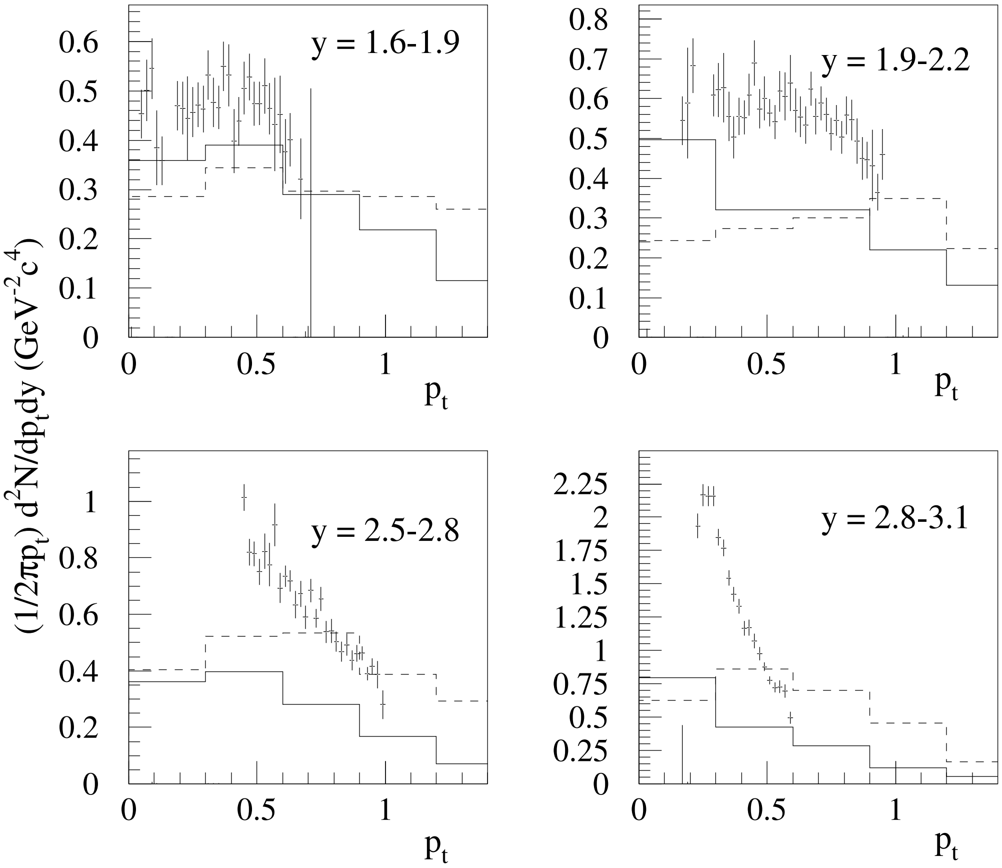

Figure 5.14: Deuterons from RQMD v2.3 in both cascade (solid line) and mean-field (dotted line) mode overlaid with the data measured by E877 in [47].

5.5 Summary

In this chapter, quantitative calculations of deuteron multiplicities and the coalescence parameter have been performed and measured deuteron multiplicities have been compared with their predictions. Matrix models and a simple thermal model have been shown to deduce freeze-out radii much larger than that gleaned from particle correlations. A new method for acquiring source information from deuteron multiplicities has been devised and a first sample of the sensitivity of such a model to deuteron yields presented. Using this method, a measure of the source volume can be made and the resulting transverse radius and temperature are found to be $R = 6.5^{+1.7}_{-.4}$fm and $T = 137^{+38}_{-12}$MeV. Although the model devised does not describe particle specie away from mid-rapidity, the technique for more precisely extracting source parameters from deuterons simply awaits a sufficient model of the source in order to deduce a quantitative source description. Comparisons to RQMD have also shown that proton and deuteron distributions, though consistent with a mean-field description of the collision at mid-rapidity, are not described away from mid-rapidity.

Chapter 6

Coda

> *I have only one ambition left: I should like to have a good epitaph.*
> [Prince Bismark]

The primary focus of this thesis has been to measure and quantitatively describe light fragment formation in Au + Au collisions at the AGS utilizing experiment E877. To this end, invariant multiplicity distributions for ^{2}H, ^{3}H and ^{3}He at mid-rapidity and ^{2}H and ^{4}He at beam rapidity have been measured and described.

Light fragments at mid-rapidity are qualitatively describable through the coalescence parameter as an increased volume at freeze-out over Si + Al and Si + Pb collisions at the same beam energy. However, simple matrix models fail in their deduction of the volume at freeze-out, surpassing a reasonable value by a factor of 2-3. As these models are incompatible with freeze-out conditions, a coalescence afterburner was implemented in order to describe deuteron multiplicities with a number of models.

A simple thermal model with a Gaussian freeze-out distribution cannot describe the deuteron yields without reverting to an excessively small volume.

However, a reasonable flowing, thermal source [75] with a coalescence assumption is found to restrict the parameters of the source significantly and reasonably. The transverse radius and temperature of the source deduced via this method are $R = 6.5^{+1.7}_{-.4}$fm and $T = 137^{+38}_{-12}$MeV. All previous measurements of the radius parameter are now recognized to suffer in accuracy because they fail to account for flow effects. In this work, it has been demonstrated that deuteron spectral shapes and yields can be used to simultaneously measure the system's flow and true radius. The author believes this result to be the first one to explicitly remove flow effects and thereby measure the true radius.

Furthermore, comparisons of RQMD with a coalescence afterburner to the measured data have been made and, though quantitatively the same at mid-rapidity, diverge rapidly from one another away from mid-rapidity.

Beam rapidity fragments in these collisions were shown to be inconsistent with Bevalac measures of fragments, proving that the region of invariance with respect to entrance channel has not yet been reached in collisions at 1 GeV·A.

The results in this thesis have provided a path which future analyses can expound upon. Given the advent of an analytic model which can describe the multiplicity distributions of particles in our collisions, the deuteron yield can be used to significantly constrain source parameters. Ideally only would incorporate more species than has been demonstrated here as well as identical particle correlation measurements coupled with a correlation afterburner. Should such an analytical model be developed, accurate parameters can be extracted at AGS energies for the first time.

Bibliography

[1] Review of Particles and Fields, Phys. Rev. D **54** (1996).

[2] E. Laermann Nucl. Phys. **A610** (1996) 1c.

[3] T. D. Lee, Rev. Mod. Phys, **47** (1975) 267.

[4] T. Schäfer, Nucl. Phys. **A610** (1996) 13c.

[5] C. Itzykson and J. B. Zuber, "Quantum Field Theory", McGraw-Hill, 1980.

[6] J. D. Bjorken, preprint hep-ph/9610516, to be published in the proceedings of the 1996 DPF/DPB Summer Study of New Directions for High Energy Physics, Snowmass, CO, June 25-July 12, 1996.

[7] J. D. Bjorken *et al.*, Fermilab Proposal T-864, April 1993.

[8] M. M. Aggarwal et al. HEPEX-9710015, Oct 1997, Submitted to Phys. Lett. B

[9] K. M. Nollett, M Lemoine, D. N. Schramm, Phys. Rev. C **50** (1997) 1144; P.J.E. Peebles, D. N. Schramm, E. L. Turner and R. G. Kron, Nature

(London) **352** (1991) 769; C. J. Copi, D. N. Schramm, and M. S. Turner, Science **267** (1995) 192.

[10] T. J. Hallmann and J. Thomas, Nucl. Phys. **A590** (1995) 399c.

[11] See for example the proceedings for Quark Matter '96, Nucl. Phys. **A610** (1996).

[12] R. Hanbury-Brown and R. Q. Twiss, Nature **178** (1956) 1046.

[13] B. V. Jacak, for the NA44 collaboration, Nucl. Phys. **A590** (1995) 215c.

[14] A. Drees, Nucl. Phys. **A610** (1996) 536c.

[15] S. T. Butler and C. A. Pearson, Phys. Rev. **129** (1963) 836.

[16] A. Schwarzschild and Č. Zupančič, Phys. Rev. **129** (1963) 854.

[17] A.Z. Mekjian, Phys. Rev. C **17** (1978) 1051; Nucl. Phys. **A312** (1978) 491.

[18] P. Braun-Munzinger, J. Stachel, J.P. Wessels, Nu Xu Phys. Lett. **B344** (1995) 43; Phys. Lett. **B365** (1996) 1.

[19] E. Schnedermann, J. Sollfrank, U. Heinz Phys. Rev. C **48** (1993) 2462.

[20] S. Nagamiya *et al.*, Phys. Rev. C **24** (1981) 971; Lemaire, Phys. Rev. Lett. **37**, (1976) 667; R. L. Auble *et al.*, Phys. Rev. C **28** (1983) 1552.

[21] S. Wang *et al.*, Phys. Rev. Lett. **74** (1995) 2648.

[22] J. Barrette *et al.*, Phys. Rev. C **50**, 1077 (1994); Phys. Rev. C **50** (1994) 3047; Phys. Rev. Lett **70** (1993) 1763.

[23] T. Abbot *et al.*, Phys. Rev. C **50** (1994) 1024.

[24] A. Schüttauf *et al.*, Nucl. Phys. **A607** (1996) 457.

[25] J. Pochodzalla, *et al.*, Phys. Rev. Lett. **75** (1995) 1040.

[26] P.B. Gossiaux, R. Puri, Ch. Hartnack, and J. Aichelin, Nucl. Phys. **A619** (1997) 379.

[27] K. Askatorab, for the E866 collaboration, Proceedings of Heavy Ion Physics at the AGS (1996) 98.

[28] J. Simon-Gillo for the NA44 collaboration, Nucl. Phys. **A590** (1995) 483c.

[29] J. W. Cronin *et al.*, Phys. Rev. D **11** (1975) 3105.

[30] J.L. Nagle, B.S. Kumar, D. Kusnezov, H. Sorge, and R. Mattiello, Phys. Rev. C **53** (1996) 367.

[31] M. Beyer and G. Röpke, nucl-th/9706021.

[32] S. Mrówczyński, J. Phys. **G13** (1987) 1089.

[33] S. Mrówczyński, Phys. Lett **B277** (1992) 43

[34] P. Danielewicz and P. Schuck, Phys. Lett. **B274** (1992) 268.

[35] S. Leupold and U. Heinz, Phys. Rev. C **50**, 1994) 1110.

[36] H. Sato and K. Yazaki, Phys. Lett. **98B** (1981) 153.

[37] D. E. Kahana *et al.*, Phys. Rev. C **54** (1996) 338.

[38] C. B. Dover, Phys. Rev. C **44**(1991) 1636.

[39] P. Braun-Munzinger and J. Stachel, J. Phys. **G21** (1995) L17.

[40] J. Stachel, Nucl. Phys **A610** (1996) 509c.

[41] J. Stachel, private communication.

[42] M. S. Muthuswamy, PhD thesis, SUNY at Stony Brook (1992).

[43] B. Hong, PhD thesis, SUNY at Stony Brook (1995).

[44] Y. Zhang, PhD thesis, SUNY at Stony Brook (1995).

[45] J. Dee, PhD thesis, SUNY at Stony Brook (1995).

[46] J. Simon-Gillo, PhD thesis, Texas A&M University (1992).

[47] T. W. Piazza, PhD thesis, SUNY at Stony Brook (1997).

[48] W. C. Chang, PhD thesis, SUNY at Stony Brook (1997).

[49] Z. Zhang, PhD thesis, University of Pittsburgh(1993).

[50] L. S. Waters, PhD thesis, SUNY at Stony Brook (1990).

[51] C.M. Zou, PhD thesis, SUNY at Stony Brook (1996).

[52] R. Bersch, MSI thesis, SUNY at Stony Brook (1995).

[53] S. V. Green, PhD thesis, Yale University (1992).

[54] R. Lacasse, PhD thesis, McGill University (1997).

[55] Leo, W.R. *"Techniques for Nuclear and Particle Physics Experiments"*, Springer-Verlag, 1994.

[56] M. Pollack, PhD thesis, SUNY Stony Brook (1997).

[57] Y. Kwon, PhD thesis, SUNY Stony Brook (1997).

[58] S. Panitkin, PhD thesis, SUNY Stony Brook (1997).

[59] K. Shigaki, PhD thesis, University of Tokyo, (1995).

[60] Nu Xu for the NA44 collaboration, Nucl. Phys. **A610** (1996) 175c.

[61] B. Alper *et al.*, Nucl. Phys. **B100** (1975) 237; K. Guettler *et al.*, Nucl. Phys. **B116** (1976) 77.

[62] J. K. Pope, for the E864 collaboration, Proceedings of Heavy Ion Physics at the AGS (1996) 119.

[63] Z. Chen, for the E866 collaboration, Proceedings of Heavy Ion Physics at the AGS (1996) 5.

[64] B. Holzer, for the NA44 collaboration, *Proceedings of the 13th Winter Workshop on Nuclear Dynamics.*, ed. A. Mignerey and W. Bauer. (1997); M. Murray, for the NA44 collaboration, to appear in the Proceedings of the Third International Conference of Physics and Astrophysics of

the Quark Gluon Plasma, Jaipur, India (1997), preprint number nucl-ex/9706007.

[65] S. Chiba, Phys. Rev. Lett. **67** (1991) 1982.

[66] J. Barrette *et al.*, Phys. Rev. Lett. **78** (1997) 2916.

[67] T. Vongpaseuth, to be published in the Czechoslovak Journal of Physics.

[68] H. Sorge, H. Stöcker and W. Greiner Ann. Phys. (NY) **192** (1989) 266; Nucl. Phys. **A498** (1989) 567c; H. Sorge, A. v. Keitz, R. Mattiello, H. Stöcker and W. Greiner Z. Phys **C47** (1990) 629.

[69] R. Mattiello, A. Jens, H. Sorge, H. Stöcker, W. Greiner, Phys. Rev. Lett **74** (1995) 2180.

[70] J. Barrette *et al.*, Phys. Rev. Lett **78** (1997) 2916.

[71] S. Koonin, Phys. Lett. **B 70** (1977) 640; R. Lednicky, V.I. Lyuboshits, Sov. J. Nucl. Phys. **35** (1982) 770.

[72] E.M. Remler, Ann. Phys. **136** (1981) 293; M. Gyulassy, K. Frankel, and E.M. Remler, Nucl. Phys. **A402** (1983) 596; J. Aichelin, A. Rosenhauer, G. Peilert, H. Stocker, and W. Greiner, Phys. Rev. Lett. **58** (1987) 1926

[73] G.Q. Li, C.M. Ko, and B.A. Li, Phys. Lett. **74** (1995) 235; G.Q. Li and C.M. Ko, Phys. Rev. C **54** (1996) 54.

[74] S. Chapman, J.R. Nix, and U. Heinz, Phys. Rev. C **52** (1995) 2694.

[75] U. Heinz, Nucl. Phys. **A610** (1996) 264c.

[76] S. Esumi, S. Chapman, H. van Hecke, Nu Xu, Phys. Rev. C **55** (1997) R2163.

[77] J. Barrette *et al.*, (E877 Collaboration) Phys. Rev. C **55** (1997) 1420; Phys. Rev. C **51** (1995) 3309; Phys. Rev. Lett. **70** (1993) 2996.

[78] J. Barrette *et al.*, submitted to Phys. Rev. C, preprint number nucl-ex/9707002

[79] R. Mattiello, H. Sorge, H. Stöcker and W. Greiner Phys. Rev. C **53** (1997) 1443.

[80] K. Ashktorab, for the E866 collaboration, proceedings of HIPAGS '96 (1996) 98.

[81] S. Ahmad *et al.*, Phys. Lett. **B382** (1996) 35.

[82] D. Miśkowiec E877 collaboration notes, 14 Febuary 1996 and 18 April 1997

Appendix A

Hyperon Contamination of Protons

The total measured proton invariant cross-section measured by our apparatus are, by their nature, a superposition of protons and hyperon decays (Λ, Σ^0, Ξ). Depending on the particular experimental apparatus in question, the hyperon contribution will contaminate the measured protons differently. As the of hyperon to nucleon ratio for our collisions is near 8% [40, 81], experimental efficiencies for hyperons in the proton spectra must be accounted for in order to properly draw comparisions across experimental platforms. Therefore, each experiment must account, through Monte Carlo simulations, for the amount of hyperon contamination in the proton spectra.

Preliminary analysis of hyperon contamination for E877 has been performed by [47] in which the fractional hyperon contribution to proton spectra was determined by utilizing a Monte Carlo program; the lambda spectra measured by E891 [81] for Au+Au collisions at the AGS was used as input. This analysis assumed that all protons from lambda decays were reconstructed by STEP1 and fell within the $mass^2$ cuts applied in the particle identification procedure (see Section 3.8). However, because STEP1 *assumes* all particles originated from the target, protons from Λ decays will be assigned an incorrect momentum which may push the reconstructed $mass^2$ outside of the particle identification cuts. Therefore, the proton invariant cross-sections will contain only a portion of those Λ's which passed through the spectrometer cuts.

For this thesis, two additional features were added to this Monte Carlo feature of [47]. First, the reconstructed momentum and time of flight were smeared according to the experimentally determined resolutions [82]. And, second, the reconstructed mass^2 of the protons and Λ's were passed through the standard particle identification routine as described in Section 3.8.

Shown in Fig. A.1 is the percentage of protons from hyperon decays, assuming the E891 [81] yield of hyperons, which would pass through our spectrometer and pass our hyperon cuts as a function of p_t for various bins in rapidity. The error bars on the E891 measurements are approximately 30% and, therefore, our measured contamination also includes 30% error bars. We find, however, that the Λ contamination percentage changes the d/p^2 minimally and, therefore, the E891 error bars are negligle in comparison with the statistical and systematic error bars in our experimental measurements.

For calculating the yield of protons in the d/p^2 ratio, then, we will utilize this contamination percentage as an upper limit on hyperons and add systematic error bars to our calculations consistent with these values.

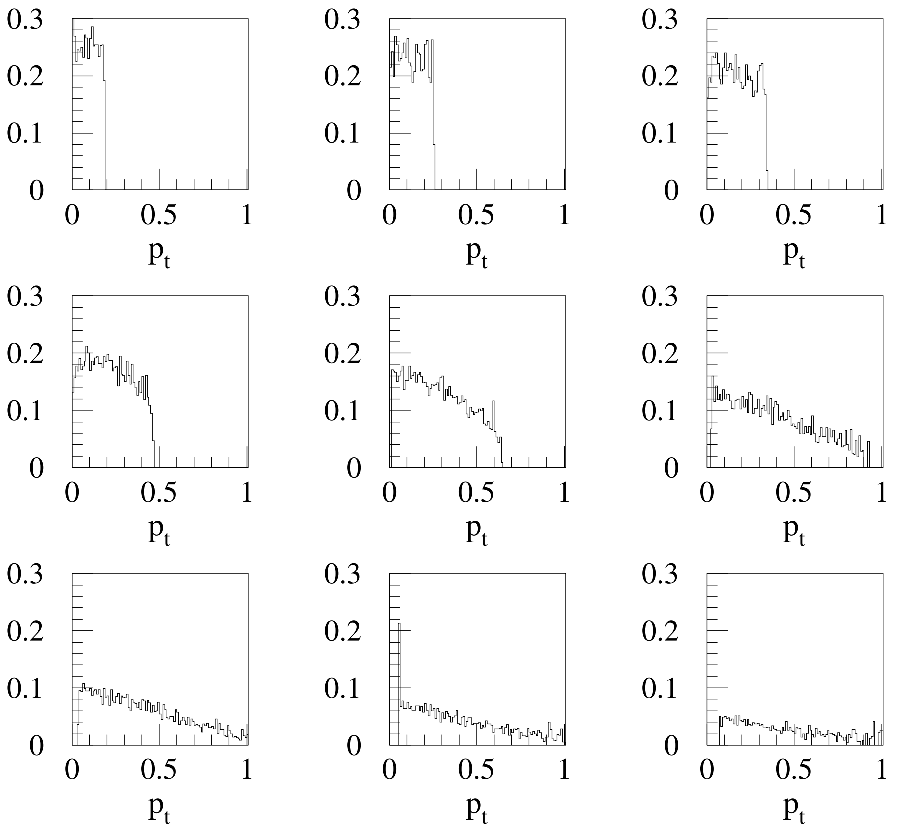

Figure A.1: Percentage of protons from hyperon decays as a function of p_t for various rapidity bins, beginning in the top left-hand corner with rapidity y=1.5-1.7 and progressing in .2 rapidity bins to y=3.1-3.2 in the lowest right-hand corner.

Appendix B

Inextractability of non-beam-rapidity ^4He

There are a total of 6 million 4% inclusive events in the 1994 data set. This number, coupled with our efficiency for measuring ^{4}He in our experiment conspire to make the total number of ^{4}He in the 1994 data set negligible, as will be shown in the following calculation.

The cross-section of light fragments is driven by the probability for coalescence. This probability, for simple models decreases trivially by a 'penalty factor' for each successively massive particle. For example, the ratio of the deuteron to proton cross-section is approximately .02, as is the ratio of ^{3}He to deuterons. Similarly, we might expect that the invariant cross-section for ^{4}He would be an extra factor of .02 lower than that of ^{3}He. This would place the ^{4}He invariant cross-section near $p_t = 0$ to be approximately $1 - 2 \times 10^{-4}$ GeV^{-2}. RQMD 1.08 [79] predicts this value to be an order of magnitude lower.

If we assume the ^{4}He is relatively constant as a function of p_t, in agreement with deuteron and ^{3}He measurements, then the invariant cross section, written as

$$\left.\frac{1}{2\pi p_t}\frac{d^2N}{dp_t dy}\right|_{mid-y} \approx 1.5 \times 10^{-4}\left(\frac{1}{GeV^2}\right) \quad \text{(B.1)}$$

can be simplified for the first 1GeV in p_t as

$$\left.\frac{d^2N}{dp_t dy}\right|_{mid-y} \approx 4.7 \times 10^{-4}. \quad \text{(B.2)}$$

Then, about mid-rapidity ($y = 1.4 - 1.8$) in the first 1 GeV of p_t we would expect approximately 1.88×10^{-4} ^{4}He per event. In 6 million events we would expect to create 10 to 12 thousand ^{4}He. However, our acceptance for ^{4}He over mid-rapidity is calculated, via the method outlined in Section 3.10.2, to be about 8.4×10^{-3} which would result in a total of 10 ^{4}He in the entire data set.

We find no unambiguous ^{4}He particle in our data set at non-beam rapidities. Beyond the simple explanation of low yield given above, a further complication in extracting them derives from the fact that the deuteron reconstructed mass^2 distribution lies directly over the ^{4}He mass^2 distribution, as described in Section 3.9.3.

Appendix C

Lower Centrality Deuterons

In Fig. C.1 are the spectra of deuterons for the centrality cut of 6-9%. As has already been noted, there is little difference between this centrality and the 4% inclusive bin in the mid rapidity region though the beam region consists of a factor of 2 difference in the invariant cross-section.

Further, shown in Fig. C.2 is the deuteron invariant cross-section of the 10-20% centrality bin. Due to the more limited statistics in this centrality range arising from the online trigger down-scaling, the number of bins is lower. However, the cross-section clearly follows that of the 0-4% and 6-9% centrality bins except near beam rapidity, where the 10-20% bin is larger than the most central region by a factor of 5.

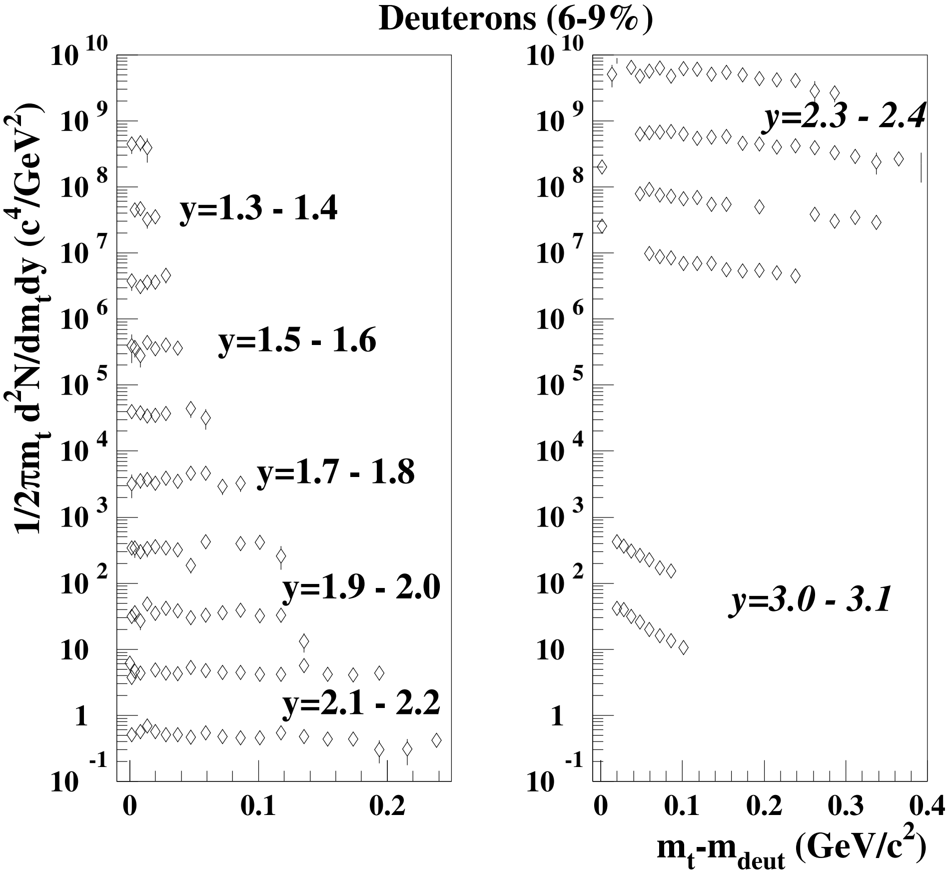

Figure C.1: Invariant cross section of deuterons for the centrality region of 6-9% measured by E877. The spectra for $y = 3.1 - 3.2$ and $y = 2.1 - 2.2$ are correctly normalized and each rapidity bin below these is multiplied by successive powers of 10 for ease of display.

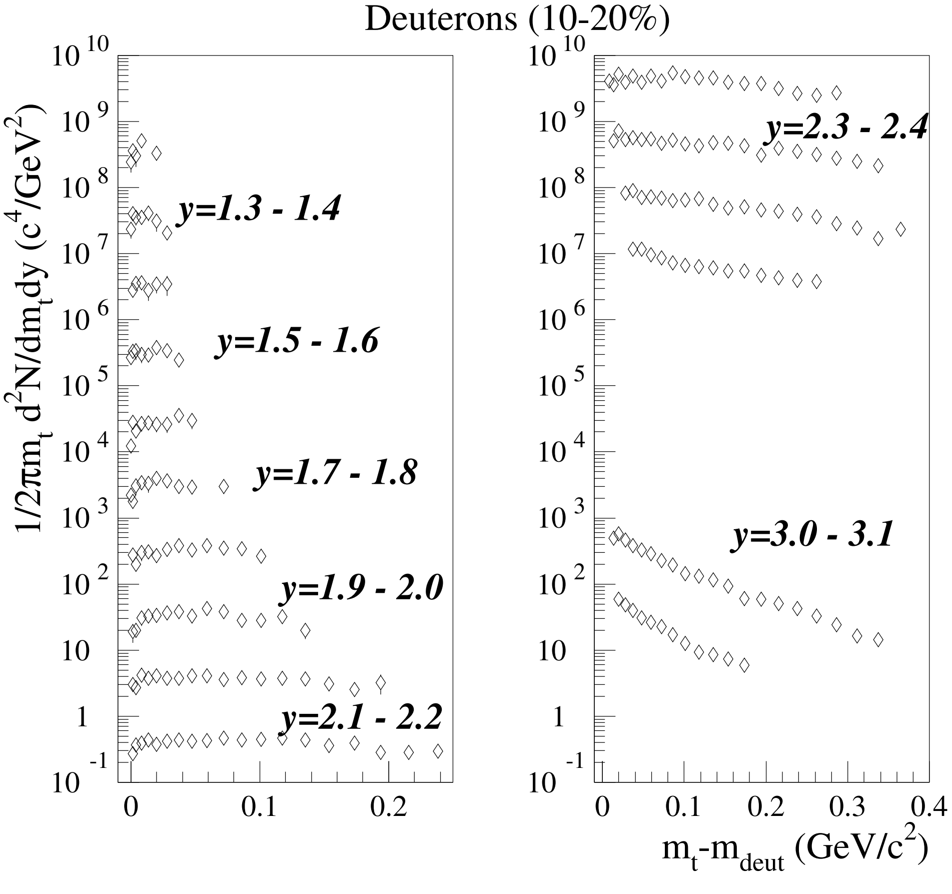

Figure C.2: Invariant cross section of deuterons for the centrality region of 10-20% measured by E877. The spectra for $y = 3.1 - 3.2$ and $y = 2.1 - 2.2$ are correctly normalized and each rapidity bin below these is multiplied by successive powers of 10 for ease of display.

Appendix D

Tabulated Results

Following are the measured multiplicities of deuterons as a function of p_t and y for the 4% most central collisions.

p_t (GeV)	y = 1.2-1.3	y = 1.3-1.4	y = 1.4-1.5	y = 1.5-1.6	y = 1.6-1.7
0.02-0.04	3.050± 0.469	2.980± 0.481	3.173± 0.381	2.960± 0.325	2.665± 0.356
0.04-0.06	3.200± 0.484	3.510± 0.519	2.991± 0.607	3.273± 0.447	2.782± 0.384
0.06-0.08	3.247± 0.621	2.880± 0.443	3.043± 0.506	2.405± 0.467	3.381± 0.503
0.08-0.10	2.956± 0.747	3.468± 0.833	2.327± 0.902	2.945± 0.457	2.891± 0.580
0.10-0.12	3.848± 0.931	3.075± 0.587	2.819± 0.414	2.582± 0.363	2.349± 0.561
0.12-0.14	3.445± 0.427	2.753± 0.354	2.753± 0.415	3.264± 0.496	2.456± 0.372
0.14-0.16	3.491± 0.671	2.849± 0.430	3.310± 0.426	3.191± 0.490	2.754± 0.317
0.16-0.18	2.980± 1.191	2.518± 0.360	3.236± 0.469	2.522± 0.329	2.975± 0.592
0.18-0.20	3.948± 0.596	3.049± 0.492	3.483± 0.397	3.144± 0.334	2.491± 0.337
0.20-0.22	3.219± 0.636	3.434± 0.702	3.030± 0.339	3.012± 0.337	2.961± 0.359
0.22-0.24	3.363± 0.700	3.193± 0.466	2.627± 0.462	2.689± 0.342	2.862± 0.372
0.24-0.26	3.302± 0.732	3.369± 0.465	2.631± 0.453	2.430± 0.379	2.937± 0.278
0.26-0.28	2.763± 0.914	3.336± 0.238	3.082± 0.359	2.701± 0.408	2.549± 0.305
0.28-0.30		3.800± 0.755	3.259± 0.402	2.492± 0.367	2.665± 0.333
0.30-0.32			2.896± 0.410	2.982± 0.401	2.390± 0.752
0.32-0.34			2.838± 0.384	2.935± 0.317	2.716± 0.404
0.34-0.36				2.911± 0.388	3.261± 0.362
0.36-0.38				2.989± 0.510	3.249± 0.305
0.38-0.40				3.041± 0.660	3.406± 0.356

Table D.1: $1/p_t d^2N/dp_t dy$

p_t (GeV)	y = 1.7-1.8	y = 1.8-1.9	y = 1.9-2.0	y = 2.0-2.1	y = 2.1-2.2
0.02-0.04	2.986± 0.404				
0.04-0.06	2.702± 0.281	2.846± 0.308	2.658± 0.344	3.655± 0.543	
0.06-0.08	2.755± 0.316	3.145± 0.393	2.883± 0.319	3.873± 0.362	
0.08-0.10	3.392± 0.538	3.424± 0.389	2.601± 0.283	3.677± 0.376	
0.10-0.12	2.914± 0.403	2.414± 0.475	3.177± 0.351	3.927± 0.416	
0.12-0.14	2.008± 0.427	2.252± 0.308	3.417± 0.454	3.399± 0.335	
0.14-0.16	2.737± 0.321		2.249± 0.410	3.944± 0.488	
0.16-0.18	2.838± 0.344		2.869± 0.389	3.380± 0.627	3.421± 0.386
0.18-0.20	3.234± 0.566	2.952± 0.312			3.698± 0.871
0.20-0.22	2.936± 0.358	2.920± 0.335	2.456± 0.304		4.287± 0.437
0.22-0.24	2.997± 0.329	2.789± 0.532	3.434± 0.357		
0.24-0.26	2.714± 0.337	2.868± 0.317	2.885± 0.419	3.462± 0.337	
0.26-0.28	2.858± 0.357	2.964± 0.285	2.861± 0.344	3.434± 0.378	
0.28-0.30	2.981± 0.318	2.909± 0.297	2.872± 0.263	4.075± 0.534	3.823± 0.330
0.30-0.32	2.755± 0.319	3.342± 0.317	2.942± 0.274	3.549± 0.376	3.905± 0.424
0.32-0.34	2.647± 0.353	2.995± 0.314	3.124± 0.279	3.192± 0.302	3.936± 0.548
0.34-0.36	2.575± 0.356	2.930± 0.278	3.114± 0.285	2.890± 0.300	3.490± 0.388
0.36-0.38	2.664± 0.370	3.453± 0.314	3.116± 0.326	3.282± 0.324	3.157± 0.336
0.38-0.40	2.766± 0.283	3.340± 0.394	3.228± 0.298	3.504± 0.292	3.488± 0.296

Table D.2: $1/p_t d^2N/dp_t dy$

p_t (GeV)	y = 1.7-1.8	y = 1.8-1.9	y = 1.9-2.0	y = 2.0-2.1	y = 2.1-2.2
0.40-0.42	2.682± 0.285	2.501± 0.411	2.948± 0.253	4.083± 0.364	3.470± 0.268
0.42-0.44	3.095± 0.320	2.752± 0.313	2.623± 0.330	3.557± 0.331	3.826± 0.332
0.44-0.46	3.208± 0.312	3.175± 0.335	3.259± 0.383	3.445± 0.340	4.331± 0.360
0.46-0.48	2.833± 0.350	3.315± 0.296	3.050± 0.349	3.344± 0.307	3.608± 0.313
0.48-0.50	2.792± 0.437	2.976± 0.282	2.571± 0.316	3.437± 0.322	3.772± 0.343
0.50-0.52	2.799± 0.411	2.979± 0.274	2.779± 0.280	3.332± 0.405	3.544± 0.215
0.52-0.54		3.202± 0.350	2.953± 0.304	3.117± 0.362	3.401± 0.268
0.54-0.56		2.914± 0.327	3.075± 0.272	3.431± 0.399	3.884± 0.323
0.56-0.58		2.712± 0.595	2.948± 0.262	3.172± 0.275	3.805± 0.378
0.58-0.60		2.842± 0.494	2.893± 0.288	3.575± 0.342	4.015± 0.444
0.60-0.62		2.369± 0.409	2.699± 0.291	3.484± 0.300	3.584± 0.347
0.62-0.64		2.519± 0.339	3.086± 0.381	3.827± 0.313	3.482± 0.322
0.64-0.66			2.805± 0.392	3.965± 0.312	3.349± 0.298
0.66-0.68			2.544± 0.335	3.359± 0.264	3.924± 0.265
0.68-0.70			2.528± 0.346	3.519± 0.313	3.487± 0.280
0.70-0.72			2.580± 0.372	3.566± 0.318	3.695± 0.270
0.72-0.74				3.308± 0.331	3.517± 0.268
0.74-0.76				3.711± 0.564	3.211± 0.258
0.76-0.78				3.236± 0.414	3.425± 0.243
0.78-0.80				2.720± 0.313	3.157± 0.254
0.80-0.82				2.512± 0.300	3.504± 0.296
0.82-0.84				2.932± 0.334	3.433± 0.320
0.84-0.86				2.713± 0.352	3.098± 0.356
0.86-0.88				3.043± 0.397	2.821± 0.335
0.88-0.90					2.799± 0.288
0.90-0.92					2.711± 0.564
0.92-0.94					2.291± 0.286
0.94-0.96					2.892± 0.400

Table D.3: $1/p_t d^2N/dp_t dy$

p_t (GeV)	y = 2.2-2.3	y = 2.3-2.4	y = 2.4-2.5	y = 2.5-2.6
0.32-0.34	4.131± 0.360			
0.34-0.36	4.267± 0.376			
0.36-0.38	5.398± 0.562			
0.38-0.40	3.896± 0.461	5.045± 0.392		
0.40-0.42	4.057± 0.379	4.979± 0.338	6.204± 0.345	
0.42-0.44	4.069± 0.343	4.729± 0.537	5.021± 0.267	
0.44-0.46	3.874± 0.285	4.327± 0.763	4.605± 0.339	6.362± 0.297
0.46-0.48	4.140± 0.400	4.846± 0.374	5.305± 0.397	5.149± 0.292
0.48-0.50	4.254± 0.326	4.257± 0.325	4.715± 0.418	5.113± 0.276
0.50-0.52	4.076± 0.348	4.226± 0.337	4.785± 0.400	4.714± 0.291
0.52-0.54	4.027± 0.364	4.100± 0.240	4.641± 0.345	5.167± 0.390
0.54-0.56	4.106± 0.303	4.050± 0.231	4.333± 0.259	4.867± 0.483
0.56-0.58	3.917± 0.287	4.195± 0.250	4.402± 0.270	5.758± 0.471
0.58-0.60	4.078± 0.308	4.097± 0.234	4.232± 0.351	4.350± 0.331
0.60-0.62	3.737± 0.334	4.312± 0.247	4.279± 0.317	4.615± 0.238
0.62-0.64	4.307± 0.343	3.922± 0.282	4.589± 0.269	4.512± 0.241
0.64-0.66	3.877± 0.344	4.031± 0.287	4.564± 0.261	3.983± 0.308
0.66-0.68	3.935± 0.411	4.032± 0.269	4.406± 0.256	4.224± 0.285
0.68-0.70	4.272± 0.424	3.360± 0.205	3.913± 0.278	3.706± 0.260
0.70-0.72	3.436± 0.345	4.165± 0.309	3.887± 0.227	4.300± 0.260
0.72-0.74	3.596± 0.322	3.954± 0.258	3.834± 0.266	3.685± 0.208
0.74-0.76	3.929± 0.301	3.787± 0.311	3.593± 0.216	4.114± 0.268
0.76-0.78	3.928± 0.286	3.599± 0.332	3.781± 0.231	3.379± 0.243
0.78-0.80	3.538± 0.240	3.614± 0.354		3.396± 0.269
0.80-0.82	3.442± 0.247	3.275± 0.320	3.885± 0.240	3.161± 0.224
0.82-0.84	3.537± 0.255	3.308± 0.240	3.200± 0.217	2.939± 0.220
0.84-0.86	3.316± 0.237	3.059± 0.222	3.340± 0.271	3.087± 0.244
0.86-0.88	3.436± 0.217	3.178± 0.214	3.030± 0.273	2.745± 0.216
0.88-0.90	3.251± 0.250	3.346± 0.206	3.188± 0.269	2.899± 0.186
0.90-0.92	3.028± 0.239	3.118± 0.196	2.925± 0.370	2.906± 0.154
0.92-0.94	3.114± 0.261	2.944± 0.758	2.867± 0.236	2.449± 0.155
0.94-0.96	2.860± 0.251	2.884± 0.185	2.690± 0.197	2.609± 0.174
0.96-0.98	3.041± 0.288	3.192± 0.196	2.620± 0.356	2.426± 0.305
0.98-1.00	2.709± 0.356	2.851± 0.179	2.616± 0.181	1.760± 0.314
1.00-1.02	2.701± 0.370	2.571± 0.218	2.988± 0.208	
1.02-1.04	2.211± 0.328	2.591± 0.168	2.479± 0.163	
1.04-1.06	2.507± 0.345	2.632± 0.253		
1.06-1.08	1.854± 0.235	2.500± 0.188	2.240± 0.154	
1.08-1.10		2.088± 0.220	2.463± 0.223	
1.10-1.12		2.385± 0.310	2.140± 0.143	
1.12-1.14		1.941± 0.263	2.046± 0.161	
1.14-1.16		1.517± 0.229	1.949± 0.160	
1.16-1.18			0.602± 0.151	

Table D.4: $1/p_t d^2N/dp_t dy$

p_t (GeV)	y = 3.0-3.1	y = 3.1-3.2
0.22-0.24	12.139± 0.578	
0.24-0.26	13.599± 0.510	12.463± 0.877
0.26-0.28	13.555± 0.471	14.188± 0.706
0.28-0.30	13.552± 0.475	13.618± 0.493
0.30-0.32	11.612± 0.400	13.551± 0.470
0.32-0.34	11.110± 0.394	11.753± 0.402
0.34-0.36	9.691± 0.368	11.158± 0.397
0.36-0.38	8.916± 0.346	9.024± 0.340
0.38-0.40	8.361± 0.346	8.191± 0.376
0.40-0.42	7.313± 0.348	7.422± 0.360
0.42-0.44	7.356± 0.377	7.087± 0.340
0.44-0.46	6.714± 0.343	5.561± 0.313
0.46-0.48	6.135± 0.303	5.405± 0.247
0.48-0.50	5.517± 0.218	4.767± 0.275
0.50-0.52	4.867± 0.196	4.592± 0.273
0.52-0.54	4.530± 0.234	4.123± 0.272
0.54-0.56	4.562± 0.302	3.961± 0.282
0.56-0.58	4.373± 0.314	3.431± 0.219
0.58-0.60	3.118± 0.281	3.009± 0.260
0.60-0.62		2.613± 0.197
0.62-0.64		2.541± 0.244

Table D.5: $1/p_t d^2N/dp_t dy$

Appendix E

Calculations of Participant and Spectator Regions

In order to determine the number of participants and spectators in a heavy-ion collisions, a simple Monte Carlo, outlined below, is implemented.

Assuming that a strong correlation exists between transverse energy and impact parameter b (as discussed in Section 2.3) the impact parameter relates to the centrality of the collisions simply by the geometric relation

$$f = \frac{\int_0^b db'b'}{\int_0^{2R} db'b'} \tag{E.1}$$

where f is the fractional centrality and R is the radius of the nucleus. Therefore,

$$b = 2R\sqrt{f}. \tag{E.2}$$

From here a simple Monte Carlo program can be written that gives the fraction of nucleons participating in the collision as a function of centrality by simply randomly determining x, y, and z locations inside of one of the nuclei and then counting it as a participator if it overlaps with the corresponding cylinder that will be shaved out by the colliding nucleus. Shown in Fig. E.1 is the corresponding calculation giving the percentage of interacting nuclei as a function of centrality. This calculation will be used whenever quantitative comparisons between varying centralities deem it necessary.

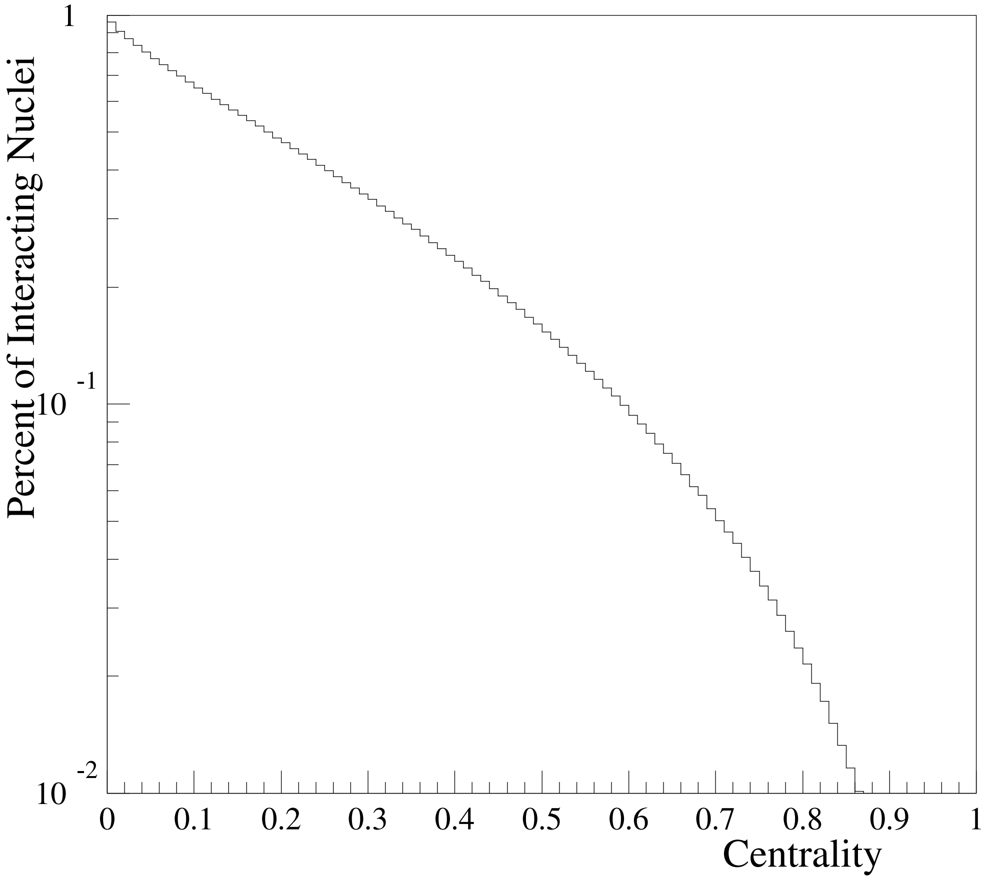

Figure E.1: Number of interacting nuclei as a function of centrality for the simple model outlined in the text.